ISSN 2159-5275 (Print)
ISSN 2159-5283 (Online)

From Knowledge to Wisdom

Journal of Mechanics Engineering and Automation

Volume 4, Number 6, June 2014

David Publishing Company
www.davidpublishing.com

Journal of Mechanics Engineering and Automation

Volume 4, Number 6, June 2014 (Serial Number 36)

David Publishing Company
www.davidpublishing.com

Publication Information:
Journal of Mechanics Engineering and Automation is published monthly in hard copy (ISSN 2159-5275) and online (ISSN 2159-5283) by David Publishing Company located at 240 Nagle Avenue #15C, New York, NY 10034, USA.

Aims and Scope:
Journal of Mechanics Engineering and Automation, a monthly professional academic journal, particularly emphasizes practical application of up-to-date technology in realm of Mechanics, Automation and other relevant fields. And articles interpreting successful policies, programs or cases are also welcome.

Manuscripts and correspondence are invited for publication. You can submit your papers via web submission, or E-mail to mechanics@davidpublishing.com. Submission guidelines and web submission system are available at http://www.davidpublishing.com.

Editorial Office:
240 Nagle Avenue #15C, New York, NY 10034, USA
Tel: 1-323-984-7526, 323-410-1082; Fax: 1-323-984-7374, 323-908-0457
E-mail: mechanics@davidpublishing.com

Abstracted / Indexed in:
Google Scholar
Chinese Database of CEPS, Airiti Inc. & OCLC
Chinese Scientific Journals Database, VIP Corporation, Chongqing, China
CSA Technology Research Database
Database of EBSCO, Massachusetts, USA
Norwegian Social Science Data Services (NSD), Norway
Summon Serials Solutions
Ulrich's Periodicals Directory

Subscription Information:
Price (per year):
Print $520; Online $320; Print and Online $600

David Publishing Company
240 Nagle Avenue #15C, New York, NY 10034, USA
Tel: 1-323-984-7526, 323-410-1082; Fax: 1-323-984-7374, 323-908-0457
E-mail: order@davidpublishing.com
Digital Cooperative Company: www.bookan.com.cn

David Publishing Company
www.davidpublishing.com

Journal of Mechanics Engineering and Automation

Volume 4, Number 6, June 2014 (Serial Number 36)

Contents

Journal of Mechanics Engineering and Automation 4 (2014) 467-475

FE Study for Reducing Forming Forces and Flat End Areas of Cylindrical Shapes Obtained by the Roll-Bending Process

Quan Hoang Tran, Henri Champliaud, Zhengkun Feng and Thien My Dao

Mechanical Engineering Department, École de Technologie Supérieure, Montréal (Québec) H3C 1K3, Canada

Received: March 31, 2014 / Accepted: April 15, 2014 / Published: June 25, 2014.

Abstract: A roll-bending process that minimizes the flat areas on the leading and trailing ends of formed plates will produce more accurate and easier assemble final shapes. There are several methods of minimizing flat areas, but they are costly or difficult to apply for thick plates. This study proposes a new, simple approach that reduces these flat areas. This approach includes moving the bottom roll slightly along the feeding direction and adjusting the bottom roll location. Sensitivity analyses were performed using a developed 3D dynamic FE (finite element) model of an asymmetrical roll-bending process in the Ansys/LS-Dyna software package. Simulations were validated by experiments run on an instrumented roll-bending machine. The FE results indicate that this new approach not only minimizes the flat areas but also reduces the forming forces.

Key words: Roll-bending process, flat end areas, dynamic FEM simulation, Ansys/LS-Dyna.

1. Introduction

Roll bending is an efficient metal forming technique, where plates are bent to a desired curvature using forming rolls. This type of sheet forming process is one of the most widely used techniques for manufacturing axisymmetric shapes. Moreover, this process is beginning to be taken into serious consideration by industries for producing large, thick parts such as the thick, conically shaped crown of a Francis turbine runner or of a wind turbine tower [1].

Over the past few decades, several bending machines were developed to adapt to various forming production specifications. However, these can be classified into two major types of roll-bending machines in the current market: three-roll models and four-roll models. For three-roll models, depending upon the setup location of the forming rolls, they can be arranged in two groups: three-roll pyramidal models and three-roll asymmetric models. The roll-bending process is a continuous type of three-point bending, where the basic principles and operations can be found in Refs. [2-4]. Although the roll-bending process can be performed for a wide range of cylindrical parts, for heavy to extremely thick plate applications, there are several issues that limit its application more widely in metal forming. One of them is the flat areas that are left at the leading and trailing edges of the final shape when the process is completed as shown in Fig. 1.

Forming parts with minimal flat areas on the leading and trailing ends are easier to assemble by welding and obtain a more accurate final shape. However, studies on the mechanisms that produce flat areas are still limited in the literature. Typical studies focus mainly on analyzing the bending mechanism. Hua et al. [5-11] conducted a considerable amount of research studying the four-rolls bending process to understand the bending mechanism. Hu et al. [12] applied an FEM (finite element model) to the study of the mechanism of

Corresponding author: Quan Hoang Tran, Ph.D. student, research fields: simulation of manufacturing processes and analysis of metal forming process by FEMs (finite element methods). Email: hoang-quan.tran.1@ens.etsmtl.ca.

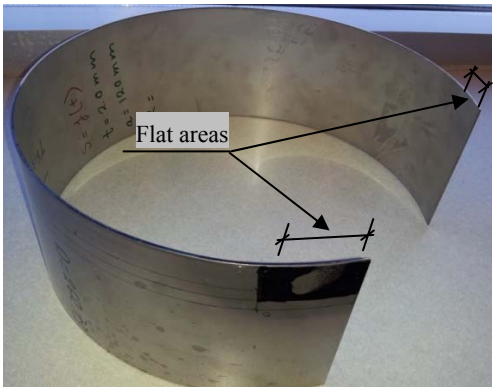

Fig. 1 Flat areas left by a roll-bending machine.

the roll-bending process. Analyses of the pyramidal three-roll-bending process and the asymmetrical three-roll-bending process can also be found in Refs. [13-15]. Zeng et al. [16], Feng et al. [17-19] and Tran et al. [20-24] developed FE (finite element) models using Ansys/LS-Dyna to simulate the three-roll-bending process. However, an analysis of the flat lengths that remain at both ends of the final shape has not been addressed.

The mechanism of the roll-bending process inherently produces a certain amount of flat area at the leading and trailing edges of the part. It is observed that this amount of unbent area depends on the machine type. Usually, a three-roll asymmetric model leaves a smaller flat area at the leading and trailing ends of the final shape relative to a pyramid-type model because the workpiece is held more firmly in Ref. [3]. Zhong et al. [25] analyzed the straight-end problem in a thin-plate, pyramid-type machine through the development of an analytical method. However, the authors did not discuss the flat areas produced by a three-roll asymmetric machine and did not propose a method to reduce these. Therefore, Tran et al. [24] expanded to study in additional detail the effect of the rolls setup on the length of the flat areas in this study. To reduce or even eliminate the unbent areas, a number of methods can be applied such as: (1) forming a small amount of extra length at each end and subsequently cutting them off or (2) hand hammering the flat end. However, these techniques are costly or difficult to apply for thick plates made of high-strength steel. Therefore, to obtain a better circularity for the final shape, the most common method used is to pre-bend both ends of the workpiece using the roll-bending machine. This is done by inserting the leading end of the workpiece into the machine. A short section of the plate is fed for pre-bending, and subsequently, the rotation of the rolls is reversed to remove the part. The pre-bending operation is then repeated at the other end of the blank. However, this is a drawback because the plate must be handled twice for pre-bending and requires more intensive labor at the production stage and additional safety measures.

The effect of moving the bottom roll to the left hand side by a distance d_i as shown in Fig. 2a and adjusting the bottom roll to a "gap" value g_i (Fig. 2b) on the flat ends length is presented in this paper. The goal is to propose a new approach to minimize the apparent flat ends and to reduce the forming forces.

The paper is divided in six sections. The content is as follows: Section 2 introduces the asymmetrical roll bending machine setup and flat areas definition; Section 3 details the FE model of the asymmetrical roll bending process; Section 4 presentes experimental study to validate the FE model; Section 5 is the discussion about the results; and Section 6 summarizes key conclusions of this research.

2. Asymmetrical Roll-Bending Machine and Flat Areas Definition

In this study, an asymmetrical roll-bending machine is used to shape a plate of thickness t as shown in Fig. 3.

The radius R of a formed cylindrical shape depends on the position of the lateral roll [19] and can be expressed in Eq. (1):

$$R = \frac{a}{2}\left[\frac{a\sin^2\theta}{2r + t - a\cos\theta} - \cos\theta\right] \quad (1)$$

where,

a: center location of lateral roll along action line;

r: radius of the rolls;

t: thickness of workpiece; and

θ: operating action line angle of offset cylinder.

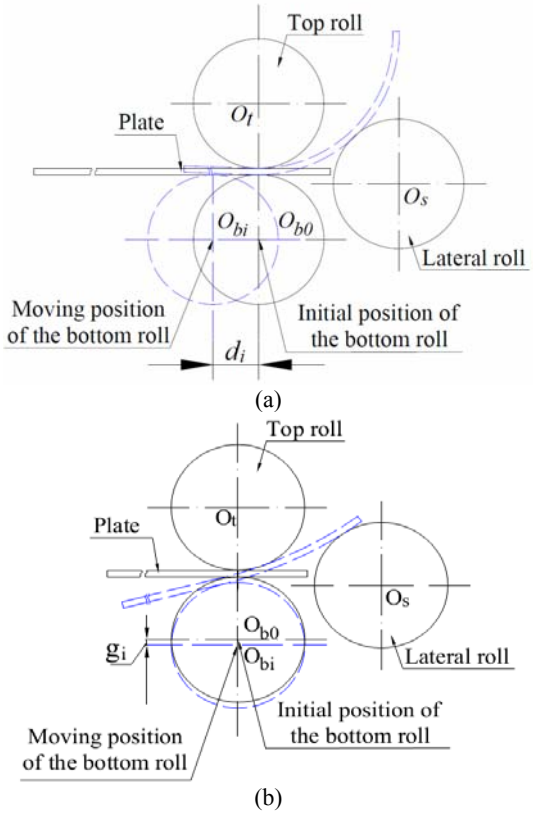

Fig. 2 Varying the location of the bottom roll: (a) offset d_i, and (b) "gap" value g_i.

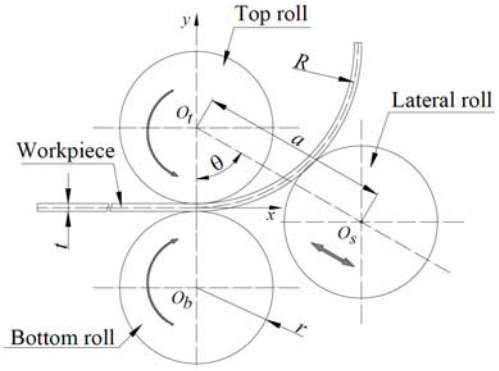

Fig. 3 Three-roll asymmetric bending machine.

The top roll is in a fixed position, while the bottom roll has an adjustable up and down displacement to pinch the workpiece and to allow for the removal of the finished workpiece. The workpiece is fed and "pinched" between the top roll and the bottom roll; the lateral roll location can be adjusted to achieve the desired radius of the final shape. At the end of the forming process, a cylindrical shape with a radius R is obtained if the length of the blank equals the developed length of the cylindrical shape and if the lateral roll is properly positioned. However, the workpiece must remain supported at all time by the rolls as mentioned previously. The process continually produces flat areas along the leading and trailing edges of the workpiece where the plate cannot be completely bent as shown in Fig. 4.

3. FEM of the Asymmetrical Roll-Bending Process

To study the flat areas produced by the roll-bending process, a 3D numerical FE model of an asymmetrical roll-bending machine described in the above section was developed in the Ansys/LS-Dyna software package. The FE model consists of four main components: three rigid rolls and one flexible plate, which are illustrated in Fig. 5. The rolls are considered to be rigid in comparison with the deformable workpiece.

To describe the nonlinear behavior of the stress-strain curve of the workpiece, a material model obeying the Ludwik-Hollomon equation is used for this nonlinear analysis. Ludwik-Hollomon's equation relates the stress to the amount of plastic strain as a power law.

$$\sigma = \mathrm{K}\varepsilon^{\mathrm{n}} \tag{2}$$

where,

σ: the stress;

K: material constants;

ε: the strain;

n: study hardening exponent.

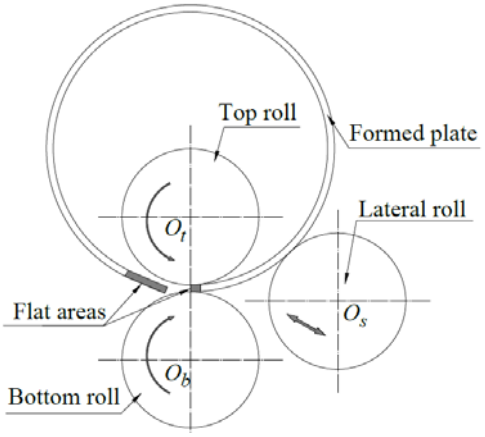

Fig. 4 Flat ends definition.

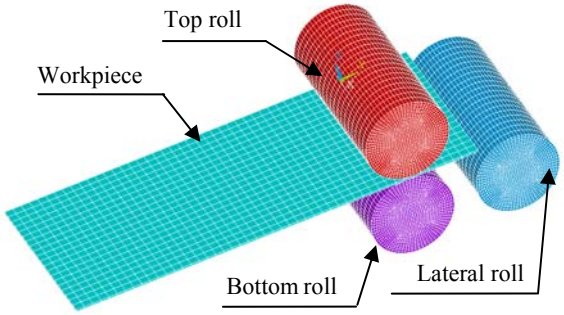

Fig. 5 FE model of the asymmetrical roll-bending process.

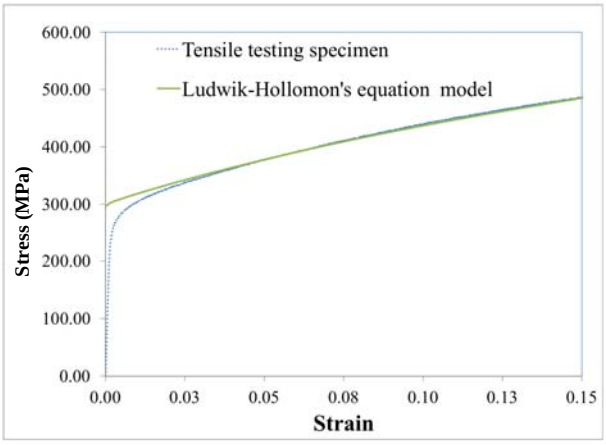

Fig. 6 Stress-strain curve.

The constants K and n are approximated by a curve fitting based on the results from a tensile specimen. Fig. 6 shows the stress-strain curves for the tensile testing model and the approximation model obtained by Ludwik-Hollomon's equation. The rate sensitive PLAW (power law) plasticity model in Ansys/LS-Dyna is applied to determine the stress-strain behavior of the workpiece.

The interaction between the rigid and flexible components is characterized through contact surfaces. In this roll-bending model, the surface of the roll is smaller than the surface of the blank. Although in the explicit analysis, Ansys/LS-Dyna supports a large number of contact options to define the interaction between the surfaces. The automatic node-to-surface algorithm was used for the interaction between the rolls and the plate because this type of surface contact is efficient when a smaller surface comes into contact with a larger one. In addition, the static friction coefficient (μs) between the plate and the rolls is directly measured via experiments.

For the boundary conditions, the top and bottom rolls are driven in rotation and fixed in translation. The lateral roll is constrained in translation and experiences no self-rotation to press the forming plate against the top roll.

4. Experimental Study to Validate the FE Model

To validate the FE model developed in Ansys/LS-Dyna, experiments are conducted using the same parameters on an asymmetric roll-bending machine. This instrumented roll-bending machine has three rolls with diameters of 100 mm, roll length of 1,500 mm and an operating action line angle of the lateral roll (i.e., θ) of 600 is shown in Fig. 7.

The final shape radius from the experiments obtained by the roll-bending machine is measured by an EXAscan laser scanner. This device is a hand-held laser system that allows for quick and accurate geometry data acquisition for verifying the characteristics of a formed plate.

Fig. 8 shows the flat ends at the leading and trailing edges of the cylinder shape in Ansys/LS-Dyna when the roll-bending process is completed.

To compute the flat-end lengths of the formed plate from the FE simulations in Ansys/LS-Dyna, a numerical procedure is applied as summarized in Fig. 9.

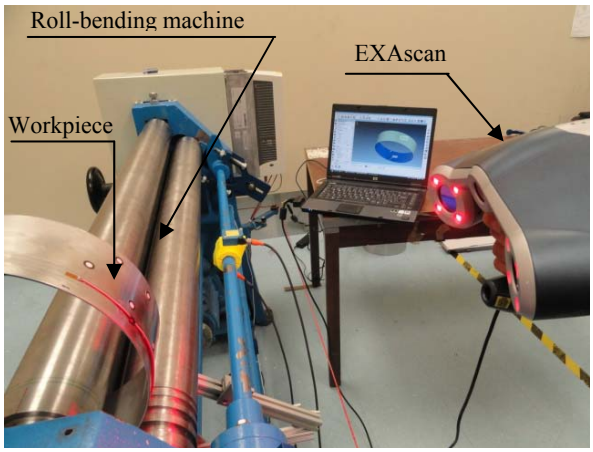

Fig. 7 Instrumented roll-bending machine.

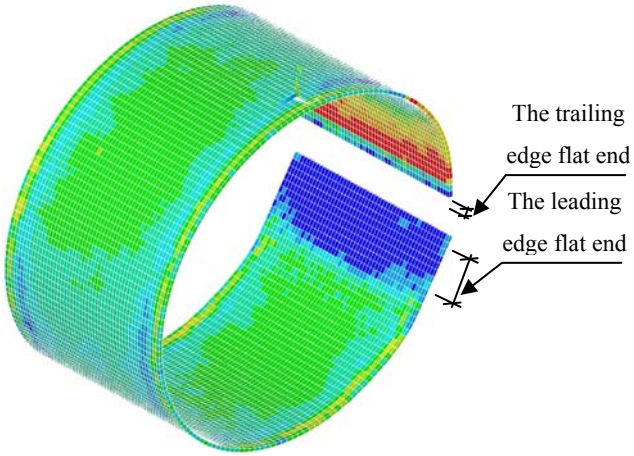

Fig. 8 Final shape obtained by the FEM.

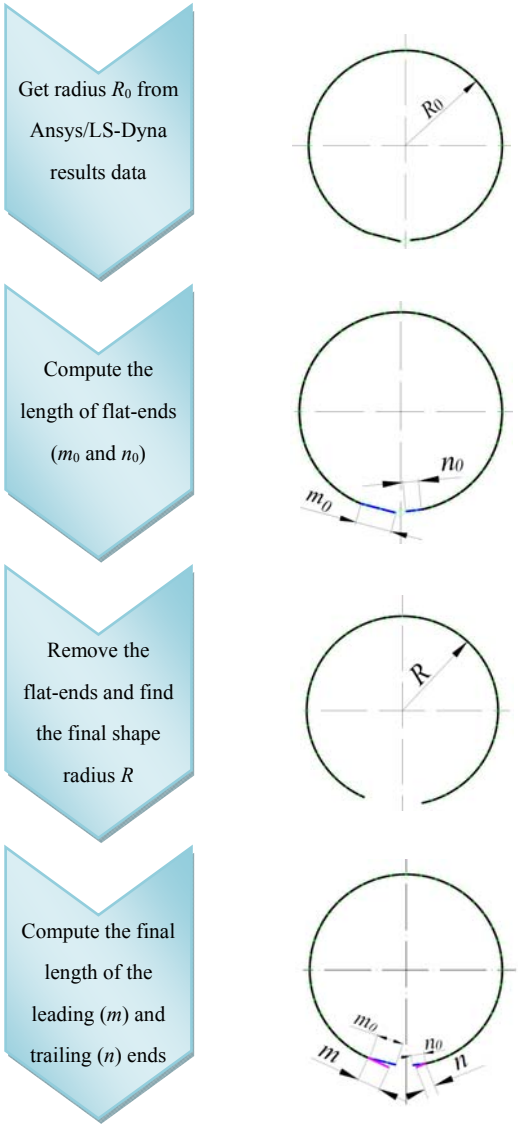

Fig. 9 Flat end and radius computational procedure.

Because the nodes of the formed plate are distributed along a cylindrical geometry, the coordinates of the center of the cylinder x_C, y_C and its radius R_0 are determined using the least-squares method:

$$\min F(x_c, y_c, R_0) \text{ with } F = \Sigma(R_0 - R_i)^2 \quad (3)$$

where,

$$R_i = [(x_i - x_c)^2 + (y_i - y_c)^2]^{1/2},$$

with $x_i = x_i^{(0)} + u_{xi}$ and $y_i = y_i^{(0)} + u_{yi}$.

With grad (F) = 0, three nonlinear equations are simultaneously solved for x_c, y_c and R_0. Only the initial coordinates $x_i^{(0)}$, $y_i^{(0)}$ and the displacements u_{xi} and u_{yi} of the nodes located at the mid-width of the plate are imported into MatLab® for numerical processing. A Newton-Raphson scheme is subsequently applied to determine the circle's parameters.

We assume that the nodes at the mid-width and at the trailing or leading edges of the formed plate in Fig. 8 are distributed along a geometry as shown in Fig. 10.

To determine which nodes at the leading or trailing ends belong to a straight line, based on a number of flatness criteria, a least-squares method was applied to compute the constants p_i and b of the best straight line $y = p_i x + b$ passing through nodes [1, 2, 3, …, i + 1].

With $\Delta = 0.2\ t/R$, the criterion for flatness, a node i + 1 is considered to belong to the flat end if and only if the new slope p_{i+1} satisfies Eq. (4):

$$|p_{i+1} - p_i| \le \Delta \quad (4)$$

The procedure is terminated when adding a new subsequent node does not satisfy Eq. (4). The final shape radius R is then recomputed following Eq. (3) with the remaining nodes, i.e., by removing the flat-end nodes from the initial node list.

It is costly to run a large number of experiments to study how the flat areas are related to the setup. Therefore, the idea is to compare the final shape radius R obtained by both the FE model and the experiment under the same forming conditions. The FE model is used to study the parameters affecting the extent of the flat areas. Fig. 11 shows comparisons of the final shape radius R for various plate thicknesses, i.e., t = 1.0, 1.5 mm, 2.0 mm or 2.5 mm for four different locations of

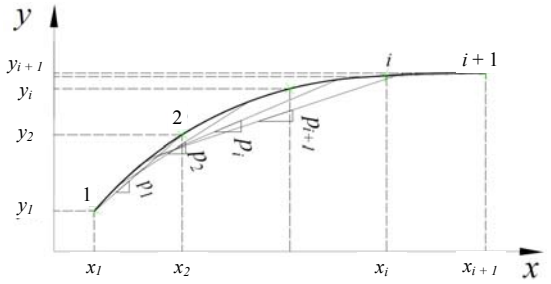

Fig. 10 Flat end lengths computational procedure.

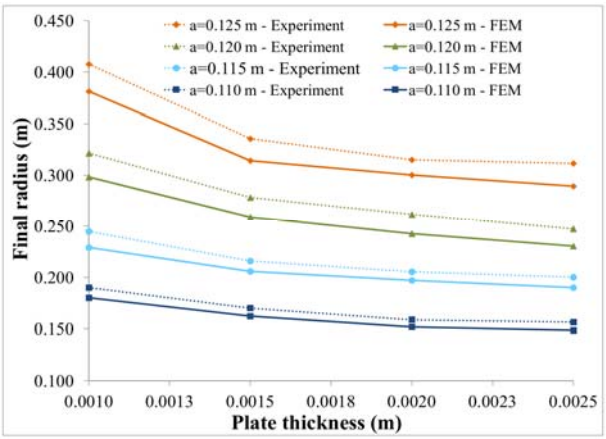

Fig. 11 Final radius dependence of the plate thickness and the location of the lateral roll.

the lateral roll, i.e., a = 110.0 mm, 115.0 mm, 120.0 mm or 125.0 mm. The final shape radii R obtained by the FE simulations (solid lines in Fig. 11) are slightly smaller than those obtained through experiments (dotted lines in Fig. 11). However, a deviation is observed with a highest difference of less than 8.0%, showing that the developed FE model is capable of accurately predicting the geometry of the formed plate.

5. Results and Discussion

The flat-end length for any given final shape obtained by the roll-bending process depends on the machine type, workpiece thickness, final radius, roll positions and even the operators' skills. In this study, correcting the position of the bottom roll of the roll-bending machine is considered as a method to reduce the forming forces and flat ends on the leading and trailing edges of the final shape. Correcting the positions of the bottom roll involves moving this roll in the horizontal plane and lowering it vertically. Although it is not possible to eliminate the flat areas inherent to the process, the challenge for future roll-bending machine designs is to minimize these areas.

5.1 Moving the Bottom Roll in the Horizontal Plane

To study the flat areas' dependence on the bottom roll positions, the FE simulations were performed using plates 2.0 mm thick, 100.0 mm wide and having a center to center distance "a" (Fig. 3) from the top roll to the lateral roll of 115.0 mm. While keeping the same input parameters, i.e., the roll radii, material properties, mesh, etc., the position of the bottom roll was moved to the left hand side for various distances d_i. Fig. 12 shows the values of the forming forces' dependence on d_i, which is expressed as a function of r, ranging from 10.0% to 70.0% of the bottom roll radius.

The forming forces, for both the top and bottom rolls, quickly decrease when the bottom roll is moved away to the left hand side by a distance d_i of 20% of r. The forces then slowly decrease when the bottom roll is moved to a distance d_i that is larger than 20% of r. Meanwhile, the forming force on the lateral roll (q_1) remains unchanged for every distance d_i. Fig. 13 shows the instantaneous free-body diagram of the system's roll-bending process, including the contact forces q_i and their respective angles θ_i. The equilibrium of the moments at point P_2 leads to Eq. (5):

$$\sum M_{(P_2)} = 0$$

$$\text{leading to } \; q_3 s_3 = q_1 s_1 \qquad (5)$$

where, s_1 and s_3 are the arc lengths of P_1P_2 and P_2P_3, respectively.

The contact angle between the rolls and the plate varies when the bottom roll is moved to the left hand side. However, the value of s_1 remains quasi-constant. This may explain why the forming forces of the lateral roll do not change in Fig. 12.

The flat ends for various positions d_i of the bottom roll are shown in Fig. 14. Knowing that the larger flat end is usually left at the leading end of the final shape [3], only the flat-end length at this edge is studied in this research.

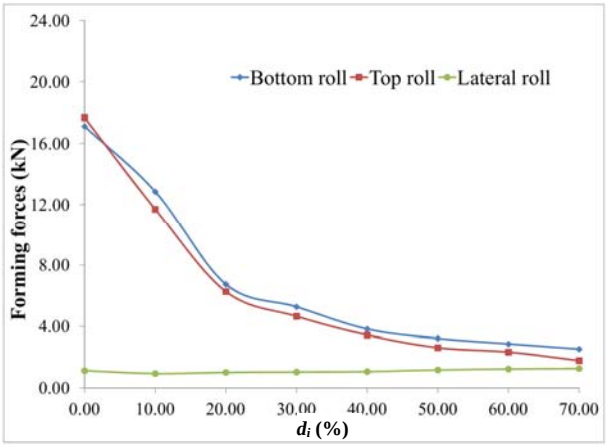

Fig. 12 Forming forces on the rolls versus the values of d_i of the bottom roll.

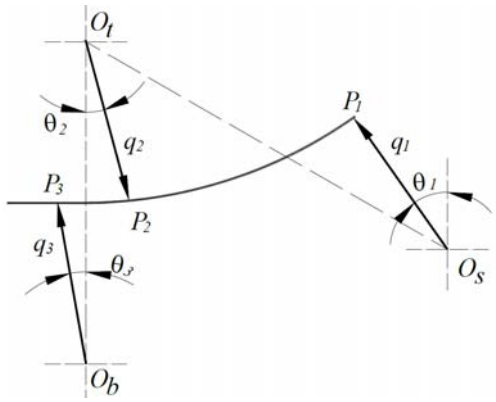

Fig. 13 Free body diagram of the roll-bending process.

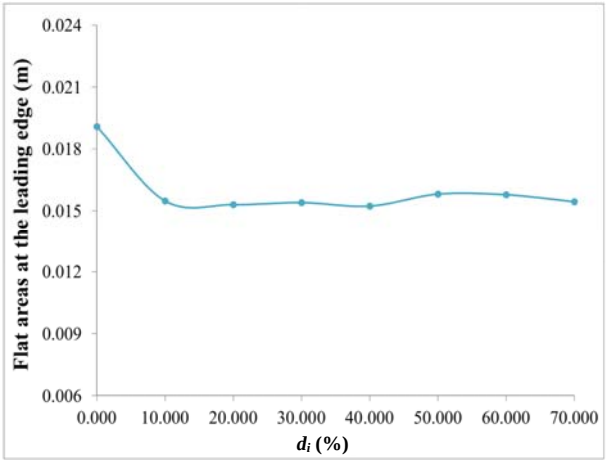

Fig. 14 Flat-end length at the leading end versus the distance d_i of the bottom roll.

The value of the flat-end length of the final shape was determined to be monotonically decreasing when the bottom roll is moved to the left hand side by a distance d_i of 10% of r. This is because at this position, the bottom roll is not only used to "pinch" the plate but, it is also used to support the plate at the contact line c (Fig. 15). The plate is therefore more efficiently bent with the lateral roll.

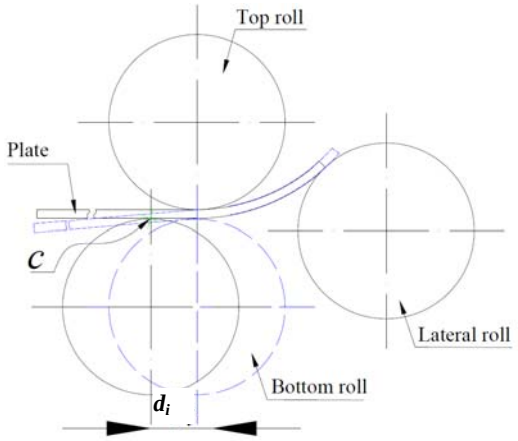

Fig. 15 Plate configuration when the bottom moves horizontally.

5.2 Moving the Bottom Roll in the Vertical Plane

The bottom roll of the three-roll asymmetric model was adjusted (up or down) in the vertical plane to compensate for the various plate thicknesses and to provide the pressure needed for "pinching". Therefore, choosing the matching "gap" between the top and the bottom roll is very important when using the roll-bending process. For example, if the bottom roll pressure is too tight, the final shape obtained may be a bell-mouthed shape. To avoid this defect, the bottom roll should leave a gap that is equal to or greater than the plate thickness.

To study the "gap" effect on the flat ends and the forming forces, a series of FE simulations were performed for various values of the "gap" g_i. These "gap" values range from 10.0% to 30.0% of the plate thickness. The center locations of the top and bottom rolls were placed on the same vertical axis. For this FE simulation, the forming parameters and the material conditions held constant were the 2.0 mm plate thickness, 100.0 mm plate width and 115.0 mm center-to-center distance "a" from the top roll to the lateral roll. The forming forces versus the "gaps" g_i are shown in Fig. 16.

The top and bottom forces tend to decrease when the

value of g_i increase. A rapid decreasing tendency is observed when the "gap" is set to 5.0% of the plate thickness. The forming forces then slowly decrease when the "gap" value continually increases, up to 30% of the plate thickness. The forming force of the lateral roll remains nearly constant for all the values of g_i.

Fig. 17 shows the flat-end length variation's dependence on the "gap" value g_i. The flat-end length monotonically increases when g_i is less than 15% of the plate thickness. Over this last value, the flat-end length is nearly unaffected when the "gap" continues to open.

This interesting phenomenon can be explained with the help of Fig. 18. The plate is held less firmly when the "gap" in-between the top and bottom rolls is larger than the plate thickness. For these cases, the plate tilts with an angle ε (dotted lines in Fig. 18), leading to a less bent plate.

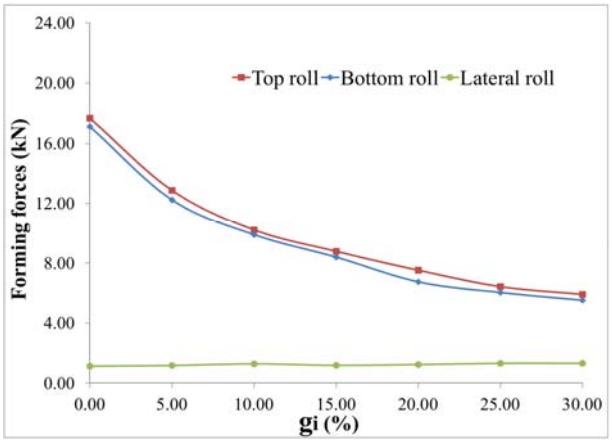

Fig. 16 Forces of the rolls versus the "gaps" values g_i.

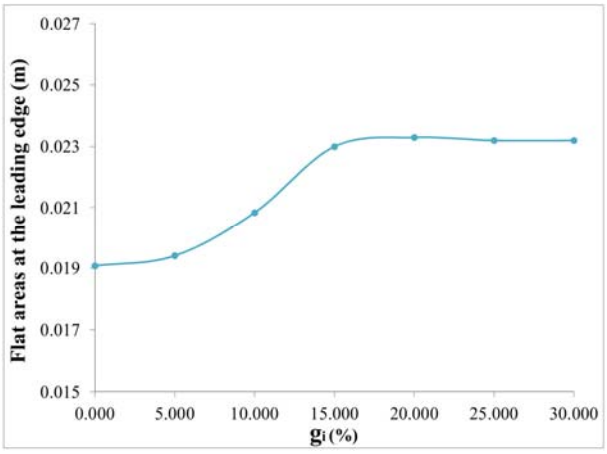

Fig. 17 Flat end versus the opening "gap" values g_i.

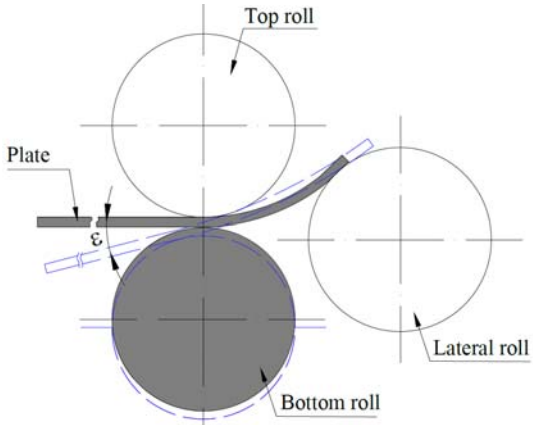

Fig. 18 Varying plate contact lines with rolls when moving the bottom roll downward.

Because the plate cannot be bent sharply, a larger amount of the blank at the leading edge remains flat.

6. Conclusions

A dynamic FE model was developed in the Ansys/LS-Dyna environment and was validated satisfactorily through experiments. In this study, we show how the flat-end lengths and forming forces are affected by the bottom roll setup. It is seen that by moving the bottom roll to the left hand side, the flat areas can be minimized, and the forming forces will be reduced on the top and bottom rolls. However, by adjusting the bottom roll with a "gap" value greater than the plate thickness in the vertical plane, the forming forces on the top and bottom roll are also reduced, but the flat area increases slightly. Therefore, in conclusion, maintaining the bottom roll at a gap close to the plate thickness and moving it laterally will produce the best results: lower forming forces and shorter flat-end lengths.

Acknowledgement

The authors express their thanks to the NSERC (Natural Sciences and Engineering Research Council) of Canada for its financial support during this research.

References

[1] Available online at: http:// www.thefabricator.com/article/bending/roll-bending-a-wind-tower-with-a-three-roll-bender.

[2] J.T. Black, R.A. Kohser, Materials and Processes in Manufacturing, John Wiley & Sons, New York, 2008.

[3] S.L. Semiatin, ASM Handbook: Volume 14B—Metalworking: Sheet Forming, ASM International, USA, 2006, pp. 386-393.

[4] O.D. Lascoe, Handbook of Fabrication Processes, ASM International, USA, 1989, pp. 48-52.

[5] M. Hua, K. Baines, I.M. Cole, Bending mechanisms, experimental techniques and preliminary tests for the continuous four-roll plate bending process, Journal of Material Processing Technology, 2nd Asia Pacific Conference on Materials Processing 48 (1-4) (1995) 159-172.

[6] M. Hua, K. Baines, I.M. Cole, Continuous four-roll plate bending: A production process for the manufacture of single seamed tubes of large and medium diameters, International Journal of Machine Tools and Manufacture 39 (6) (1999) 905-935.

[7] M. Hua, A formulation for determining the single-pass mechanics of the continuous four-roll thin plate bending process, Journal of Materials Processing Technology 67 (1-3) (1997) 189-194.

[8] M. Hua, Y.H. Lin, Effect of strain hardening on the continuous four-roll plate edge bending process, Journal of Materials Processing Technology 89-90 (1999) 12-18.

[9] M. Hua, D.H. Sansome, K. Baines, Mathematical modeling of the internal bending moment at the top roll contact in multi-pass four-roll thin-plate bending, Journal of Materials Processing Technology 52 (2-4) (1995) 425-459.

[10] M. Hua, Continuous four-roll plate bending process: Its bending mechanism and influential parameters, Journal of Materials Processing Technology 45 (1-4) (1994) 181-186.

[11] M. Hua, Y.H. Lin, Large deflection analysis of elastoplastic plate in steady continuous four-roll bending process, International Journal of Mechanical Sciences 41 (12) (1999) 1461-1483.

[12] W. Hu, Z.R. Wang, Theoretical analysis & experimental study to support the development of a more valuable roll-bending process, International Journal of Machine Tools and Manufacture 41 (5) (2001) 731-747.

[13] M. Yang, S. Shima, Simulation of pyramid type three-roll bending process, International Journal of Mechanical Sciences 30 (12) (1988) 877-886.

[14] M.B. Bassett, W. Johnson, The bending of plate using a three roll pyramid type plate bending machine, The Journal of Strain Analysis for Engineering Design 1 (5) (1966) 398-414.

[15] N.E. Hansen, O. Jannerup, Modelling of elastic-plastic bending of beams using a roller bending machine, Journal of Engineering for Industry, Transactions of the ASME 48101 (3) (1979) 304-310.

[16] J. Zeng, Z. Liu, H. Champliaud, FEM dynamic simulation and analysis of the roll-bending process for forming a conical tube, Journal of Materials Processing Technology 198 (1-3) (2008) 330-343.

[17] Z. Feng, H. Champliaud, T.M. Dao, Numerical study of non-kinematical conical bending with cylindrical rolls, Simulation Modelling Practice and Theory 17 (10) (2009) 1710-1722.

[18] Z. Feng, H. Champliaud, Three-stage process for improving roll bending quality, Simulation Modelling Practice and Theory 19 (2) (2011) 887-898.

[19] Z. Feng, H. Champliaud, Modeling and simulation of asymmetrical three-roll bending process, Modelling Practice and Theory 19 (9) (2011) 1913-1917.

[20] H.Q. Tran, C. Henri, F.Z. Kun, T.M. Dao, FE simulation of heat assisted roll bending process for manufacturing large and thick high strength steel axisymmetric parts, in: Proceedings of The IASTED International Conference on Modelling, Simulation, and Identification, Pittsburgh, PA, United States, 2011.

[21] H.Q. Tran, C. Henri, F.Z. Kun, T.M. Dao, Analytical modeling and FE simulation for analyzing applied forces during roll bending process, in: International Design Engineering Technical Conferences & Computers and Information in Engineering Conference, Chicago, 2012, pp. 207-215.

[22] H.Q. Tran, C. Henri, F.Z. Kun, T.M. Dao, Dynamic analysis of a workpiece deformation in the roll bending process by FEM simulation, in: 24th European Modeling and Simulation Symposium, Vienna, Austria, 2012, pp. 477-482.

[23] H.Q. Tran, Heat assisted roll bending process dynamic simulation, International Journal of Modelling and Simulation 3 (1) (2013) 54-62.

[24] H.Q. Tran, C. Henri, F.Z. Kun, T.M. Dao, Dynamic FE analysis for reducing the flat areas of formed shapes obtained by roll bending process, in: ASME 2013 International Mechanical Engineering Congress & Exposition, San Diego, CA, 2013.

[25] Y.C. Zhong, W.L. Ying, Analysis on the straight-end problem in thin-plate three-roll bending, Applied Mechanics and Materials 80-81 (2011) 585-590.

Journal of Mechanics Engineering and Automation 4 (2014) 476-487

Analysis of the Approach on Usability and Ergonomics in Handling and Transporting Packaging

Marília Colozio Favaro, Adriana Yumi Sato Duarte and Franco Giuseppe Dedini

Laboratory of Integrated Systems, Faculty of Mechanical Engineering, State University of Campinas, Sao Paulo 13083860, Brazil

Received: April 15, 2014 / Accepted: May 13, 2014 / Published: June 25, 2014.

Abstract: The purpose of this research is to explore the principle of the man-object relationship to identify the issues shown when handling packaging and emphasizing the usability aspect. For that, the theoretical reference of the research involves the analysis of the parameters according to the aspects that involve the use interactions of packaging in agreement with the definition and scientific concepts of ergonomics, allied to the development of product projects, discussing forms, handling, load transportation and the support of the product. Therefore, improperly handling of the packaging may cause damages to the products and even potential accidents. Coding and decoding are significant to facilitate the use recognition within the individual's repertoire. The packaging, within the macro-ergonomics universe, may be the object of ergonomics, whose contribution to solve problems is related to labor activities, by dealing with packaging, transportation and load resulting from the man-object interaction. The incorrect identification of information may lead to problems of interpretation and misuse, from the handling to the disposal of packaging. For this reason, this research suggests the adjustment of the man-object interface which may lead users to make mistakes regarding use and important choices, through adequate handling actions.

Key words: Man-object, handling packaging, usability, packaging, product development.

1. Introduction

Ergonomics is the term that designates the multidisciplinary application of knowledge to deal with a series of cautions involving men and the inherent particularities of each task performed under labor conditions, observing the individual characteristics and limitations. For such, this study must be more broadly interpreted, not only in relation to physical effort, but in all dimensions. Only then the objective of maximizing the results of this study and minimizing effort, fatigue and potential harm to the integrity of human health will be reached.

The adjustment between object and information is a reference for the man-object interface. Non-significant codes and denominations may lead users to make mistakes regarding the use and important choices. Coding is meaningful so that there is an easier recollection and use recognition [1].

The study of the symbols and identification of the problems that may occur due to the inadequate use of packaging was based on the man-object analysis. The user's experience in relation to the object suggests principles for a good design, building a psychological method to interact with the objects, based on principles are highly inter-relational with other areas or other terms [2].

Usability is the capacity that an interactive system offers to the user, within a specific context, in order for the task to be effectively, efficiently and comfortably performed, and it determines specifications and evaluations emphasizing the performance and satisfaction of the operator/user. Partially, multidisciplinarity is essential for its correct use during the project's conception.

The packaging has a fundamental role to protect the products' quality, in addition to making their transportation feasible, in order to perfect sustainably

Corresponding author: Marília Colozio Favaro, master, research fields: packaging, product development and design methodology. E-mail: mcfavaro@fem.unicamp.br.

the product's distribution chain. The project methodology guides this study due to the complex network of variables involved, mainly because this is a multidisciplinary theme.

The objective of this research is to show the definitions on the theme, elaborating a discussion on the different study branches involved with this concept and finally, elaborating a theoretical analysis suggesting an adjustment of the man-object interface, in which information is the reference for the non-significant codes and denomination, considering that they may lead the user to make mistakes as to use and important choices through adequate handling and transportation actions. Thus, the approach to Ergonomics is justified, especially regarding usability with the purpose of contemplating these new parameters.

The paper is organized as follows: Section 2 presents the research scenario, introducing the ergonomics and usability concepts, packaging technology and transportation; Section 3 analyses and discusses the ergonomic factors applied to the handling and transportation of packaging; and Section 4 presents the conclusions and emphasizes the importance of ergonomics for comfort and safety.

2. Research Scenario

The purpose of this section is to discuss the main research themes: packaging technology by function, shape and classification, the importance of the ergonomics parameters, specifically usability and handling to perform a specific task.

2.1 Ergonomics

Thus, the word Ergonomics comes from the Greek words ergo (work) and nomos (rules) and, in some other territories, it may be found with the denomination human factors, and it is applied to the design of machines, equipment, products, tools, systems and tasks with the purpose of improving the safety, health, comfort and efficiency of the work.

The purpose of Ergonomics is always to adapt or adjust the object in the best possible way to human beings in general, in relation to safety, comfort, and use efficiency or operational handling of the objects, in activities and human tasks [3].

It can be said that Ergonomics is the source of usability, since the purpose of both is to provide efficacy, efficiency, well-being and health to the user by adapting his/her way of thinking. The Brazilian Association of Ergonomics (ABERGO) [4] adopts the definition of "Ergonomics as the study of interactions between people and technology, the organization and the environment, aiming at interventions and projects to improve, in an integrated and non-unrelated manner, the safety, comfort, well-being and efficiency of human activities".

Thus, Wisner [5] defines Ergonomics as "a set of scientific knowledge related to humans and necessary to create tools, machines, and devices that may be used with the utmost comfort, safety and efficiency". For Grandjean [6], Ergonomics may be defined as "the science of configuring work adapted to humans". In the beginning, the configuration of tools, machines and the work environment was considered.

According to IEA (International Ergonomics Association [7]), Ergonomics (or human factors) is the scientific discipline related to understanding the interactions between humans and other elements or systems, and to the application of theories, principles, data and project methods, in order to optimize the human well-being and the global performance of the system.

Among the characteristics of Ergonomics, we may mention three types of approach: Physical Ergonomics, which involves several human characteristics; Cognitive Ergonomics, which involves cognition processes; and Organizational Ergonomics, which involves the social-technical elements.

However, the basic objectives of Ergonomics are the ones that encompass health, safety and satisfaction of the worker, which is the consequence of an

adequate planning and work organization.

Human posture is the decision to keep the body in a desired position related to biomechanical matters [3]. General biomechanics studies the interactions between work and man under the perspective of skeletal muscle moves. Iida [8] states that Occupational Biomechanics is part of General Biomechanics and, thus, Gomes [3] emphasizes that it studies the interactions between man and work under the perspective of skeletal muscle moves.

Therefore, the activities performed at work may be shown as follows:

• Static work—the one that requires continuous contraction of some muscles, in order to maintain a certain position;

• Dynamic work—the one that allows for alternate contraction and relaxation of the muscles.

The force applied may occur in several different ways, such as pushing, pulling, squeezing and pressing among others, which will depend on the work performed [8]. The number of people with spinal problems is increasingly higher. Several studies in many countries have shown the relationship between the handling activities and manual material handling and the incidence of a large number of accidents and osteoarticular lesions, mostly in the lumbar region [6].

Whenever possible, the control moves must follow the natural moves that are more easily performed by humans. Based on the Ergonomic principles, machines and tools are considered as an extension of men. The man-object interaction contributes to reduce mistakes, ergonomic stress and accidents in order to improve the performance of the system in which it is inserted. All the moves made by the human body with the purpose of transmitting some form of energy to the machine (usually performed with the hands and the feet) are called control movement. Therefore, the hands must make paced moves, through a curved and continuous orbit, avoiding sudden changes and harsh interruptions [8].

Ergonomics makes use of Biomechanics which consists of analyzing the mechanical bases of biological activities directed towards the human muscle-skeleton system in order to study the human body's posture at work, application of force and handling.

The movement of body segments is defined as "the angular displacement around an imaginary rotational axis that goes through the articulation to which the segment is connected" [9]. For lifting and manual material handling, the weight on the spine must be applied towards the axis and close to the body, in order to hinder perpendicular components from appearing as shown in Fig. 1.

Load transportation may cause two types of reactions on the user: the overweight causes an excessive physiological load on the spinal muscles and the lower limbs; and the postural stress, caused by the body's contact with the load. Consequently, pain, discomfort and ergonomic stress are caused. The product development together with Ergonomics looks for efficient alternatives to transport load that would reduce energy use and muscle-skeleton problems. Adopting alternatives such as keeping the load close to the body, adopting an adequate value for the unitary load, using symmetrical loads, projects such as adequate handling, teamwork, defining the path to be

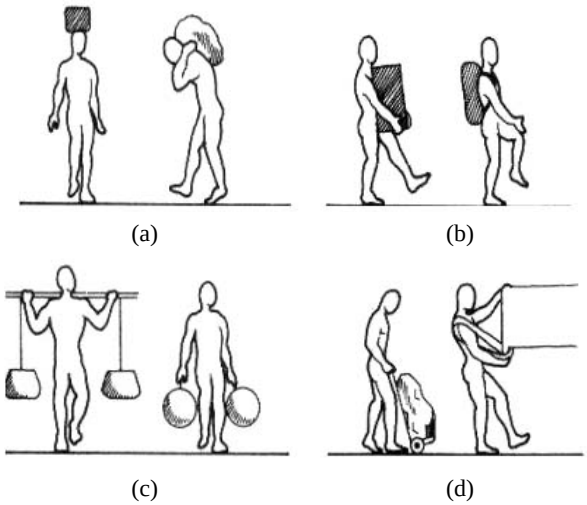

Fig. 1 Manual handling: (a) vertical load; (b) close-to-body load; (c) symmetrical loads; and (d) use of auxiliary means [9].

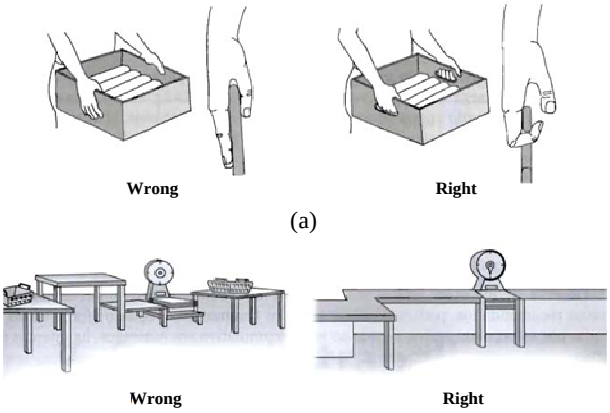

Fig. 2 (a) Material handling; (b) unevenness at the work area [8].

taken, leveled floors, use of mechanical carriers (Fig. 2), may avoid excessive effort of the dorsal muscles among other traumas caused by impact.

The operator is subject to actions such as lifting, bending down, pushing, pulling, holding and transporting load to perform a certain task. The elements that constitute this manual material handling system require the operator (defined due to his/her physical, sensorial and psycho-motor characteristics); the material (load), which has mechanical and geometrical characteristics, handling and stability, task and work space divided into geometric, temporal, complex and environmental characteristics; and work practices to be performed, which may be individual, organizational and administrative.

There are general handling classifications that are divided into two basic types [8]:

• Fine manual handling or precision handling: the moves are transmitted by the fingertips, while the palm of the hand and the fist remain still. It is characterized by great precision and speed with little force transmitted during the moves;

• Manual handling or force handling: the moves are performed with the center of the hand, keeping the fingers still and with the grasping function, while the moves are performed by the fist and arm. It transmits stronger forces, with lower speed and precision than in fine handling.

The handling design is completely relevant for the performance in the man-object system, considering the handling types. For fine manual handling, smaller shapes than the ones used for manual handling are needed. These shapes are classified into geometric and anthropomorphous.

The geometric handling is characterized by regular shapes, such as cylinders, spheres, cones and others. Since they differ from the human anatomy, they have little contact surface with the hands. Due to the use flexibility, which allows handling variations, it is easy to adapt to the variations in anthropometric measurements. However, tensions are concentrated in certain parts of the hand, interfering in the force transmission and making it hard to perform the move. Despite being less efficient, this type of design works better if applied to operations that do not require major force.

In the anthropomorphous handling design, the surfaces are round-shaped, adjusting to the hand anatomy due to the fitting depressions or saliences, which are referred to as “anatomical”. It shows greater contact surface and handling stability in relation to geometric handling, transmitting greater force and concentrating less tension, but it is ergonomically stressful if used during long hours due to the limited position. Therefore, this kind of design shows a better performance when used for short-term tasks, which require little moves, need greater force, as well as when the users show similar anthropometric measures.

The object’s superficial finishing may interfere in the handling and task performance, since each type of handling (fine manual handling and manual handling) requires an adequate surface, which, otherwise, may be harmful, since pressures are concentrated on those spots. Data show that the use of “manual tools” is related to cumulative trauma on the users’ hands and forearms [8]. A diagram shows the painful areas of the hands, fist and forearms, according to Fig. 3.

In order to avoid any type of ergonomic stress when performing the work, the tool must be adequately

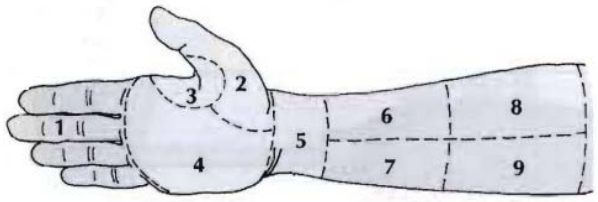

Fig. 3 Diagram to survey the painful areas when using manual tools [8].

chosen, based on its functionality, and they must be selected according to the task to be performed, followed by the ergonomic characteristics that ensure the operator's comfort and safety. Such characteristics depend on two factors [8]:

(1) Handling characteristics: the differences in the handling methods must be considered, the transmitted moves (force, speed and precision), possibility to use both hands and adjustment for left-handed people. These measures allow the reduction of tension on the hands, as well as a better handling design and greater handling diameter eliminating angular surfaces;

(2) Center of gravity: the tool's center of gravity must be located as close as possible to the center of the hand, allowing better motor control in order to reduce moves and consequences, muscle efforts and energy use during the operation.

A large number of parameters are observed, trying to combine the advantages and disadvantages of each one, in order to soften the handling rigidity and increase the contact area.

2.2 Usability

Oftentimes, incompatibility problems on a same product cause all the improvement to be left aside, forcing the user to keep on using methods that he/she already knows. However, the user needs autonomy to demand functionality and make easy use a priority.

Usability depends on the specific characteristics of the object's interface and the user in the determining sense of the objectives applied to the use situation. The same interface may be satisfactorily interpreted for old users, but it may not be as satisfactory for new users. The essence that designates the use is in establishing a relationship between interface, object, user, task and environment [1]. The current concept is excessively involved to the cognitive aspects of the task, focusing on experiences and individual characteristics, abilities and emotional perception, which approaches a need to enrich a usage concept [10].

Partially, the social and behavioral sciences are fundamental in order to make use of usability for the design's conception, where four principles are used, involving the user and the task requirement. According to ABNT (the Brazilian Association of Technical Standards [11]) NBR 9241-11, usability is the "measure according to which a product may be used by specific users to reach specific objectives effectively, efficiently, and satisfactorily in a specific use context". To better clarify, the concepts described are defined as:

• Efficacy—accuracy and completeness with which users achieve specific objectives;

• Efficiency—resources spent regarding the accuracy and reach with which users achieve objectives;

• Satisfaction—lack of discomfort and presence of positive attitudes towards the use of a product;

• Usage context—users, tasks, equipment (hardware, software, and materials), and the physical and social environment in which a product is used;

• User—a person who interacts with the product;

• Objective—intended result;

• Task—set of necessary actions to achieve an objective.

Therefore, what the standard dictates on the use of a certain objective (or system) can be noticed, taking into consideration its relationship with the user. Within this prism, it can be said that the term usability comprehends any relationship between the user and the environment, and the main subject matter is the interface between them and any of its consequences on the person, the object and/or the environment.

Usability, when considered as a usage quality, is not only an aspect of the product's quality, but a consequence of the interaction between user and the product when performing a task in a certain context [12].

In the beginning, the study focused on the machine and the worker should adjust to it. The workers were selected and qualified according to the specific demands and characteristics of the machines, making the worker engage into long periods in the learning process.

Afterwards, in relation to the problems detected by human mistakes, a study that focused on the man was established. No attempt was made to modify the machines, taking into the limitations of men consideration. Finally, a system was conceived in which the man-machine interaction, specifically the man-work interaction, is taken into consideration.

Considering the orientations of the ergonomic parameters for load mobilization, it was shown that manual work may cause severe health problems due to the operator's bad human posture. However, alternatives were created to relief the load's weight on the spine, that is, wheel carts, stackers, load unification packaging; these are accessories that intend to relief the excessive weight on the user, in addition to optimizing the process. However, even with this type of mechanical work, human posture and handling actions must be applied, since the static work may be ergonomically stressful, and a bad sitting posture may cause irreversible damages to the spine. Thus, attention must be paid to the ergonomic parameters, in order for the product design to abide to the standards, offering better work conditions and comfortable safe and efficient man-object interaction.

Within the context of the man-machine system, Chapanis [13] points out that people are used or involved in any system of equipment, because the systems of equipment are at all times elaborated according to some human objective. They are there to meet a certain human need. In addition, the systems are planned and built by human beings. Human creatures handle them, oversee them, observe how they work and take care of their maintenance. The man-machine system is the system of equipment in which at least one of the components is a human being, who acts or intervenes in the operation of mechanical components of the system at all times.

In man-machine systems, people are used or involved in any systems of equipment, considering that they are at all times elaborated according to some human objective. They are there to meet a certain human need, and are developed from one human being to another. "It is the system of equipment in which at least one of the components is a human being, who acts or intervenes in the operation of mechanical components of the system at all times" [13]. Under this perspective, a product that is considered as non-usable within a system may be used for another, since usability does not depend only on the characteristics of the product, but on the user/environment relationship [10].

2.3 Packaging

The term "packaging", which comes from the verb "to pack", "the act of conditioning (good or objects) into packaging, packs and boxes, etc., in order to protect them from risks or facilitate their transportation" [14], has as its primary role protection and transportation. As humans became aware of their basic needs to eat, store and preserve food for a longer time and, as the distance between the supply sources increased, reaping and hunting were no longer enough, they needed to store and transport [15].

The Brazilian Ministry of the Environment [16] on DL 366-A/97 defines packaging as "all and any products made from materials of any nature used to contain, protect, transport, handle, deliver, and present goods, both as raw materials and as transformed products, from the producer to the user or consumer, including all the "disposable" alternatives used for the same purposes".

The Brazilian Packaging Association [17] determines that packaging is every container or wrapping that stores products temporarily, individualizing or grouping units, with the main role of protecting them in order to extend their shelf life, enabling their distribution, identification and consumption. Understanding packaging as the creation process, its efficiency and performance are verified according to the product's success, which implies the adversities of creation, interpreted as a technical object, with a particular role and characteristics [18].

However, the packaging is a thin line between the product's design and the graphic design, since both aspects are complementary and merged into three different levels: primary, secondary and tertiary [14] as represented in Fig. 4. The primary packaging design is directed towards the consumer, has a market appeal, good shelf arrangement and protects the process [21]. It is responsible for preserving and maintaining the product.

In the case of the secondary packaging, cardboard boxes, bags or casks are usually focused on logistics to offer greater handling efficiency and used to group products which are called secondary packaging. The purpose of this kind of packaging is to avoid damages upon the product's handling and storage [21].

In the tertiary packaging, the design is developed aiming at the collective transportation of the previous packaging, focusing on the protection against damages caused by the journey, prioritizing the quality of the product that will get to the end consumer. This type of packaging is usually made from a coarse material, corrugated cardboard, plastic and wood. For this type of packaging, the visual astatic is not a relevant factor since it does not get to the consumer.

The combination of these levels, due to the characteristics of the products, applicability and marketing image, guides the parameters of the product's development. The importance of this segment is due to the different roles of each one of them. The primary packaging must protect and

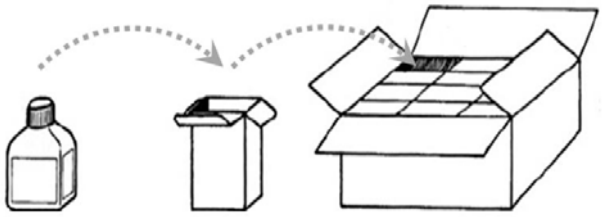

(a) (b) (c)

Fig. 4 (a) Primary; (b) secondary and (c) tertiary packaging [14].

preserve the chemical and physical integrity of the product, minimizing the absorption of gases (oxygen, carbon dioxide), humidity, odors and light among others; secondary and tertiary packaging must also help in the transportation, grouping them or optimizing mechanical aspects, protecting the product from shocks, vibrations, falling and pressure, etc., and they oftentimes work as a reinforcement [14].

The means of transportation, the level of vibration suffered during the displacement and handling of the product, the stacking height, humidity and time of stocking, among other factors, are cost-efficient, since when the lowest possible amount of material is used, the costs are reduced, increasing the number of products transported at once, and restricting investments on transportation and storage. A more resistant packaging reduces losses due to damages and stability, and offers a safer stacking. These measures are relevant considering ecologic factors, minimizing the post-use tear.

2.4 Product Design Methodology

In product design, information such as the product's stability and the degree of frailty or sensitivity is essential to define the level of protection the packaging will provide, considering the mechanical, chemical and electric stability.

The impacts and mechanical vibrations occurred during the transportation and shifting of the products are the main responsible factors for the damages incurred. That includes manual or equipment-based shifting, such as through conveyor belts, carts, stackers and lifters, etc., requiring adequate packaging [19].

The packaging development may be referred to as the act of going through a path established by the project's methodology, meeting the packaging's specificities in relation to the other industrial products, and it must be considered as a whole, that is, the context in which the product is inserted is a relevant factor for the product's development [19, 20].

In order to develop the packaging's design, the needs and simultaneities between the product's design process and the packaging's design process must be integrated. In order to develop new designs, the model is previously filled with current information on technologies, marketing researches, information products and environmental impact processes, materials, competitive intelligence, evaluation of the packaging' life cycle, in order to meet the environmental and strategic goals established [22].

The product's development is a multidisciplinary process and, as such, it needs different perspectives and expertise in order to be complete. Engineering conceives the product from a technical-physical system, with an efficient and safe operation. The design understands that the product has different roles and therefore, its good operation depends on their interactions. The design, as opposed to the common sense, is not only related to the aesthetic and symbolic aspect [23].

Another key factor for the process of developing a product is the methodology and tools used. The discussion concerning a universal definition for the term "product design methodology" shows that the acquired meaning depends on the author and the applicable area; it is generally related to the process of directing resources both financial and human to meet the defined goals.

By systematizing and describing a methodology, Asimow [24] started a discussion on the theme, and it opened a precedent for other authors to change and adapt the methodology according to the existing needs during each period, as shown in Fig. 5.

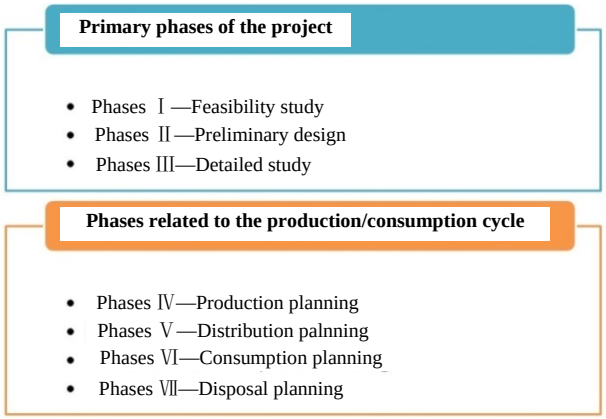

Fig. 5 Methodology [24].

2.5 Moving Packaging

The objective of the design of a packaging made for transportation is to protect the product during transportation against external agents, such as mechanical shocks, dust and humidity, etc., and add several unities making the transportation, handling and storage easier.

Some aspects must be considered when specifying the packaging for transportation, such as [19]:

(1) the total weight must be adequate to be carried by one person;

(2) using closure systems that inhibit the opening as a safety measure to prevent theft;

(3) use of details that assist in opening the packaging at the point of sale.

These recommendations facilitate the use by consumers, who demand improvements on the design of packaging, such as using details that make it easier to open them. The type of material and calculating the packaging's resistance refer more to its resistance upon handling; therefore, each product has a type of specific packaging according to the context in which it is inserted. In large volume productions, the packaging need to be mechanically handled, considering as design requirements the material, tolerances, the closure system, and internal accessories.

The packaging for frail and hazardous products needs a more robust design. In the case of frail products, especially those that add value, the primary packaging must be reinforced to avoid the use of an extra packaging, exclusively for transportation, since, in addition to affecting the aesthetic; it increases the

product's total cost. To transport hazardous products, the packaging must meet the national and international safety standards that define risk levels, material specifications and tests for approval.

The packaging that protects the product during the different transportation methods joins it from the factory up to the end user or distribution center. During the transportation, unifying the packaging involves the concept of packing or arranging several volumes of goods to create a since standardized "unit" in order to be mechanically moved along the process, serving as the basis for a chain constituted by an integrated system involving packaging, shifting, storing and transporting materials. Thus, it saves more time during displacement, in addition to protecting the product, since it is possible to see whether the volume was violated. The most used unification method is palletization, which consists of arranging upper and lower boards, connected by ring or spiral nails, adding glue (optional) to offer greater fixation; the pallets must be well aligned in order not to deform the cardboard packaging, as seen in Fig. 6. Pallets must be standardized according to the project's specifications.

Another unification method used is the slip sheets platforms, used as an accessory for the stacker during the transportation. With a solid or corrugated cardboard base and two lids measuring about 7 mm thick, the space taken by the packaging is minimal, and they offer another advantage which is the reduced cost in relation to any type of pallet. For this system, a stacker with a special accessory or adequate machines must be used, according to Fig. 7.

The main characteristic of singulators is the repetitive use (except for the one-way ones), and these devices allow carrying and lifting loads through self-bearing fittings. The main unification method used by industries and warehouses is palletization, due to the pallets' transportation flexibility in automotive vehicles, airplanes, ships, railways and containers [25]. Other methods that are mostly employed for unitization are pre-language means, used for sacks, which consists

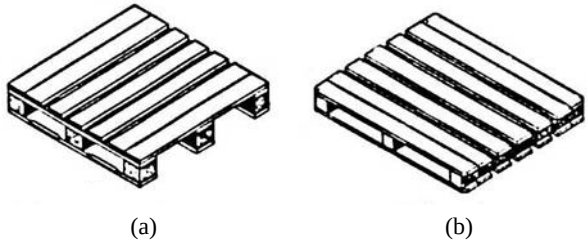

Fig. 6 (a) Four-way entry simple pallet and (b) two-way entry pallet with lids [19].

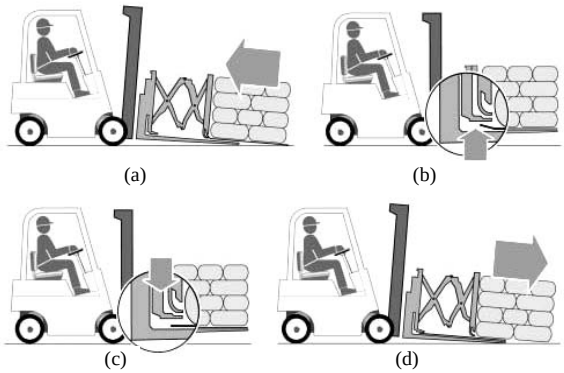

Fig. 7 Moving consolidated load units, such as slip sheet [19].

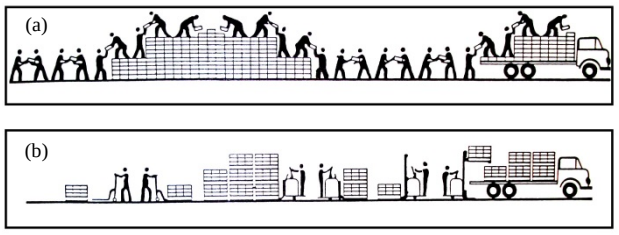

Fig. 8 (a) Manual vs. (b) mechanical transportation [25].

in tying up an object or set of objects, involved by nets or belts with lifting handles, and load self-unitization by strapping, block-stacking or bundling. Among the methods used to promote load stability during transportation or stacking, a highlight is the use of lifting devices introduced beneath the load, load compression between two surfaces and load suspension.

Fig. 8 represents the use of the unified method in comparison to the individual load handling system, showing the characteristics of each application.

The advantage of using the load unification method together with the shifting and stocking system is that it makes it easier to stack loads on top of each other,exploring the tridimensional plan by reaching considerable heights. In addition, it offers

cost-efficient benefits for the manufacturers, shippers and consignees (facilitating price quotation) and transportation companies by increasing the operational speed of the transportation vehicle and the productivity and reducing the load shifting costs. Other advantages of applying the system are the reduced damages to the load, lower transit time and incidences of theft and reduced stock. However, it has disadvantages when it comes to controlling and returning the empty singulators.

3. Theoretical Analysis of Usability and Ergonomic Factors Applied to the Handling and Transportation of Packaging

For almost all operators, using mechanical transportation and packaging during transportation means no longer having to perform a dynamic work, which requires daily physical efforts when handling these objects. A few of them, however, know that a smooth-surfaced packaging, burred texture, overweight of the packaging exceeding the advisable limits, or even a stacker's seat may lead to discomfort ad even physical problems.

Several problems may arise when adequate tolls and objects are not used according to the characteristics of each person. There are several items that must be adjusted to each person, including:

(1) Chair: it must have a high backrest with arm support at the same height of the machine's panel. It needs to be precisely positioned on the lumbar curvature, supporting the spine;

(2) Height of the transporting cart: it must have an independent height regulation. The elbows must be at a 90° angle in relation to the body;

(3) Workbench unevenness: the upper part must be at the same height than the eyes at a minimal distance of one arm in order to make the head to be vertically positioned and avoid irregular surfaces that force the user to move the legs. Instead, he/she should be positioned in order to be only able to rotate the body around its own axis;

(4) Shape of the packaging: surfaces must offer a steady handling to prevent the operator from using a handling method that uses excessive weight;

(5) Packaging stacking: packaging stacking must be avoided in manual handling due to spinal overload; the ideal scenario is using mechanical transportation.

The problems with packaging handling are not only related to bad human posture or with the use of inadequate equipment. The type of task and the process performed by the operator must also be taken into consideration. Overly ergonomically stressful and long tasks that require concentration to be performed reduce the operator's attention and result in physical and mental fatigue.

Several problems may arise when the work environment specifications are not being followed:

(1) Fatigue: reduced performance and work capacity. It is caused due to a change in the properties of the muscles, local intoxication or due to long and uninterrupted work hours;

(2) Backache: caused by the use of overweight and tools those are not adapted to the person. Na inadequate chair is the main factor that causes backache. The chair's backrest needs to be precisely positioned on the lumbar curvature, supporting the spine. The backrest must also be flexible in order not to allow the operator to slip backwards;

(3) RSI（repetitive strain injury): caused by the excess of repetitive movement, going back and forth through the same path, incorrect handling, machine control panels, and mainly when the load is not being transported using a correct posture. In some cases, RSI may be restricted to the affected limb, usually hands and arms. In an earlier phase, inflammation occurs, requiring immobilization and adequate medication. Depending on the quality of the resting period which should last for some months after the patient has been mobilized, he/she may or may not be able to get back to work. Some workers experience pain only five minutes after resuming the work they used to do, other take hours, and other months.

Therefore, in order to analyze the task detailing the work procedures to make it efficient, some questions should be considered:

- Which actions are employed on the interface of the work tools and by humans?
- How do they work to reach their goal?
- Which situations must be foreseen whose use may cause risks?
- In which physical (spatial and temporal) conditions the operator and his/her instruments are involved?
- Which psycho-social relationships are there on this man-equipment/object interface in relation to shape, color and texture?
- Task description.

Questioning and surveying these data is completely relevant to develop new packaging and instruments to facilitate transportation in order to offer greater comfort for the operator, avoiding ergonomically stressful and repetitive moves, as well as energy use that may cause discomfort and severe diseases with time. In order to make the workers execute their activities, they perform varied types of body moves required by the actions, involving all of their limbs (speed, force, precision and duration); and the characteristics and types of controls used on the equipment (buttons, levers, wheels and pedals).

According to Ref. [8], the force may be directed towards pushing or pulling. In general, the force applied by humans to pull and push varies from 200 N to 300 N. However, if the weight of the body and the strength of the shoulder are used to push, this value reaches 500 N. In vertical reaches, the position causes ergonomic stress on the muscles of the shoulders and biceps; pain may also occur and be increases according to the time required for the exercise.

In relation to horizontal reaches, due to the distance between the weight and the shoulders, more is required from the muscles of the shoulders. In this position, as well as in the vertical position, the arms have to overcome certain resistances, and that is when ergonomic stress and pains occur and these positions are held for a long time.

In relation to load lifting, some care must be taken, mainly in relation to the spine, which is usually injured when they are not observed. For example, the load on the spine must be vertically applied, avoiding bending over and keeping the load as close as possible to the body, symmetrical load and auxiliary means must also be used. Therefore, important considerations to keep the human body's integrity are necessary in order not to exceed the maximum load capacity.

4. Conclusions

This study may broaden the knowledge on ergonomics and its different conceptual and historical aspects, its objectives and types, and mainly the awareness as to the man-object system. Incorrect handling or excessive load transportation may cause several problems to the health of the worker and the simple user. Regarding these problems, mainly in relation to the worker who is subject to long work hours, it may be questioned whether there should be a responsible party for this worker's health and well-being, that is, whether preventing these problems is a duty of the employer, the own employee or the government.

Analyzing the harms that may be caused, it may also be considered that the most adequate solution is the prevention by observing the regulatory standards, in order to avoid the possible disturbances and misfortunes. It was shown that bad human postures are oftentimes adopted due to tools and packaging those are not adequately dimensioned.

The use of the project methodology, together with ergonomics and usability, is the basis to develop alternatives, tools and objects to assist the operator and the user when transporting and handling objects in a safer and more comfortable manner. A mistaken interpretation of the task may cause severe damages and even disabilities. Objects with no usability confuse the operator/user, inducing him/her to make a

mistake. In the work environment, in leisure areas or even within the household, such factors are called operational risks.

It is necessary to emphasize good postural practices and the correct use of equipment, instruments and objects in real situations that require active participation, in order to obtain satisfactory results: meet the goals of Ergonomics of maximizing the comfort and safety, minimize human costs and improve the quality and productivity at work. Therefore, further researches must be made to analyze the man-object relationship, as a parameter for the engineer and the designer to develop new packaging and tools/equipment, benefiting the workers and users, assisting them in the performance of their tasks, meeting their needs and minimizing mistakes.

Acknowledgment

The authors would like to thank the Laboratory of LabSIn (Integrated Systems) from the Faculty of Mechanical Engineering of UNICAMP, the financial support from CAPES and CNPq and Espaço da Escrita (Coordenadoria Geral da Universidade/UNICAMP) for the language services provided.

References

[1] W. Cybis, A.H. Betiol, R. Faust, Ergonomics and Usability: Knowledge, Methods and Applications, Novatec Editora, São Paulo, 2007.

[2] D.A. Norman, The Psychology of Everyday Things, Basic Books, New York, 1988.

[3] J.F. Gomes, Object Ergonomics, Escrituras, São Paulo 2003.

[4] Abergo—Brazilian Association of Ergonomics Home Page, http://www.abergo.org.br (accessed Jul. 2011).

[5] A. Wisner, Inside the Job—Ergonomics: Methods and Techniques, FTD S.A, São Paulo, 1987.

[6] E. Grandjean, Ergonomics Handbook, Bookman, Porto Alegre, 1998.

[7] What is Ergonomics, IEA (International Ergonomics Association), Madison, 2000.

[8] I. Iida, Ergonomics, Project and Production, Edgar Blücher, São Paulo, 2005.

[9] R.F. Abrahão, J.M. Tereso, Dciscipline “Ergonomics applied for engineering project” 2011, Feagri Unicamp.

[10] J.M.M. Neves, Study of usability with focus in PDAs, Master Thesis, UNICAMP (University of Campinas), 2005.

[11] NBR 9241-11: Usability Orientation, Brazilian Association of Technical Standards (ABNT), Rio de Janeiro, 2002.

[12] M. Hassenzahl, M. Burmestre, F. Koller, Usability engineering: Quality doesn’t happen by accident, in: Proceedings of the International Status Conference of the Lead Projects Human-Computer Interaction, Saarbrücken, Germany, 2001, pp. 99-103.

[13] A. Chapanis, The Engineering and Man-Machine System, Atlas, São Paulo, 1972.

[14] C. Negrão, E. de Camargo, Packaging Design: From Marketing to Production, Novatec Editora, São Paulo, 2008.

[15] D.S. Bolognini, Packaging, Art and Technique of a People, Toga, São Paulo, 1985.

[16] Law nº 366-A/97 Diary Republic, December 20th, 1997 http://dre.pt/pdf1s/1997/12/293A03/04980503.pdf (accessed Apr. 15, 2013).

[17] ABRE—Brazilian Association of Packaging Home Page, http://www.abre.org.br/setor/dados-de-mercado/texto.

[18] L.F. Silva, The Taste of Packaging, P&D UNICAMP, Brazil, Dec. 2000.

[19] M.A. Carvalho, Packaging Engineering: An Technic Approach the Development of Packaging Project, Novotec Editora, São Paulo, 2008.

[20] F. Mestriner, Packaging Design—Basic Course, 2nd ed., Pearson Makron Book, São Paulo, 2002.

[21] C.P. Neto, Definição de embalagem e seus tipos, http://www.administradores.com.br/informe-se/producao-academica/definicao-de-embalagens-e-seus-tipos/2170/ (accessed May 18, 2011).

[22] D.Z. Bucci, D.Z. Bucci, F.A. Forcellini, Sustainable packaging design model, Springer London, London, 2007, pp. 363-370.

[23] L.B. Guimarães, Sustainable brazilian design: The project process is hampered for lack of information, in: Proceedings of 6º ERGODESIGN, Bauru, SP, 2006.

[24] M. Asimow, Introduction to Design, Prentice-Hall, USA, 1962.

[25] R.A. Moura, J.M. Banzato, Packaging, Unitization & Containerization, Vol.II IMAM, 1997.

Journal of Mechanics Engineering and Automation 4 (2014) 488-498

Development of a Methodology for Determination and Analysis of Thermal Displacements of Machine Tools Using Finite Elements Method and Artificial Neural Network

Romualdo Figueiredo de Sousa, Fracisco Augusto Vieira da Silva, João Bosco Aquino Silva and José Carlos de Lima Júnior

Department of Mechanical Engineering, Federal University of Paraiba, João Pessoa 58051-900, Brazil

Received: March 28, 2014 / Accepted: April 14, 2014 / Published: June 25, 2014.

Abstract: In the processes of manufacturing, MT (machine tools) plays an important role in the manufacture of work pieces with complex and high dimensional and geometric accuracy. Much of the errors of a machine tool are those which are thermally induced which are from internal and external heat sources acting on the machine. In this paper, a methodology for determining and analyzing the thermal deformation of machine tools using FEM (finite element method) and ANN (artificial neural networks) is presented. After modeling the machine using FEM is defined the location of the heat sources, it is possible to obtain the temperature gradient and the corresponding thermal deformation at predetermined periods. Results obtained with simulations using the software NX.7.5 showed that this methodology is an effective tool in determining the thermal deformation of the machine, correlating the temperature reading at strategic points with volumetric deformation at the tool tip. Therefore, the thermal analysis of the errors in the pair tool part can be established. After training and validation process, the network will be able to make the prediction of thermal errors just stating the temperature values of specific points of each heat source , providing a way for compensation of thermally induced errors.

Key words: Thermal displacement, machine tool, finite element method, artificial neural network.

1. Introduction

The influence of temperature variation on MT (machine tools) is a physical phenomenon that cannot be completely eliminated. However, it should be monitored and included in the development process of the machine. Geometrical changes and/or structural volume of the machine represent the undesirable effects of heat and especially heat flow. These changes cause an unwanted relative motion between the tool and the work piece, which can negatively influence the specified tolerances during machining or accuracy [1]. Thus, this paper seeks to provide a contribution towards increasing the accuracy in MT, as compensation mechanisms are thoroughly studied to try to reduce thermal effects.

The main reason for the geometric and dimensional errors in production of work pieces in MF includes static laws of the rigid structure of the machines; the performance of the power law dynamics drives used and thermal deformations or displacements in the tool and the work piece [2].

In order to increase the accuracy of machined parts for machine tool CNC (computer numerical control) HSM (high-speed machining), by compensating the deformations caused by thermal variations during the process, which transforms the energy into thermal energy machining and propagates in the conduction, convection and radiation, the latter being discarded

Corresponding author: Romualdo Figueiredo de Sousa, Ph.D., research field: precision engineering. E-mail: engfsousa@bol.com.br.

and the concentration of studies usually done only by conduction and convection, or just taking into account the deformations arising under heat sources involved in the machine. Importantly, it is essential to develop methodologies which are able to analyze and evaluate the performance of high accuracy and high speed cutting of the MT, with regard to thermal effects.

In this paper, a methodology is established to decrease, even if it is simulated the effects thermals in MT, but that can later be used in real cases. Being used the tools of FEM (finite element method) and ANN (artificial neural networks), using the software NX and MatLab 7.5, respectively.

2. Machine Tool Analyzed

Considering the machine tool type column three axes, Fig. 1, the methodology that was employed for the analysis of thermal errors displayed on this machine, through the FEM and ANNs, has been adapted into a virtual machine to similar from Fig. 1, this simplified model of MF was redesigned, adapted in Ref. [3], the simulation software infinite element NX.7.5, simplified form whose considerations are discussed in following sections.

3. Methodology Used

Shortly after executing the design of the machine, setting the criteria for the creation of the finite element mesh, creating a mesh compatible with both the structural solution as thermal [4], then preceded with the following steps:

(1) Create a mapping file (file "bun" in the NX environment) which initially contains the values of temperatures for the conditions specified in the contours of a permanent state of temperature over a period of eight hours;

(2) Export the conditions of thermal contours for structural solution and then simulate the displacements occurring at the tool tip for the three axes of analysis. This operation being repeated 80 times for predetermined time interval of 8 h 28,800 s using a time increment between each simulation 360 s over the initial state at time zero, to complete the cycle;

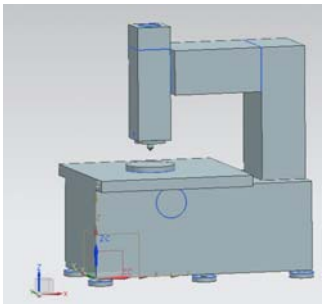

Fig. 1 Machining center type column redesigned in the NX environment (adapted in Ref. [3]).

(3) Collect the solutions for each increment of time considered and plot the data on the time x displacement, as well as temperature versus displacement in the MatLab environment;

(4) Create RNA through the environment MatLab function having, as input the temperature values of each node, represent the thermocouples on the machine tool, and as "target" or desired value for each respective displacements of the shaft. Training the ANN by means of programs developed in MatLab using the functions contained in this software;

(5) Run the validation process to verify that the Network could actually learn and predict the thermal displacements, only making use of the temperature readings on the specified nodes;

(6) Develop this method for two different cases, namely to a permanent state of temperature and temperature transient state;

(7) Simulate offsets in each axis, by means of the MATLab programs in two states analyzed to verify the efficiency of the technique developed.

4. Thermal Analysis of Shifts in Permanent State Temperature

In the machine tool of Fig. 1, it analyzed the thermal behavior and structural in order to find a relationship between the thermal volumetric displacements occurring at the tool tip, with tapered temperature reading strategic points on the machine. That is, the thermal behavior of the machine by

reading eight nodes symbolizes virtual thermo couples (T1, T2, T3, T4, T5, T6, T7 and T8.) as illustrated in Figs. 2 and 3. Near any heat sources, considering the amount of work, in the simulations, one eight-hour shift [4].

The thermocouples were distributed for the simulations as follows:

- T1: base part (Node 1,935);
- T2: mesa (Node 1,605);
- T3: base tool holder (Node 3,416);
- T4: upper bearing spindle (Node 3,146);
- T5: main engine (Node 2,455);
- T6: base table motor (Node 2,878);
- T7: coolant pump (Node 1,795);
- T8: oil pump (Node 2,564).

The considerations for analysis in this section are as follows:

- material machine-tool: steel density 7.829E-6 kg/mm^3;
- heat sources: some internal heat sources exist in machine tool variations in time;
- hazard analysis: 0 s to 28,800 s;
- thermal mapping performed for the times: every 360 s;
- temperature range: 20 °C-200 °C;
- structural boundary conditions: feet machine tool set;
- thermal boundary conditions: temperature set at each side of the machine tool in contact with the engine, with the bearing sand, the pair play tool, through a fixed temperature, as Figs. 4 and 5;
- element size: 50 mm;
- type of the element: tetrahedron with four nodes.

The conditions of thermal contours are shown in Figs. 4 and 5, where in the indications of temperatures from the heat sources in each internal face contact with the machine motors, bearings, etc., and the pair tool part, are illustrated. The reading of each thermo couple virtual over time, for the case considered in this section, is shown in the graph of Fig. 6.

It is observed mainly in the thermo couple located close to the tool as the temperature rapidly enters the steady state, and as others take longer, it happens

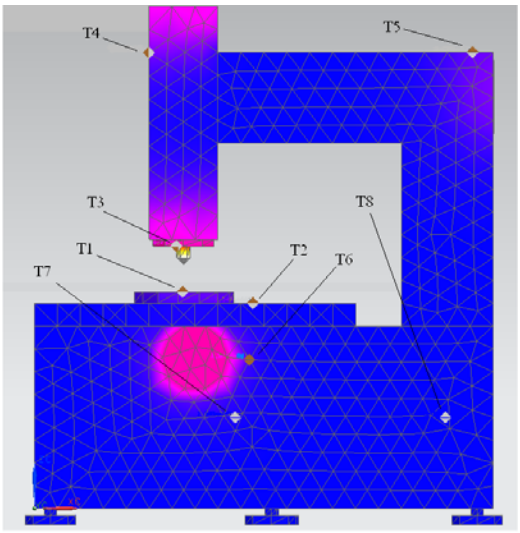

Fig. 2 Distribution of thermo couples in the structure of the virtual machine.

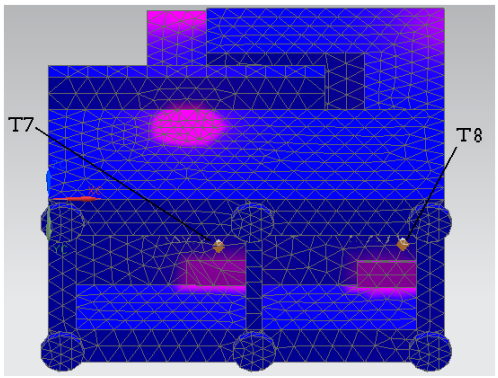

Fig. 3 Thermo couple virtual oil pump sander frigerant.

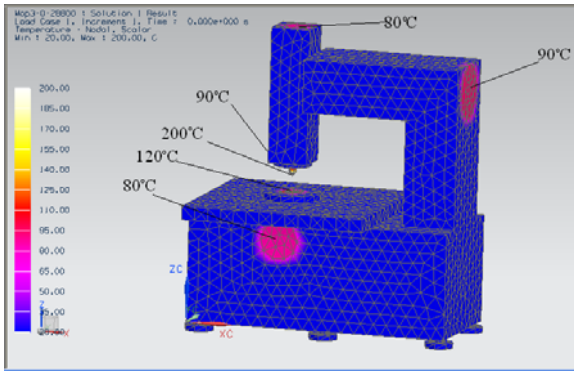

Fig. 4 Conditions of thermal contours.

mainly because of the heat generated at the tool end, assuming machining and proximity for each thermo couple.

When the simulations were performed, taking into

consideration a lathe eight hours of machining, the curves of the displacements thermal insulation in

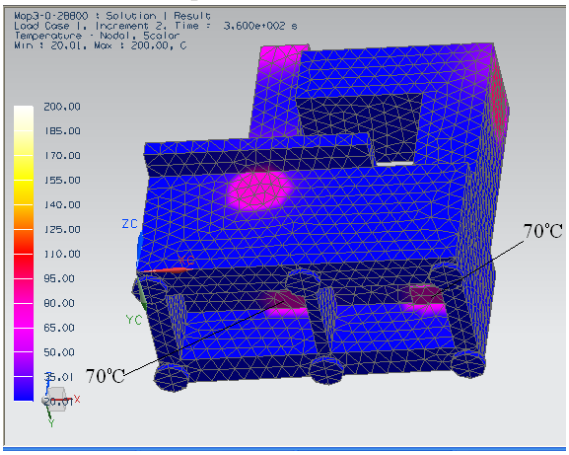

Fig. 5 Conditions of contours thermal oil pump sand cooling.

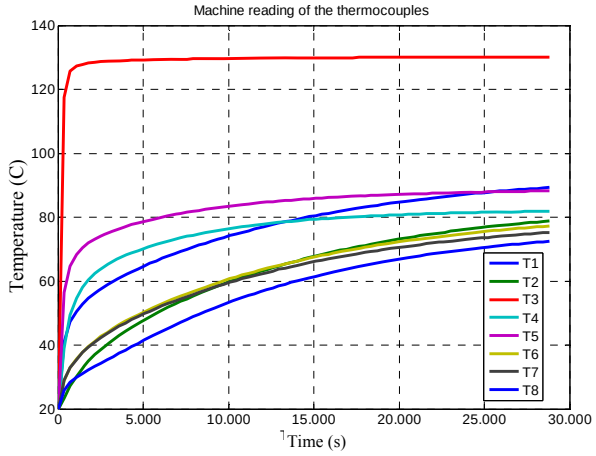

Fig. 6 Curves of the eight thermo couples in permanent state.

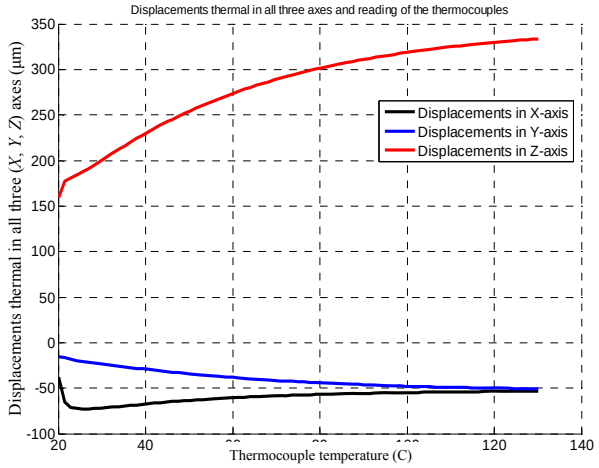

Fig. 7 Behavior of the three axes simultaneously-permanent state.

function of time respective axes are shown in Fig. 7, where if observe behavior smoother, due the fact of having been collected a sufficient number of points, as also the period analyzed time in the simulations is coherent with the performed in the machining process of an environment manufactures. If we still observes that, although the simulations commences in the zero instant, the displacements thermal on each axis already exhibit a significant error thermal, this happens due the fact that the temperature gradient be elevated in the permanent state temperature provoking great displacements thermal already in beginning of the process for this case.

5. Development of an RNA for Learning Axes Simultaneously on the Basis of the Readings of the Thermo Couples in the Steady State Temperature

ANN was formulated one of 16 neurons in the first layer and the second layer 1 neuron with feed-forward back propagation and feedback from output to input, with activation functions "tansig" and "purelin", respectively supervised learning by correcting errors standard mode [5], using Eqs. (1) and (2), whose topology is shown in Fig. 8.

$$tansig_j = \frac{2}{(1+\exp(-2w_i t_j))} - b_i \quad (1)$$

$$a_j = w_i t_j + b_i \quad (2)$$

where,

wi: the weight for each iteration *i*;

tj: mother mains input for each element *j*;

bi: bias or (threshold) of each neuron for *n* iterations.

It is created after the network, passed the learning process of the displacements of the three axes simultaneously, depending on the readings of the temperatures of the nodes that represent the thermo couples on the machine.

The entry "input" was introduced arrays temperature of each thermocouple, Eq. (3) over time and considered as "target" or desired output array of thermal displacement of the axes *X*, *Y* and *Z* Eq. (4).

$$T = \{[Tj]\} \quad (3)$$

$$A = \{[Dx][Dy][Dz]\} \quad (4)$$

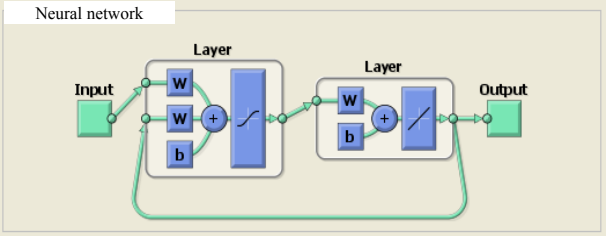

Fig. 8 ANN for three axis-permanent state.

where,

T = matrix of readings of all thermo couples in the analyzed period;

A = the matrix "target" or desired output of the thermal displacements in the period analyzed;

$[Tj] = \{Tj\ (1, i)\}$ matrix line of each thermo couple j for each increment i;

$[Dx] = \{Dx\ (1, i)\}$ matrix line of each matrix row in the X axis displacement for each increment i;

$[Dy] = \{Dy\ (1, i)\}$ matrix line every shift on the Y axis for each increment i;

$[Dz] = \{Dz\ (1, i)\}$ matrix line every shift on the Z axis for each increment i.

The result of the learning process to the three axes using the ANN carried in this section is shown in Fig. 9, which shows the learning simultaneously to the respective deflections along the three axes as a function of the temperatures developed in strategic points of the machine tool analyzed for 500 iterations.

It is seen in the same figure, convergence occurred for all axes. Five hundred iterations for the

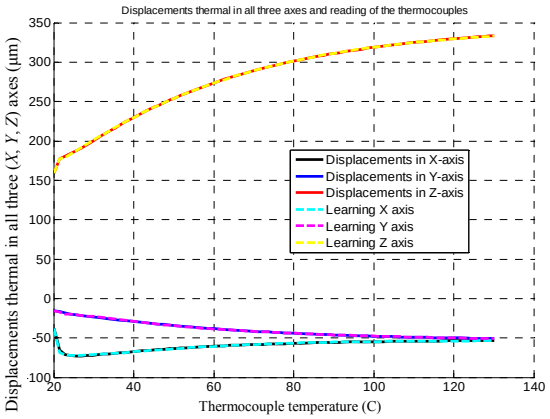

Fig. 9 Displacements as a function of volumetric temperature-permanent state.

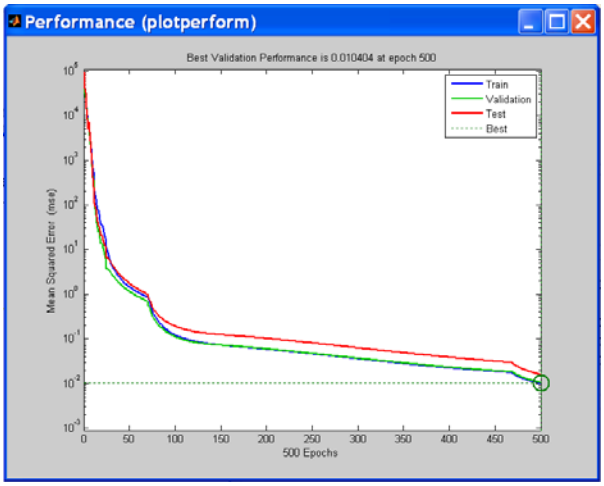

Fig. 10 Graph of the performance of ANN learning.

aforementioned performance curve, extracted from the environment MatLab is shown in Fig. 10, which is observed that the network could learn and that the error reached 0.01 µm compared to the simulated results.

6. Validation of ANN for the Three Axes in a Permanent State

Network after going through the process of learning, it is important to submit the network to another process called validation [6]. The validation process of an ANN is to provide the network after trained, different values of the input data which she was trained and then compare them with the simulated results of these new input data, to verify that the network could actually learn satisfactorily, and whether it is possible to predict the deformations, providing only the values of the temperatures measured by the thermocouples. For the validation processes steady state temperature. The procedure was as follows:

Again we performed simulations, being the time interval for each reading 180 s. Of the 162 new temperature readings of the thermo couples, disregarding that coincided with the previous analysis.

Next to the new temperature readings of the eight thermocouples, fed to the network only at the new readings without the network retrained.

After performing the above procedure, we obtained

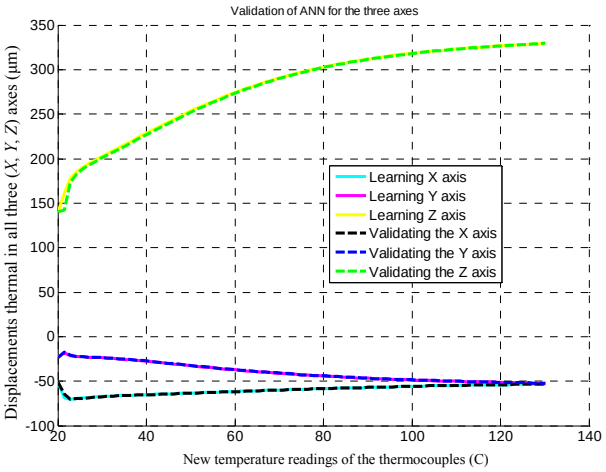

Fig. 11 Validation of ANN for the three axes, heat sources contained.

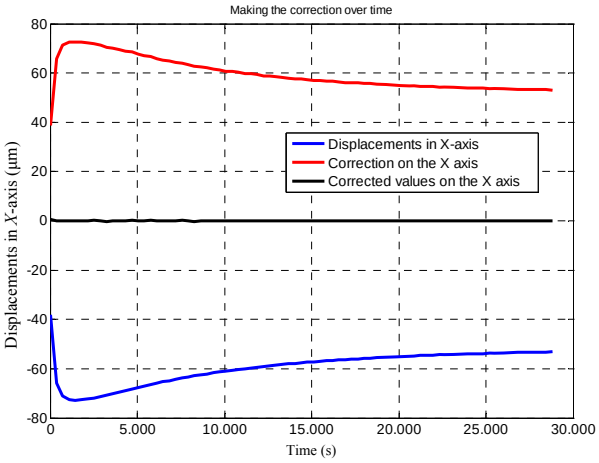

Fig. 12 Corrections in the *X* axis along time.

the validation curves as shown in Fig. 11. Thus, ANN, made the prediction of deformations, even entering different values (of temperature) of those she was trained. Being able to reach the goal of validation and keep this section to the permanent state of temperature.

7. Analysis of Results and Compensations for the Steady State Temperature

Using the curve that the ANN learned the thermal behavior of the *X* axis to predict the thermal deformation of this axis machine tool analyzed, and make possible corrections or compensations. In Fig. 12, the black curve of displacements corrected or compensated. Where one can observe that with the correct coordinate axis *X*, using the technique proposed virtually zero thermal error on this axis.

Using the same technique for the *Y* and *Z* axis, there is the efficiency of the method.

8. Thermal Analysis of Shifts in Transient State Temperature

In this section, the same procedure will be adopted in the previous section, in other words, the same configuration of the machine tool, the thermocouples located on the same nodes, and the same conditions of structural contours, but just changing the conditions of thermal contours, which will be replaced by heating equations for each heat source.

The considerations for the simulation results in this section are the same as in the previous section, but only change the transient thermal boundary conditions, in other words, temperature set at each side of the machine tool in contact with the engine, with the bearing sand the pair play tool, by heating the equation of Newton, Eq. (5). The graph of Fig. 13 was plotted from the law of heating/cooling Newton, according to Eq. (5) each heat source. As seen in its initial temperature (Tm) which coincides with the temperature at 20 °C, if the instant "0 s" and a final temperature $T_{(\infty)}$, which is the maximum power that can reach through the simulation conditions preset to a final state of thermal equilibrium.

$$\frac{dT}{dt} = k(T - Tm) \quad (5)$$

where,

Tm = room temperature;

T = temperature of the body at time t;

K = proportionality constant.

Solving Eq. (5), by separation of variable sand replacement of boundary conditions, according to Ref. [7] is Eq. (6):

$$Tl(t_i) = T_{(\infty)} + C_j \times \exp(-k_j \times t_i) \quad (6)$$

where,

$Tl(t_i)$ is the local temperature of each heat source at

time t_i;

$T_{(\infty)}$ is the steady state temperature;

C_j constant is found from the condition of initial and final contours;

K_J is time constant found for each heat source in unit time (s).

It represents the time that the source spends to reach 63.2% of the final value of the temperature rise corresponding to its operation in a state of thermal equilibrium or steady state [8]. And t_i is the time to consider every moment according to the temperature transient.

The value of the time constant for all sources, were found from the initial boundary condition $T(0)$ = 20 °C and intermediate condition $T(1{,}800)$ = $0.632 \cdot T_{(\infty)}$.That is the temperature at time 0 sand the temperature at which the source can reach the elapsed time when 1,800 s or 30 min.

As showing, only two are assigned numerically as an example, the eight equations as conditions found in simulations contours of heat sources close to the thermocouples installed in the structure, as seen in Figs. 4 and 5, the two equations are the following:

Temperature in the base part (close to $T1$) via the associated Eq. (7):

$$Tb(t_i) = 120 - 100 \times \exp(-0.000450 \times t_i) \quad (7)$$

Temperature in the tool holder (next to the tool, T3), linked by Eq. (8):

$$Tf(t_i) = 200 - 180 \times \exp(-0.000493 \times t_i) \quad (8)$$

From the graph of Fig. 13, it is shown at eight curves from data collection of virtual thermocouples throughout the simulation period considered and the thermal displacement on the Y axis. It is observed eight different curves relating to data collected from each heat source, whether transients exist three equations equal, this happens because the position or location of each thermocouple being different in the structure of the machine. What is more coherent because all heat sources begin at 20 °C which is exactly considered the initial temperature of the entire structure of the machine and the thermal shifts starting 0. Although the graph of Fig. 13 shows only the displacements in the Y axis can also be achieved for the other axes respectively at the end of the tool achieved by the FEM analysis.

There has been an irregular deformation in the first 1,800 s (Fig. 13), although the heat sources have a rather regular behavior. Such irregularities are usually due to temperature gradients which are greater at the beginning of machining machine tool of any or due to other structural parameters which provide voltages at certain points in the machine frame. It was also observed that the initial deformation on the X axis is zero for the initial time, the initial temperature of 20 °C. In other words, it is more consistent with the reality machining than in the situation considered in the section where the heat source had a temperature constant, in other words, steady, besides the fact of observing the deformation at the tool tip on the X axis, and the temperature of each heat source with the reading of the respective thermocouples on the same graph.

The fact show deformations in the negative Y axis is due (Fig. 13), the tool tip to deform in the direction opposite the direction of the axis of the machine and no shrink age or the influence of other axes, as well as heat sources.

The deformations also occur in the other two axes,

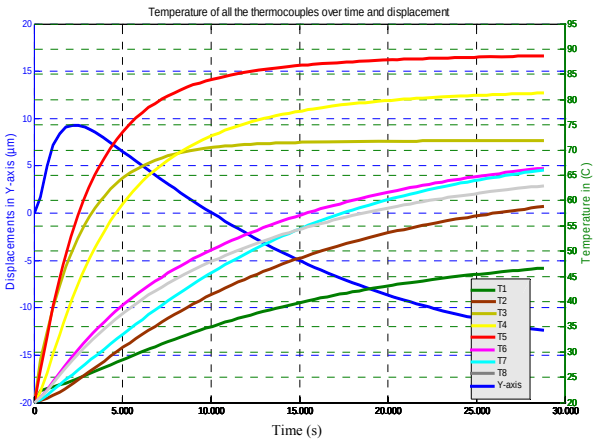

Fig. 13 Reading of the thermocouple sand displacement in the *Y* axis over time.

having different behavior due to the fact that they

have different stiffness and thermal diffusivity on each axis, as well as the extent of deformation over time considered. In this paper, it is shown only one axis due to synthesis of the work, but he analysis maybe performed either individually for each axis or in a volumetric showing the thermal behavior of all the axes simultaneously, because the methodology allows.

9. ANN Learning for State Transient Temperature

For learning the volumetric deformations, that is, the thermal deformation occurring simultaneously in each axis, whereas the same machine fermentation heat source sand variations in time (transient event). It was formulated an ANN with the same characteristics of the section steady state temperature, only changing the values of the input array and the "target", using the same topology of the previous case for the three axes, but with data from transient state temperature. In Fig. 14, it has been learning for artificial neural network for 170 iterations, as shown:

It can be seen from the graphs that the network successfully learned the thermal volumetric machine for the transient event, through the convergence curves, that is, the thermal displacement on each axis happens simultaneously. But that is not enough; the network has to go through the validation process.

In Table 1, there is an example of learning of ANN for the 10 initial training data network, having as input the temperatures of the thermocouples, and one of the "target" thermal displacement of the tool tip is relative to the *Z* axis, with their errors of learning in relation to the displacement occurred on the same axis, collected as example after 239 iterations, a maximum of 500 iterations.

In Table 1 below, again as the network converged, or learned by reducing the error.

You can clearly see this statement, besides the graphs shown in Fig. 14. Or by means of the graph of Fig. 15, which shows the behavior of the mean square error relative to the axis *Y*. Dropping to less than 0.1 μm approximately one hour when it was simulated machining.

10. Validation of ANN for the Three Axes in the Transient State

In the process of validation of the ANN

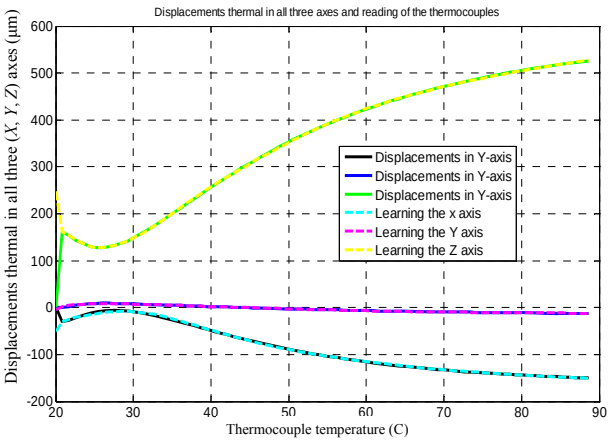

Fig. 14 Learning the neural network model for 170 iterations.

Table 1 Sample learning of ANN for the *Z* axis.

Some thermocouples temperature (°C) RNA input				Thermal displacement in *Z*-axis (μm)	Learning RNA (μm)	Error (μm)
T1	T2	T3	T4			
20.0	20.0	20.0	20.0	0.0	239.72	-239.7
21.9	20.2	25.5	20.8	161.4	161.06	0.34
22.4	20.4	28.5	22.1	154.1	155.84	-1.74
22.8	20.8	34.0	25.7	144.8	149.09	-4.29
23.1	21.4	38.8	29.6	137.2	139.81	-2.61
23.5	22.1	43.1	33.4	131.8	132.53	-0.73
23.9	22.8	46.8	37.1	128.8	128.57	0.23
24.3	23.7	50.0	40.5	128.1	127.81	0.29
24.8	24.6	52.9	43.7	129.5	129.45	0.05
25.3	25.5	55.3	46.6	132.7	132.68	0.02

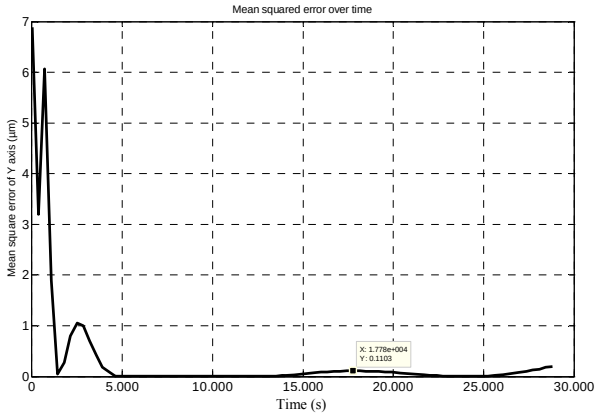

Fig. 15 Mean square error for the *Y*-axis transient state.

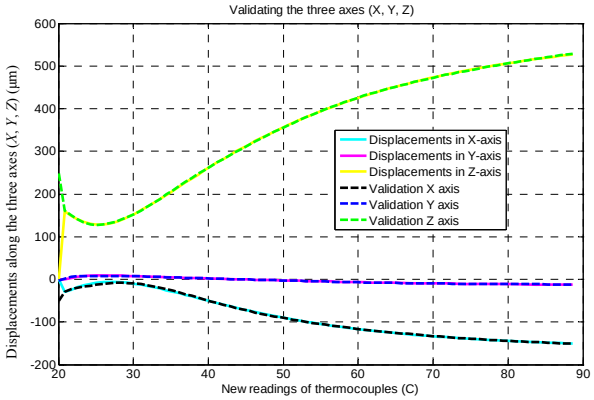

Fig. 16 Validation of ANN-case transient.

To the transient event, the procedure was the same as the section to steady state temperature, or consist of the supply network after trained different values of input data with which it was trained, to verify that the network actually managed to learn the thermal behavior satisfactorily, and make the prediction of thermal displacements of the tool, only with the entry of the temperature readings of the thermocouples transiently.

For these simulations validation process proceeded as follows:

Executed the simulations again, being in a time interval for each reading 180 s. 162 of the new temperature, readings of the thermocouples, disregarding that coincided with the increase of time of 360 s.

Then with the new temperature readings of the eight thermocouples, fed into the network only at the new readings without the network to be retrained, in other words without a "target". Curves were obtained for validation as shown in Fig. 16. In other words, ANN made the prediction of deformations, even entering different values (temperature) of those she was trained also to transient state. It is observed that there is little discrepancy between the curve simulated deformation and validation for each axis only at the start of the curves where the network begins the process of learning and the temperature gradient is increased, there is a greater difference between the curve sand values. Soon the validation process was satisfactory.

11. Corrections to the Transient Case

Using the curve that the ANN learned, considered as an example in this section, only the thermal behavior in the *X* axis, to predict the thermal deformation of this axis machine tool analyzed, and make possible corrections. Is the corrected strain curve of the *X*-axis in Fig. 17? Where one can observe that with the correct coordinate axis *X*, using the technique proposed, virtually zero thermal error on this axis, immediately when the machine starts the heating process? The same procedure for corrections or offsets *Y* and *Z* axes can be performed.

Performing the corrections in the *X*-axis, *Y* and *Z* to become volumetric error is, as shown in Fig. 18, almost constant after 25.09 °C, and less significant than in the situation without correction. In percentage terms, we consider the last time increment, where the thermal displacements were increased to 150.75 µm and 0.65 µm (reduction of 99.57% in the *X*-axis), 11.83 µm to 0.56 µm (reduction 95.1% on the *Y*-axis), and 528.38 µm to 1.98 µm (reduction of 99.62% in the *Z*-axis).

In other words, the joint work of the FEM, ANN and methodology developed in this work provide significant results in the case of correction of thermal errors in machine tools even in a simulated. But the methodology can be used in real cases of compensation thermal errors even in the most critical case is that the transient case.

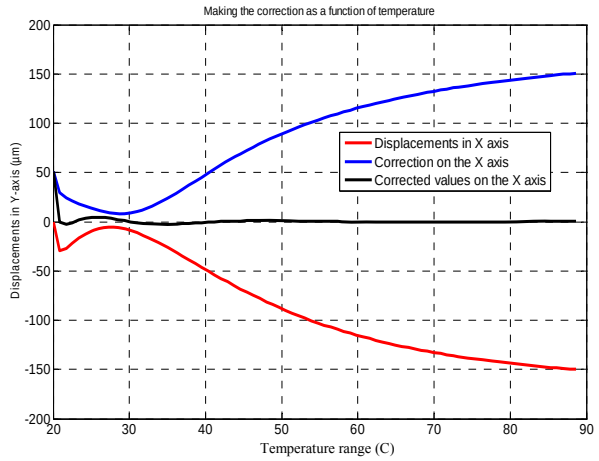

Fig. 17 Correction of the *X* axis, if transient.

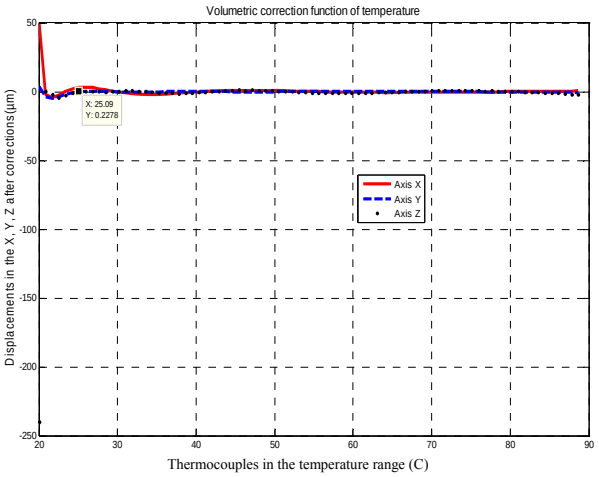

Fig. 18 Volumetric Correction for axis.

12. Conclusions

The data collected from the thermal deformation of machine tool model analysis, can also be collected in any model of machine tool, since it applies the same methodology or that already has the design of the machine using the technology and export to CAD software working with the FEM and then develop ANNs.

The thermal behavior of the machine is very different from that, which was used at a constant temperature from start to finish the simulations, but it is closer to the reality of a machining process, it is therefore more reliable and can show that thermal errors consistent with the reality of machine design. The fact that there are more irregular thermal errors in the first 30 min proves the two thermal conditions studied contour, what is said in the literature, in other words, the machine tool studied is consistent with a real model, considering only the conditions studied. It is observed that in both cases the heat source is variable or it is not the network has difficulty in learning at the beginning of the deformation. What one can optimize this by refining the network and increasing the number of data in the beginning of deformations is increased or the number of points collected between 0s and 360 s. It is also observed that, although the heat sources variations in time, that is, the temperature rise is smoother, has more considerable deformations mainly in the *Y* and *Z* axes in relation to the heat sources constant. Due to the fact that the temperature gradient is due to greater thermal stability and it is slower. Regarding the neural networks, the temperature, the coordinates of each point analyzed and the thermal displacements corresponding to each axis of MF derived from the thermal expansion are the input and output of the artificial neural network, respectively. That through these data, the network topology suggested, "learned" significantly offsets in each axis simultaneously are able to predict the movement only with the entry of the matrix temperature, as verified in the validation section of ANN. Therefore, this work contributes significantly, through the methodology suggested for the reduction and/or reduction of thermal displacement in machine tool.

References

[1] J. Vyroubal, Compensation of machine tool thermal deformation in spindle axis direction based on decomposition method, Precision Engineering 36 (2012) 121-127.

[2] M. Week, P. Mckeown, R. Bonse, U. Herbst, Reduction and compensation of thermal errors in machine tools, Annals of the CIRP 44 (2) (1995) 589-598.

[3] H.J. Pahk, Y.S. Kimt, J.H. Moon. A new technique for volumetric error assessment of CNC machine tools incorporating ball bar measurement and 3d volumetric error model, Int. J. Mach. Tools Manufact 37 (11) (1997) 1583-1596.

[4] R.F. Sousa, Development of a methodology for determination and analysis of thermal displacements of machine tools using finite elements method and artificial neural network, Ph.D. Thesis, Federal University of Paraíba, 2013.

[5] J.H.F. Cavalcante, Artificial Neural Network, Federal University of Paraíba, April, 2004.

[6] J.C.L. Júnior, Application of artificial neural networks to determine parameters of substitute geometries in MMCs, Ph.D. Thesis, Federal University of Paraíba, 2007.

[7] R. Bronson, C. Gabriel, Differentiable Equations, 3rd ed., SCHAUM, São Paulo, 2008.

[8] F.P. Incropera, D.P. Dewitt, T.L. Bergman, A.S. Lavine, Fundamentals of Heat and Mass Transfer, LTC, Rio de Janeiro, 2008.

Journal of Mechanics Engineering and Automation 4 (2014) 499-504

Temperature Control of a Thermal Plasma Torch with Inductive Coupling Using the Arduino Board

Gustavo Fernandes de Lima, Glauco George Cipriano Maniçoba and Andrés Ortiz Salazar

Department of Computer Engineering and Automation, Federal University of Rio Grande do Norte, Natal 59072-970, Brasil

Received: February 17, 2014 / Accepted: March 11, 2014 / Published: June 25, 2014.

Abstract: Plasma torch is a device that transforms electrical energy into heat carried by a gas and its safe operation is necessary to control her temperature. This paper presents the use of the Arduino board in temperature control of a plasma torch through fuzzy control. The plasma torch of this project was built so that a flow of water can circulate through your body, allowing its cooling. The cooling system mounted consists of one radiator, one expansion vase, one water pump and one temperature sensor. The heated water coming the plasma torch is passed by the temperature sensor. This is converted in a voltage and read by an analog input port of the Arduino. This processes the information received and makes the decision to turn on/off the radiator fan and/or powered the frequency inverter water pump to control the temperature. The graph of the fuzzy control showed an oscillation between 104 °F to 122 °F around the chosen reference 113 °F. The results show that it is possible to control the temperature of a plasma torch using the Arduino board and fuzzy logic.

Key words: Arduino, torch, fuzzy logic, temperature, thermal plasma.

1. Introduction

Arduino is a prototyping platform electronics open source based on flexible hardware and software and easy to use. It is destined for artists, designers, hobbyists and anyone interested to create interactive objects or environments [1].

The Arduino board can integrate with environment by receiving signals inputs from types varied of sensors. And it can also affect the environment by controlling lights, motors or others actuators.

In this work, the environment of Arduino interaction was a water refrigeration system for a thermal plasma torch. The Arduino board received an electrical signal from temperature sensor and acted by controlling a frequency inverter which powered a water pump, and acted in a fan coupled a radiator.

The form how refrigeration system was projected enabled the implementation of a controller using fuzzy logic embedded on Arduino board, which controlled on spin speed of water pump and on/off fan of radiator.

The paper is organized as follows: Section 2 presents the theoretical foundation; Section 3 presents the a short description of components using in this work; Section 4 shows the results and discussion; and Section 5 presents the conclusions.

Corresponding author: Gustavo Fernandes de Lima, electrical engineer, specialist, research fields: analog electronics, control systems and automation. E-mail: gustavoflima@msn.com.

2. Theoretical Foundation

2.1 Fuzzy Logic

In 1965, the professor Lofit A. Zadeh from Berkeley's University proposed a new theory of sets, where transition of pertinence to non pertinence were slow and progressive, and no abrupt how in usual theory of sets [2]. Thus, it emerged the Fuzzy Set theory.

A system based in fuzzy logic can have your action schematized by the elements [3]: fuzzificator, rule base (knowledge base), inference engine (decision-making unit) and defuzzificator. This structure can be viewed in Fig. 1.

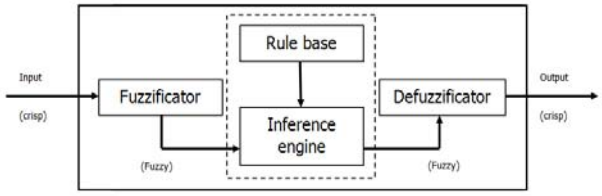

Fig. 1 Blocks of the controller fuzzy.

The fuzzificator has for function to convert the numeric values of the inputs in linguistic variables.

The rule base represents a system model to be controlled, consisting of a data base and a linguistic fuzzy rule base.

The inference engine has for feature to transform input linguistics values, with the rules, on output linguistics values.

The defuzzificator has for function to translate the output linguistic values on output numeric values, usable in a control action at real world.

2.2 The Arduino Board

The Arduino is a board of printed circuit (2.68 × 2.17 × 0.39), indicated for creation electronics prototypes based on the philosophy of open hardware and software. It has a 01 microcontroller ATmega328P (manufactured for Atmel Company), 14 digital inputs/outputs, 06 analog inputs and pins of 3.3 Volts, 5.0 Volts and Ground (Fig. 2).

In this work, the Arduino Uno model was chosen for those reasons: it has USB connection, one jack connector for supply external, simple programming, low price and easy manipulation.

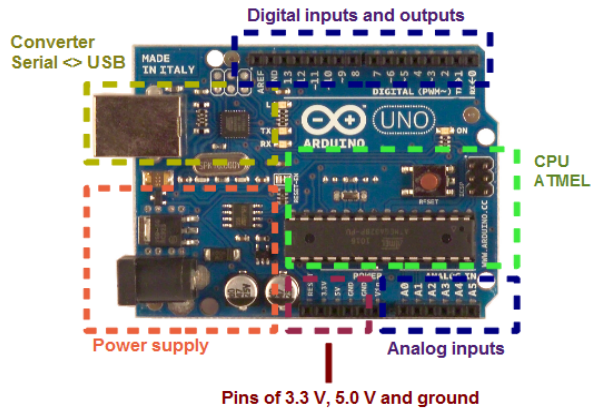

Fig. 2 Identified blocks of the Arduino Uno.

Also, two modules were used in connection with the Arduino board. The first module was SD card (Fig. 3a) and the second was LCD (liquid-crystal display) 16 × 2 (Fig. 3b).

In this project, the SD card module was used for save the measurements of temperature and time in txt. file. Whereas the LCD module was used to show the values of temperature and time measured.

2.3 Temperature Sensor NTC (Negative Temperature Coefficient)

In this project, one thermistor NTC, low cost semiconductor which decreases the electrical resistance with increment the temperature were used (Fig. 4).

The NTC sensor works for a resistance of 520 Ω in 298.15 K (77 ºF) and 75.41 Ω in 373.15 K (212 ºF), with a tolerance of 1% to 5%, giving a non-linear graphic. For making one, this curve graphic was used in Eq. (1).

$$R = R_0 \cdot \exp\left[\beta \cdot \left(\frac{1}{T} - \frac{1}{T_0}\right)\right] \quad (1)$$

where, R is the thermistor resistance at temperature T, R_0 is a thermistor resistance at temperature T_0 and β is the material constant which is equal to 2,864.30 [4].

Fig. 5 presents the characteristic curve of the sensor used in this project.

(a) SD Card (b) LCD

Fig. 3 Modules for connection with Arduino board.

Fig. 4 NTC sensor used in this project.

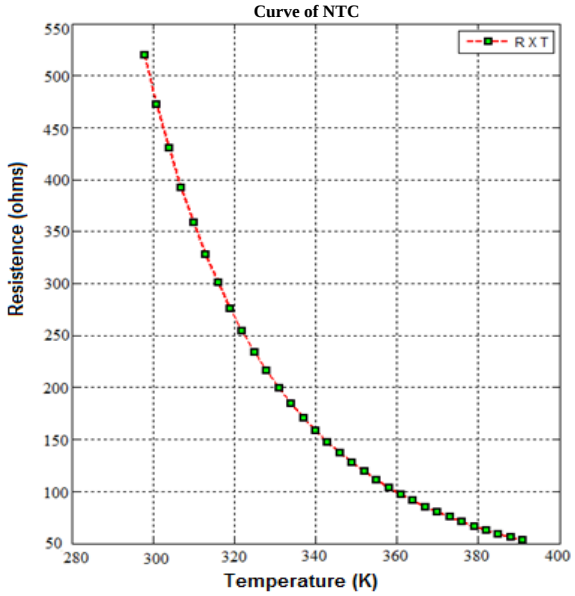

Fig. 5 Characteristic curve of the sensor NTC.

The Arduino analog input was developed to receive voltage up to 5 V_{DC}. Therefore, it raised the need to conversion the NTC's resistance in matching voltage signal.

A voltage divider circuit was chosen to convert the resistance of NTC in measurable voltage by Arduino. In the configuration chosen, an increase of temperature was reflected in increase of voltage V_0 (Eq. (2)).

$$V_0 = V_{cc} \cdot \left(\frac{R_1}{R_1 + R_{NTC}} \right) \quad (2)$$

The V_0 voltage was connected in analog input A0 of Arduino board and this one has to calculate the resistance R_{NTC} (Eq. (3)).

$$R_{NTC} = \left(R_1 \cdot \frac{V_{cc}}{V_0} \right) - R_1 \quad (3)$$

For determine of the current temperature of system in Kelvin, was used the Steinhart-Hart's equation (Eq. (4)).

$$T(K) = \frac{1}{a + b \cdot \ln(R_{NTC}) + c \cdot (\ln(R_{NTC}))^3} \quad (4)$$

The Steinhart-Hart's coefficients (a, b, c) were extracted from Ref. [5], whose values were:

$$\begin{bmatrix} a \\ b \\ c \end{bmatrix} = \begin{bmatrix} 0.0012 \\ 0.00033151 \\ 0.0000001962 \end{bmatrix} \quad (5)$$

In this moment, it was possible to implement the stretch of source code for Arduino able to convert the read voltage in A0 input, calculate the resistance R_{NTC}, determinate the temperature in Kelvin and, lastly, convert for a temperature in ºF, according to Code 1.

```
//Convertion sensor voltage in temperature
Tensao Sensor = analog Read(A0); //read input A0
V0 =Tensao Sensor * 5/1023; // convert to voltage
Rntc = (5*150/V0)-150; //RNTC = (Vcc*R1/Vin)-R1
b1 = log(Rntc); //calculate LN(RNTC)
b1 = 0.00033151*b1; //calculate b*LN(RNTC)
c1= log(Rntc); //calculate LN(RNTC)
c1 = 0.0000001962*c1*c1*c1; //c*(LN(RNTC)^3)
tempK=0.0012+b1+c1; //a+b*LN(RNTC)+c*(LN(RNTC)^3)
tempK = 1/tempK; // 1/(a+b*LN(RNTC)+c*(LN(RNTC)^3))
tempC =tempK-273.15; //convert to ºC
tempF = tempC*1.8+32; //convert to ºF
```

Code 1 Stretch of Code for Arduino.

2.4 Plasma Torch

The plasma can be defined how a gas partly ionized where exist free electrons and positive ions in movement, in the process where happen transference of energy by radiation, conduction and Joule heating between others [6].

Now, the plasma torch for Ref. [7] is a dispositive which transforms electrical energy in heat transported by a gas. With these devices, virtually either one gas can lead the plasma state.

For this project, one ICP (inductive coupled plasma) torch was chosen. According to Ref. [5], an ICP torch has by advantages do not have internal electrodes metallic, to be eroded by plasma jet, avoiding possible contamination. Fig. 6 presents one image of the ICP torch used in this project.

This torch was built to allow the water flow in two different paths, for your own cooling. Still in Fig. 6, it is possible to see an indicative numeration for these paths. In the first path, the water gets in the exhaustion opening (nº 1), goes to tube of confinement and gets

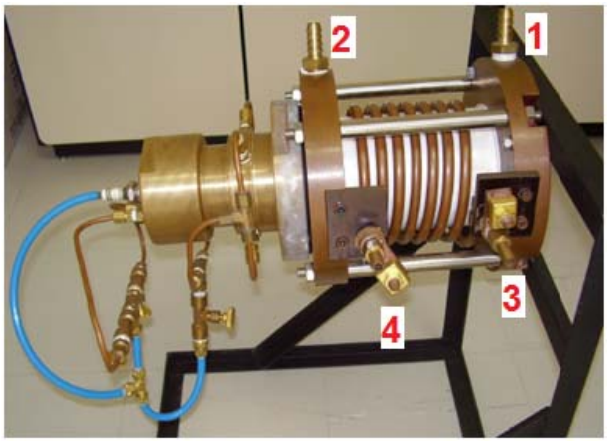

Fig. 6 ICP torch of the project.

out by the base of torch (nº 2). The second path enters in the nº 3 and gets out in the nº 4 by within of coil.

3. Description of Components

3.1 Water Refrigeration System

One water refrigeration system was mounted compound by one radiator (heat exchanger), which have one fan coupled and powered by three-phase motor, one expansion vase, one water pump powered by one frequency inverter and one NTC temperature sensor, according to Fig. 7.

These components have the following features in the cooling system [8]:

- Radiator: device used to exchange heat between the heated water from the plasma torch and the atmospheric air;
- Expansion vase: semitransparent plastic reservoir which allows to see the water level;
- Water pump: responsible for circulating water in the cooling system of the plasma torch;
- Temperature sensor: responsible for the measurements of water temperature in the cooling system of the torch.

3.2 Description of Control

The control of temperature proposal can be visualized in block diagram of Fig. 8.

In this diagram, the water temperature of system was read by Arduino. For determining the error (ε) value,

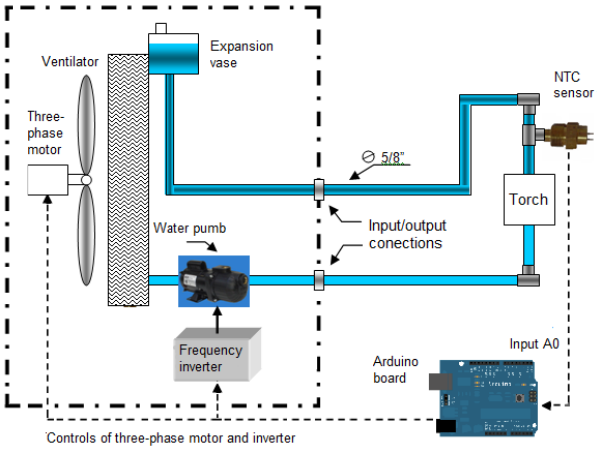

Fig. 7 Refrigeration system of the torch.

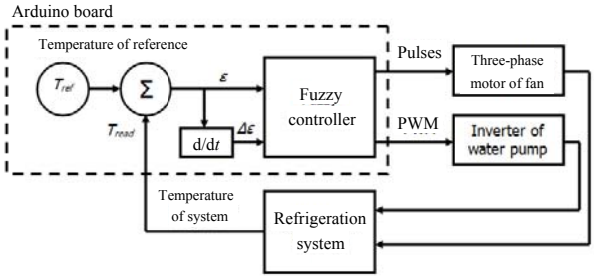

Fig. 8 Block diagram of the system.

Eq. (6) was used. This is the first variable of fuzzy controller and measurable in Celsius degree.

$$\varepsilon(°\mathrm{F}) = T_{\mathrm{read}} - T_{\mathrm{ref}} \qquad (6)$$

After that, the error value (current) was subtracted of the previous error value for determining the "variation of error" ($\Delta\varepsilon$) value, according to Eq. (7). This is the second variable of fuzzy controller and measurable in ºC/min.

$$\Delta\varepsilon(°\mathrm{F/min}) = \frac{\varepsilon_{\mathrm{current}} - \varepsilon_{\mathrm{previous}}}{\mathrm{d}t} \qquad (7)$$

With two previous values, the fuzzy controller combined variables ε and $\Delta\varepsilon$ in the inference rules, of type if then, and created two appropriates outputs. The first for powered the of frequency inverter and second for powered of the radiator's fan.

3.3 Fuzzy Controller

The fuzzy logical toolbox of MATLAB™ software was used for created the inputs variables of fuzzy system and determine output variables values.

The ε variable was defined with values in -67 ºF to

131 ºF and Fig. 9 shows the fuzzy set created, where linguistics values were: L (low), M (medium), SP (set point), H (high) and VH (very high).

The "variation of error" variable was defined with values in 22.1 ºF/min to 41.9 ºF/min and Fig. 10 shows the fuzzy set created, where linguistics values were: FF (falling fast), FS (falling slow), S (stable), RS (rising slow) and RF (rising fast).

The first output variable was called PWM (pulse width modulation) and represented the signal of powered of the frequency inverter (0 to 100%) of water pump and Fig. 11 shows the fuzzy set created, where linguistics values were: S (small), M (medium), B (big) and VB (very big).

The second output variable was called pulses and represented the on/off signal of radiator's fan and Fig. 12 shows the fuzzy set created, where linguistics values were: off and on.

For inference machine, the Mandani was used and the defuzzification was calculated using the medium of the maxima pertinence.

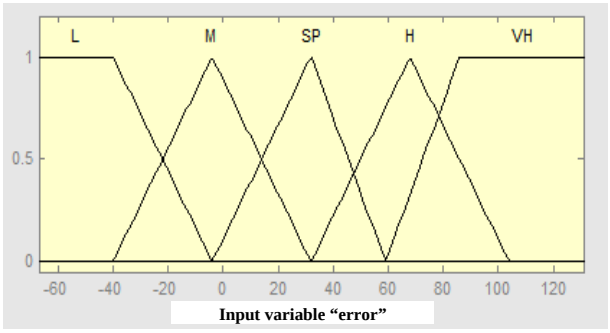

Fig. 9 Pertinences of the "error" variable.

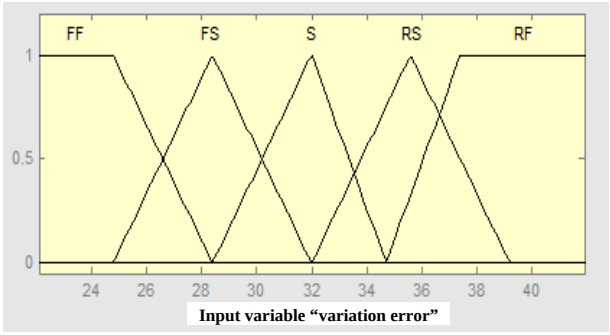

Fig. 10 Pertinences of the "variation of error" variable.

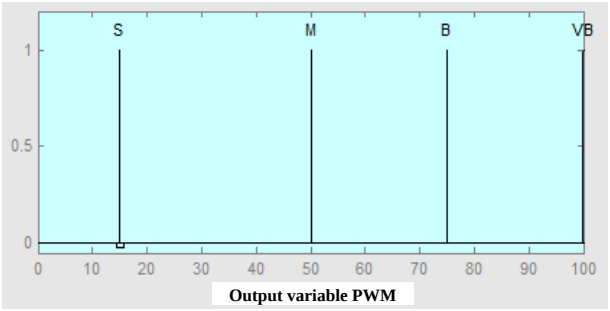

Fig. 11 Pertinences of the PWM variable.

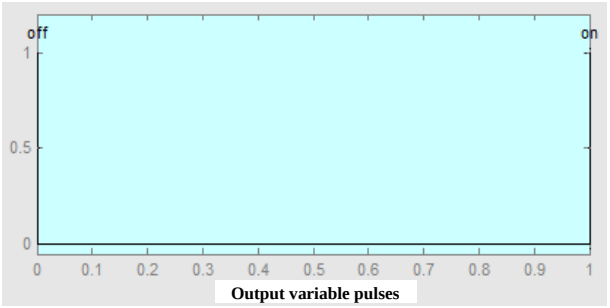

Fig. 12 Pertinences of the pulses variable.

4. Results and Discussion

For the demonstration of the control operation, five real experiments were made. In all, the reference temperature was configured in 113 ºF, for security reasons. The radiator's fan temperature powered was configured in 122 ºF and after was turned off when the temperature achieved 104 ºF.

The fuzzy controller was configured for keeping the PWM variable in a constant value. In the first experiment, that value was 15% (green curve), in second 50% (yellow curve), in third 75% (red curve) and in fourth 100% (black curve). In the last experiment, the fuzzy controller was configured for any PWM variable value, in range from 0 to 100% (blue curve).

Fig. 13 shows all curves of the five real experiments. This allowed to see the temperature behavior when the PWM variable was remained constant and when her changed freely. In all, the fuzzy controller worked how expected and allowed the temperature variation was within of the range previous determined from 104 ºF to 122 ºF.

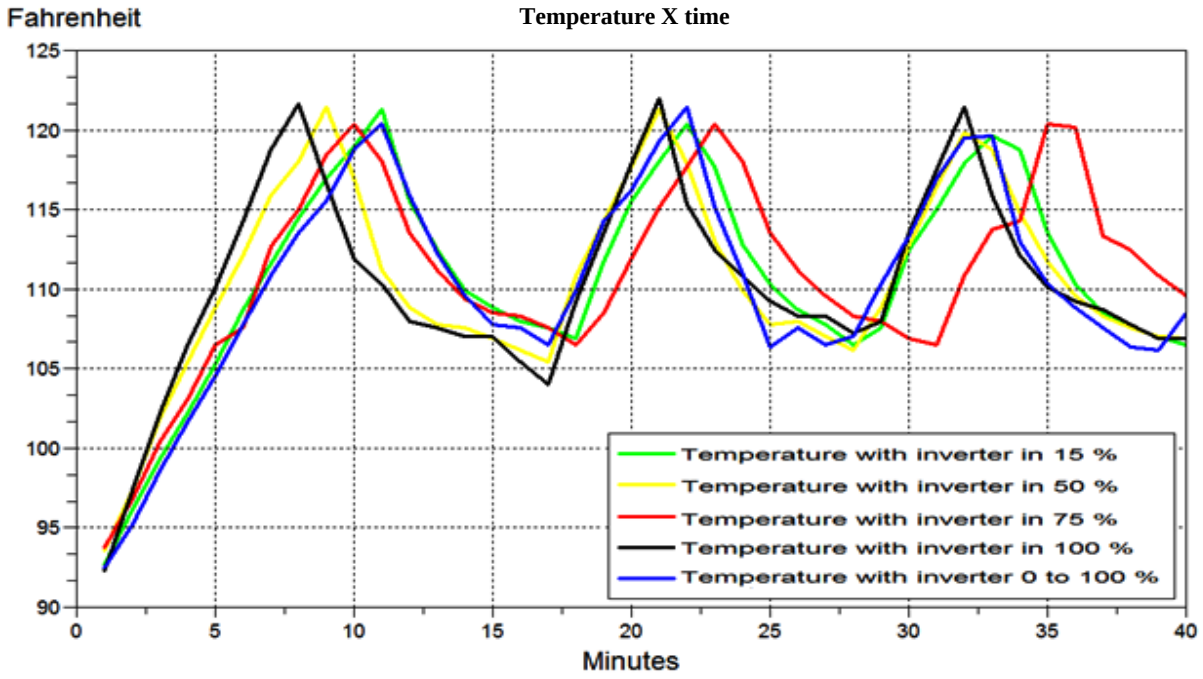

Fig. 13 Variation of the water temperature.

5. Conclusions

In this work, it presents the use of Arduino board in temperature control of water which cools a thermal plasma torch used the fuzzy control. The objective was achieved, once the temperature of water ranged between 106.16 ºF and 121.46 ºF within the range from 104 ºF to 122 ºF as previous defined. This result was possible why the temperature is a magnitude slow varies, which allowed for Arduino board works without big computational endeavor.

References

[1] Arduino Home Page, http://www.arduino.cc (accessed 2013).

[2] M. Bilobrovec, R.F.M. Marçal, J.L. Kovaleski, Implementation of an intelligent control system using fuzzy logic, in: XI SIMPEP, Bauru, SP, 2004.

[3] F.M.L. Filho, H.L. Gosmann, A. Bauchspiess, Fuzzy control for liquid level system, in: XIV Congresso Brasileiro de Automática, Natal, RN, 2002, pp. 3017-3022.

[4] G.G.C. Maniçoba, Temperature control of the water cooling system of a plasma torch using fuzzy logic, Master Thesis, Federal University of Rio Grande do Norte, 2013.

[5] G.G.C. Maniçoba, A.O. Salazar, J.A.D. Amado, J.A.B. de Oliveira, J.P. Dubut, A. S. Lock, et al., Design and simulation of a thermal plasma torch with inductive coupling, in: VII CONEM, São Luiz, MA, 2012.

[6] M.F.G. Rosias, Emission Atomic Spectrometry with Inductively Coupled Plasma, 1st ed., CENA, Piracicaba, SP, 1998.

[7] N.M. Nishio, A. Takabatake, Energy Production from Waste of a Water Reuse, Graduation Project, University of São Paulo, São Paulo, SP, 2002.

[8] A.M.F. Guimarães, Development of a control system for a plant of waste blanketing by plasma, Ph.D. Thesis, Federal University of Rio Grande do Norte, 2009.

Journal of Mechanics Engineering and Automation 4 (2014) 505-510

Lightweight Concrete Using Local Industrial By-product

Deborah Olukemi Olanrewaju

Department of Building Technology, Lagos State Polytechnic, Lagos +234, Nigeria

Received: March 31, 2014 / Accepted: April 15, 20114 / Published: June 25, 2014.

Abstract: Construction is one of the largest users of energy, material resources and water and it is a formidable polluter. One of the major materials used in construction is concrete and ordinary concrete contains about 12% cement which is a major producer of greenhouse gas in the world. The use of waste materials as partial replacement of cement in concrete reduces greenhouse gases, frees up land fill space, and reduces raw materials consumption. This contributes towards sustainable development, as in a sustainable society, nature is not subject to systematically increasing concentrations of substances extracted from the earth's crust. This research work explores the possibility of replacing some percentage of cement in concrete with marble sludge powder to produce lightweight concrete. This was achieved by determining the compressive strength and some hardened properties of concrete like sorptivity and carbonation with marble sludge. The results so far have been able to prove that lightweight concrete can be produced when some percentage of cement is replaced with this waste.

Key words: Lightweight concrete, marble sludge, filler, carbonation, permeation.

1. Introduction

Industrial by-products are waste materials produced by industries as a result of production. More production equals more waste, and more waste creates environmental concerns of toxic threat. An economically viable solution to this problem should include utilization of these waste materials for new products especially in construction applications which in turn minimizes the heavy burden on the nation's landfills, saves natural resources, energy, reduces air and water pollution and also reduces the emission of green house gases. Examples of these wastes that can be used in construction works which include cement kiln dust, foundry sand, fly ash, silica fume, slag, marble sludge, and so on [1].

By virtue of its size, construction is one of the largest users of energy, material resources and water, and it is a formidable polluter [2]. There is increasing concern now that the choice of construction materials must also be governed by ecological considerations. Concrete is the major construction material in the world with 11.5 billion tons of concrete as world demand per year and the demand for concrete is expected to grow to approximately 18 billion tons a year by 2050 [3].

Ordinary concrete, typically, contains about 12% cement, 8% mixing water, and 80% aggregate by mass [3]. This means that, in addition to 1.5 billion tons of cement, the concrete industry is consuming annually 9 billion tons of sand and rock together with one billion ton of mixing water. The 11.5 billion tons a year concrete industry is, thus the largest user of natural resources in the world which if continue unchecked will result in depletion of natural resources. Greenhouse gas is also generated which is responsible for 5% CO_2 production in the world. The mining, processing and transport of huge quantities of aggregate, in addition to billions of tons of raw materials needed for the cement manufacture consume considerable energy and adversely affect the ecology of virgin lands. If the waste product of one industry is recycled as a substitute for virgin raw material of another industry, it will thereby reduce the

Corresponding author: Deborah Olukemi Olanrewaju, M.Sc., research fields: building structure & construction material research. E-mail: kemiolan@yahoo.com.

environmental impact of both. Any efforts to reduce such dependence of virgin materials will, therefore, be a contribution towards sustainable development.

Marble sludge powder is an industrial waste containing heavy metals in its constituent and it is produced from cutting of marble stone for usage in various construction applications in Nigeria. The amount of industrial waste generated due to the cutting is increasing every day; this put pressure on the limited number of land fill and suggests more sustainable use of such in construction development and in production of new products like concrete. The use of marble sludge as filler material in cement reduces the amount of natural resources required. This displaces some cement production, an energetically expensive and environmentally problematic process, while reducing both the need for land area for extracting resources and amount of industrial waste that must be disposed of.

In recent times, marble dusts have found some use in the construction industry and research has been conducted to examine their applications. An exclusive work has been done on the feasibility of the usage of quarry rock dust and marble sludge powder as hundred percent substitutes for natural sand in concrete [4]. From the study, it is found that the compressive, split tensile strength and durability studies of concrete made of quarry dust and marble sludge powder are nearly 14% more than the conventional concrete. The concrete resistance to sulphate attack was enhanced greatly, according to the experiment performed on the hardened properties of bituminous concrete with marble dust as filler [5]. Fillers are fine aggregate material that passes 0.063 mm sieve [6]. The behaviour of bituminous concrete with marble dust compared very well with bituminous concrete with lime and stone dust.

Marble powder has a very high Blaine finess value of about 1.5 m^2/g with 90% of particles, passing 50 μm sieves and 50% under 7 μm [7]. The maximum compressive and flexural strengths were observed for specimens containing 6% waste sludge when compared with control and it was also found that waste sludge up to 9% could effectively be used as an additive material in cement [8]. The result of an investigation on the abrasion resistance of concrete made by percentage substitution of sand by marble waste powder compared very well with that of conventional concrete [9]. In the same study, increment in percentage of substitution of sand caused a significant increment in the sodium sulphate resistance of concrete; whereas water penetration depth of concrete with marble powder at 15% substitution was found considerably less than that of concrete with 0 marble powder. Marble dust can also be used as filler and helps to reduce the total voids content in concrete [9]. Consequently, this contributes to improvement of strength of concrete.

The durability of concrete is a function of permeability [10], hence concrete can be made durable by reducing the extent of voids. Permeability is the movement of fluids across a porous medium as a result of pressure gradient. Thus, concrete permeability refers to its ability to transmit fluids through it caused by pressure head; this applies to the transport of both gases and liquid [11]. More research is still needed to see its wider application in concrete especially as partial replacement of cement. The objective of this study to provide more scientific evidence to support the re use of accumulated marble wastes in Nigeria; by investigating into the following hardened properties of concrete with marble sludge powders, compressive strength, permeability, sorptivity and carbonation. If this is successful there will be less demand on cement, thus providing possible solutions to environmental concerns of green house gas (CO_2) pollution, waste production and depletion of natural resources. The paper is organized as follows: Section 2 shows the characterization of materials; Section 3 explains the materials and experimental methods used in the study; Section 4 presents results and discussions; and Section 5

highlights the conclusions.

2. Characterization of Materials

The physical characteristics of the marbles sludge powder are furnished in Table 1 while the chemical characteristics of the marble sludge powder are compared with that of ordinary Portland cement is in Table 2.

3. Materials and Experimental Methods

3.1 Cement

Ordinary Portland cement that conforms to ASTM C150—standard specification for Portland cement obtained from a local commercial manufacturer in Nigeria precisely (Dangote cement) was used throughout the experiment.

3.2 Marble

Marble dust samples from Coker, Lagos State, Nigeria were crushed and grinded using laboratory crusher and ball mill and passes 0.063 mm sieve size.

3.3 Aggregates

The coarse aggregate used was crushed granite chippings with a size of 12 mm at the average.

Medium size fine aggregate from Ebute River in Ikorodu with clean tap water available in the concrete laboratory was used in manufacturing the concrete. The qualities of water samples are uniform and potable.

3.4 Specimen's Preparation

The batching of concrete was done by weighing the different constituent materials based on the adopted mix ration of 1:2:4 and 1:3:6. In the first ratio labeled mix A, cement was replaced by marble dust at 0, 5, 10 and 20% (represented by mix codes MA_1, MA_2, MA_3 and MA_4). The same was done for the second ratio labeled mix B (represented by mix codes MB_1, MB_2, MB_3 and MB_4).

The water cement ratio for both two mixes was 0.65% by weight. The freshly mixed concrete was then filled in 150 mm by 150 mm moulds in approximately 50 mm layers with each layer given 35 strokes of the tamping rod. Samples were held in the laboratory at an atmosphere of more than 95% relative humidity and ambient temperature, i.e., 25 °C. The moulds were opened after 24 h and the specimens were stored in the humid bath for 28 days curing age.

3.5 Test Procedure

The 150 mm size concrete cubes were used as test specimens to determine the compressive strength. The test specimen at the end of 28 curing days were subjected to compressive load from a 214 × 250 shambhavimpe compression testing machine until failure.

3.6 Durability studies

The object of this durability study is to investigate the permeability through sorptivity test and resistance to carbon attack for both conventional concrete and concrete with % replacement of cement. Sorptivity test was conducted over six hours. The water sorptivity test measures the rate of movement of water front through the concrete under capillary suction. The specimens after dried were saw-cut in

Table 1 Physical characteristics of marble powder.

Material	Moisture content (%)	Bulk density (kg/m^3)	Fineness modulus	Effective size (mm)	Coefficient of uniformity	Coefficient of gradation	Wet dry
Marble powder	23.35	1.59	1,118	2.04	0.17	1.58	1.37

Table 2 Chemical characteristics of marble sludge powder and Portland cement.

Material	Fe_2O_3	MnO	Na_2O	MgO	K_2O	Al_2O_3	CaO	SiO_2
	%wt	%wt	%wt	%wt	%wt	%wt	%wt	%wt

Marble	11.99	0.08	2.08	8.74	2.33	4.45	1.58	64.86
Portland cement	2.27	0.045	0.75	2.24	0.70	5.86	64.07	20.15

pieces (75 × 150 mm^2). The surfaces of the concrete samples were then placed in water. For each mass determination, the test specimens were removed from water and the surfaces cleaned with a dampened paper towel to remove water droplets. The mass of the samples were then measured and were replaced to continue the test. The cumulative change in mass 1, 2, 3, 4, 5 and 6 hours were used to obtain the respective cumulative absorption values (i) expressed as Eq (1):

$$i = \Delta m/A\ell \quad (1)$$

where, Δm = cumulative change in mass due to water absorption, A = cross-sectional area of test specimen (mm^2) and ℓ = density of water (10^3 kg/m^3)

As soon as concrete is formed, the carbon dioxide in the air reacts with the calcium hydroxide, forming calcium carbonate, a process known as carbonation. For the carbonation test of the samples, phenolphthalein indicator solution was applied to fresh fractured surface of concrete. The indicator turns purple at PH above 8.6 and remains colourless when the PH of the concrete is below 8.6, suggesting carbonation. A fully carbonated paste has a PH of about 8.4. In practice, strong immediate colour change to purple suggest a PH that is rather higher, perhaps PH 9.0 or 10.0.

4. Results and Discussion

4.1 Compressive Strength Development

Compressive strength tests were conducted in accordance with BS EN12390-3:2009 [12] on all cubes of the two mixed ratios at 28 curing days. Compressive strength test results are shown in Table 3 and Fig.1. MDC (marble dust concrete) showed a reduction in compressive strength compared to the control PC concrete. This confirms that different mixes of concrete ingredients produce different strengths which are measured in MPa [13]. Different strengths of concrete are used for different purposes; very low-strength (14 MPa or less) concrete maybe used when the concrete must be lightweight [13].

Table 3 Average compressive strength in N/mm^2 at 28 days.

MIX	% Marble concentration			
	0	5	10	20
MIX A	29.3	20.5	19.6	19.1
MIX B	24	15.3	15.1	9.6

4.2 Applications of Lightweight Concrete in Construction

- Curtain walls for high-rise construction;
- Highway sound barriers;
- Low cost insulated walls for residential buildings;
- Tilt up panels;
- Façade tiles for an architectural application;
- Repairs on a bridge;
- Slope protection;
- Aircraft arresting beds;
- Foundations for roads and sidewalks;
- Subsurface for sport arenas, e.g., tennis courts;
- Explosion-resistant structures.

4.3 Permeation Test

Sorptivity test was conducted over six hours and the cumulative change in mass at specific intervals was determined. The results in Fig. 2 show decrease in sorptivity as the level of replacement of cement increases. This means marble dust can be used as filler and helps to reduce the total voids content in concrete. This result is in line with Ref. [9].

4.4 Carbonation Test

Phenolphthalein indicator solution was used to achieve the carbonation test. There was strong immediate colour change to purple in all the samples which suggest a PH that is rather higher perhaps PH 9.0 or 10.0, but within 24 hours, the specimen begin to turn colourless. The result of carbonation test of MDC

compares very well with control concrete. The penetration rate of carbonation increases with increase in exposure time for all samples with faster rate in MDC. This improves the compressive and tensile

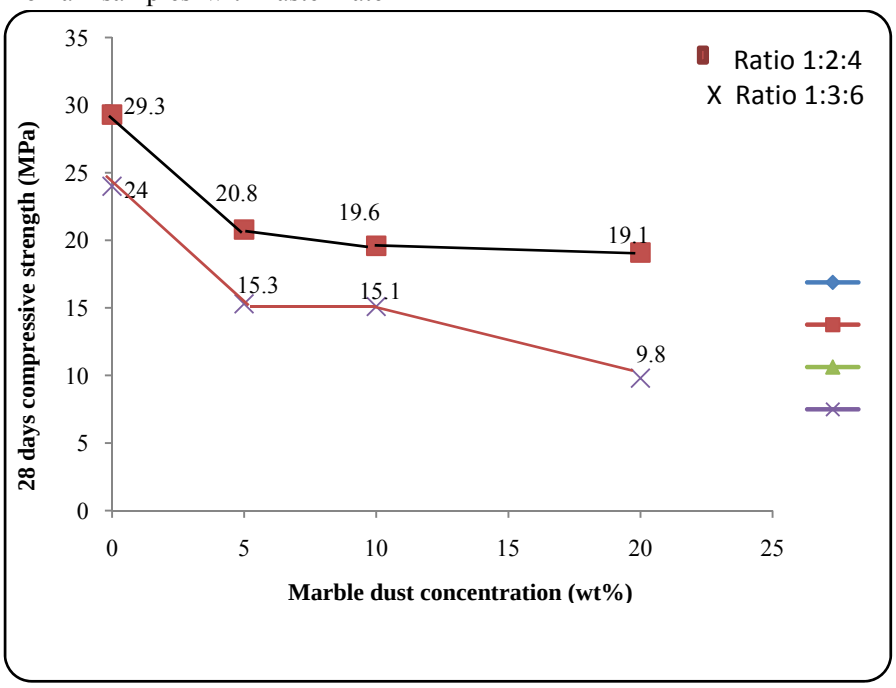

Fig. 1 Compressive strength of concrete samples.

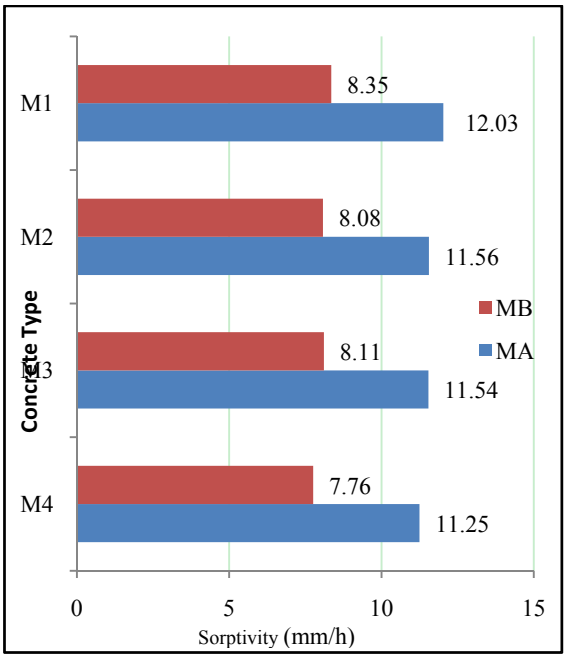

Fig. 2 Sorptivity and concrete type.

strength of concrete by reducing the porosity of dense and compact concrete, protecting it against water and chloride ion infiltration. Chloride ions can corrode the steel placed in reinforced concrete. It is important to keep these advantages in mind because the carbonation is an inevitable process for concrete to undergo.

5. Conclusions

From the above study, it is concluded that the marble sludge powder may be used as a partial replacement material for cement in producing lightweight concrete. The investigation was primarily to find solution to the disposal problem of marble dust. The disposal of this waste material can lead to the following environmental problems:

- If the waste is disposed on soils, the porosity and permeability of top soil will be reduced, the fine marble dust reduces the fertility of the soil by increasing its alkalinity;
- When dumped, marble powder suspends in the air and slowly spread out through wind to the nearby area;
- When dumped along a catchment area of natural rainwater, it results in contamination of over ground water reservoir and also causes drainage problem.

Acknowledgements

The author thanks the members of Yaba College of Technology Concrete Workshop staff for providing the needed support for the success of this research work.

References

[1] B. Johnny, A. Taher, F. Ellie, Utilization of recycled and waste materials in various construction applications, American Journal of Environmental Sciences 9 (1) (2013) 14-24.

[2] H. Arpad, Construction Materials and Environment, Annu. Rev. Environ. Resource (29) (2004) 181-204.

[3] P.K. Mehta, P.J.M. Monteiro, Concrete: Microstructure, Properties and Materials, McGraw-Hill Professional, USA, 2013.

[4] H.M. Shahul, A.S.S. Sekar, Properties of green concrete containing quarry rock dust and marble sludge powder as fine aggregate, ARPN Journal of Engineering and Applied Sciences 4 (4) (2009) 83-89.

[5] C. Satish, R. Choudhary, Performance characteristics of bituminous concrete with industrial wastes as filler, Journal of Materials in Civil Engineering 25 (11) (2013) 1666-1673.

[6] BSI. BS EN 197-1:2000, Cement Composition, Specification and Conformity Criteria for Common Cements.

[7] C. Valeria, M. Giacomo, R.N. Tarun, Characterisation of Marble powder for its use in mortar and concrete, in: NMET/ACI International Symposium on Sustainable Development of Cement and Concrete, Toronto, Canada, Oct. 5-7, 2005.

[8] T. Salih, Physico-chemical treatment of marble processing wastewater and the recycling of its sludge, Materials Science and Engineering 419 (1-2) (2006) 306-309.

[9] H. Houari, H. Hebhoub, H. Aoun, M. Belachia, Use of waste marble aggregates in concrete, Construction Build Mater 25 (2011) 1167-1171.

[10] B. Bogale, Comparison of concrete durability as produced by various cements manufactured in Ethiopia, M.Sc. Thesis, Addis Ababa University School of Graduate Studies, 2007.

[11] Literature Review Summary Increased Mineral Addition Online, http://www4.umw.edu/cbu/papers/200320CBU20Reports/REP–525-pdf.

[12] BSI. BS EN 12390-3: 200, Testing Hardened Concrete-Compressive Strength of Test.

[13] Structural Lightweight Concrete-Concrete Construction, The Aberdeen Group, Mar. 1981.

Journal of Mechanics Engineering and Automation 4 (2014) 511-520

Electromagnetic Torque Estimation of a Three-Phase Induction Motor for Setting the Feedrate of a Milling Machine

Élida Fernanda Xavier Júlio[1], Simplício Arnaud da Silva[2], Cícero da Rocha Souto[2] and Isaac Soares de Freitas[2]

1. Postgraduation Program in Mechanical Engineering, Federal University of Paraíba, João Pessoa 58059-900, Brazil

2. Department of Electrical Engineering, Federal University of Paraíba, João Pessoa 58059-900, Brazil

Received: March 11, 2014 / Accepted: March 31, 2014 / Published: June 25, 2014.

Abstract: In this paper, it presents a project of a fuzzy controller and a neural estimator to control a coordinate table powered by three-phase induction motor, aiming to implement an intelligent milling system. The position/speed control is performed using vector techniques of three-phase induction machines. The estimation of the motor electromagnetic torque is used for setting the feedrate of the table. The speed control is developed using TS (Takagi-Sugeno) fuzzy logic model and electromagnetic torque estimation using neural network type LMS (least mean square) algorithm. The induction motor is powered by a frequency inverter driven by a DSP (digital signal processor). Control strategies are implemented in DSP. Simulation results are presented for evaluating the performance of the system.

Key words: Machining, speed control, torque estimation, fuzzy logic, neural network.

1. Introduction

Milling is a machining process in which the piece material removal takes place intermittently. The milling is accomplished by the combination of two movements performed simultaneously. One of the movements is rotation of the cutter around its axis. The other is the movement of the milling machine table, which is attached to the piece to be milled. Thus, cutting parameters such as feedrate, cutting speed and cutting depth should be analyzed [1]. According to Ref. [2], parameters of the machining process should be monitored and adjusted automatically, which can improve the production quality and reduce the machining time.

With advancements in applications using induction motors, the use of these motors on start and controlling of positioning systems are majority in the industry. An example of positioner machine is the coordinate table, which has applicability to devices milling, turning, drilling, and welding, among others. The milling operation is one of the most important in the process of mechanical machining.

The three-phase induction motor is widely used in various applications in industry, due to its relative simplicity of construction, maintenance, both operational and market low cost, as well as, the capacity to operate with a wide range of loads in adverse conditions. One of the factors that provided the advancement in driving of three-phase induction motor was the development of control strategies, specifically vector control strategies.

In induction machine, the implementation of vector control for field orientation can be done by direct or indirect method. The direct field orientation enables the position of the flux to be determined by measuring terminal quantities of the stator (voltages and currents).

Corresponding author: Élida Fernanda Xavier Júlio, Ph.D. student, electrical engineer, research fields: control systems, electric drives, fuzzy logic and artificial neural network. E-mail: elida_xnet@yahoo.com.br.

The advantage of using the stator terminal quantities lies in the fact to be sensitive only to the stator resistance [3].

In the development of controllers and estimators, the use of vector control and the application of intelligent control techniques, such as fuzzy logic and ANN (artificial neural network), provided greater robustness to systems powered by three-phase induction motors.

Fuzzy logic is a technique that allows the implementation of human experience in systems, considering the uncertainty of information, the ambiguities, for the development of controllers. The fuzzy inference model type TS (Takagi-Sugeno) is capable of representing, approximately or exactly, any nonlinear dynamics as combination of locally valid linear models, interpolating smoothly [4]. The TS fuzzy model is a hybrid approach [5], because it combines a fuzzy method based on rules and a mathematical method, consisting of conditional propositions, whose antecedents are linguistic variables and whose consequents are linear equations [6].

The ANN is a computational technique organized according on human neural structures and acquires knowledge from experience, consisting of inherently parallel and adaptive processing [7]. This technology has the proper way to store knowledge and evaluate them for use [8]. This knowledge is acquired through a learning process and stored in a distributed manner. The learning objective is to obtain an implicit model of the system under study by adjusting the parameters of the neural network [9].

In machining systems, a structure consisting of ANN and data set was applied in Ref. [10] in order to obtain the inference of knowledge of a fuzzy model for an end milling process. The inference, based on fuzzy learning, was used as a mechanism of intelligent determination of advancement.

The signal digital processor is a device that performs signal acquisition and large number of mathematical operations with fast and efficient processing in the range of microseconds, enabling the application in high performance systems operating in real time [11]. This equipment is well suited for the implementation of control and estimation strategies, which have complex calculations to be performed in real time.

This paper presents simulated results for the development of a driving and control system of a vertical milling machine. This system drives the coordinate table of the milling machine with specific feedrate for machining of material of a piece.

As the coordinate table is driven by three-phase induction motor, the angular position control and the rotor rotational speed control of this motor are carried out. This speed of the three-phase induction motor is controlled using TS fuzzy control system.

The electromagnetic torque of the motor is estimated in order to identify the material of the machined piece and to define the feedrate of the table. For this estimation, it is used an ANN type LMS (least mean square) algorithm.

The paper is organized as follows: Section 2 presents the development of the driving and control system of the milling machine table; Section 3 shows the simulation results obtained; and Section 4 presents the comments and conclusions about this paper and the perspective of future work.

2. System Development

For the experimental setup of the milling machine, design shown in Fig. 1, it will be used an *X*-*Y* coordinate table composed by two perpendicular bases to each other, *X* and *Y*, which move linearly in the horizontal plane. The *X* base of the table (upper base) has a course of 200 mm and the *Y* base (lower base) of 100 mm, whose trapezoidal spindles have a pitch of 4 mm for ten revolutions of the motor shaft. Each base of the table is driven by a three-phase induction motor. The drive of the *X* base results in displacements in the right and left directions, and the *Y* base results in forward and backward displacements.

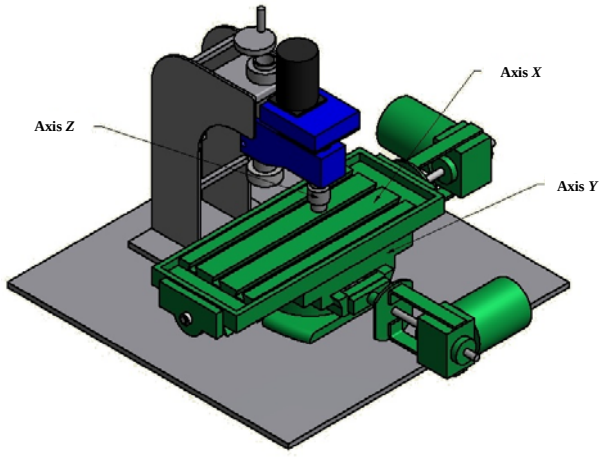

Fig. 1 Vertical milling machine design.

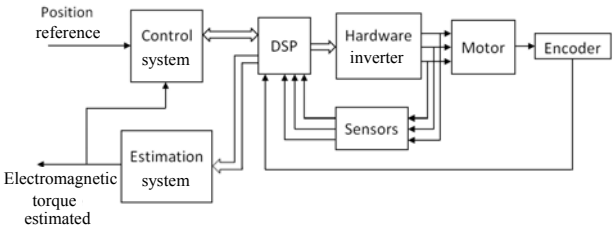

Fig. 2 Schematic diagram for the control of the coordinate table.

A tool of end mill will be attached on the mandrel, located in the spindle of the milling machine. The cutter, running through a cutting depth in the *Z* axis, will perform chip removal of a piece fixed to the *X* base.

Due to the work of piece machining, an electromagnetic torque will be imposed on the induction motor of the *X* base. The information of the electromagnetic torque estimated will characterize the type of material constituent of the piece. This signal of the estimated torque will be used to specify, in real time, the drive speed of the *X* base.

In Fig. 2, the system configuration for the drive and control of the *X* base of the coordinate table is schematized. In this diagram, it can be observed not only the control system, developed to drive and control the three-phase induction motor of the *X* base, but also the estimation system of the electromagnetic torque of this motor.

A DSP is used for processing, transmission and data acquisition. Hardware consists of a three-phase voltage inverter will power the three-phase induction motor of the table. An encoder is coupled to the motor shaft in order to obtain the angular position of the rotor of this machine and thus the linear position of the *X* base. And sensors are used to obtain the phase currents and phase voltages of the motor.

2.1 Control System

The control system of the three-phase induction motor was implemented in closed loop, where it was developed: a current controller using a PI (proportional-integral) controller and a speed controller through fuzzy model TS.

The speed controller is composed of a fuzzy PD base, TS model with an input of Error and another Derror and the integration of the Error. In Fig. 3, it is presented the structure of the PD + I speed fuzzy controller used, in which i_{ts} is the output variable of the fuzzy PD base, k_p is the gain and i_{sq}^{b*} is the control variable. The variable i_{sq}^{b*} corresponds to the stator current of the three-phase induction motor, *q* component in referential of the rotor flux.

Next, the settings for fuzzification, fuzzy inference and defuzzification of the developed fuzzy PD base are presented.

In the fuzzification stage, Error and Derror input variables are defined, respectively, by the difference between the reference value and the value of the rotor rotational speed ω_r, and by the derivative of this error. The universes of discourse of the Error and Derror comprise a normalized range from -1 to 1.

The variable Error is composed of seven pertinence functions with triangular and trapezoidal shapes

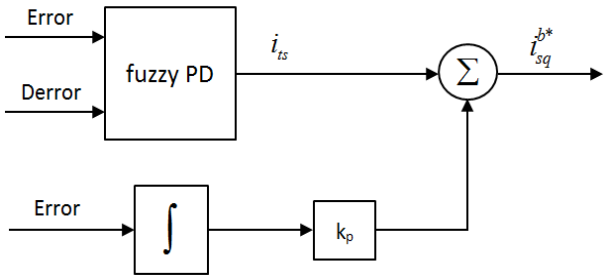

Fig. 3 PD + I speed fuzzy controller.

called: NB (negative big), NM (negative medium), NS (negative small), AZ (almost zero), PS (positive small), PM (positive medium) and PB (positive big). In Fig. 4, it is presented the arrangement of linguistic terms of the Error in their universe of discourse.

For variable Derror, it was associated seven pertinence functions, with triangular and trapezoidal shapes, defined by the terms: NB, NM, NS, AZ, PS, PM and PB. In Fig. 5, these functions are shown.

In the stage of fuzzy inference, it is determined how the control rules are activated. In Table 1, the forty-nine control rules developed are inserted.

Control rules consist of conditional sentences. For the composition of each rule and for the relationship between them, the max-min inference technique was used. Thus, each sentence is modeled by the minimal application and the relationships between rules are modeled by the maximal application.

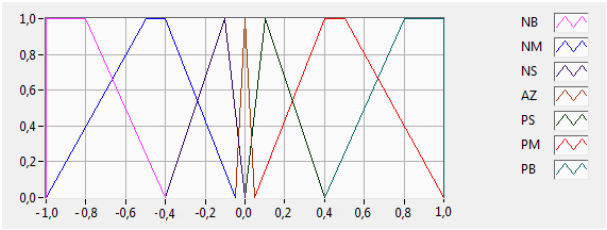

Fig. 4 Pertinence functions of the Error input variable.

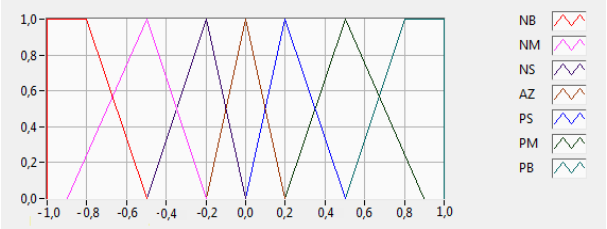

Fig. 5 Pertinence functions of the Derror input variable.

Table 1 Table of fuzzy rules of the speed controller.

Error \ Derror	NB	NM	NS	AZ	PS	PM	PB
NB	*iNB*	*iNB*	*iNB*	*iNB*	*iPM*	*iPB*	*iPB*
NM	*iNB*	*iNB*	*iNB*	*iNM*	*iPS*	*iAZ*	*iPB*
NS	*iNB*	*iNB*	*iNM*	*iNS*	*iAZ*	*iPS*	*iPM*
AZ	*iPB*	*iPM*	*iPS*	*iAZ*	*iNS*	*iNM*	*iNB*
PS	*iNM*	*iNS*	*iAZ*	*iPS*	*iPM*	*iPB*	*iPB*
PM	*iNB*	*iAZ*	*iNS*	*iPM*	*iPB*	*iPB*	*iPB*
PB	*iNB*	*iNB*	*iNM*	*iPB*	*iPB*	*iPB*	*iPB*

In the defuzzification, the i_{ts} output variable is generated, according to the PD fuzzy output shown in Fig. 3. According to TS fuzzy method, at this stage, a linear and time-invariant model is determined [12].

In Eq. (1), i_{ts} variable is obtained by a weighted average, in which the i_{tsx}, i_{tsy} and i_{tsz} terms are expressed by Eqs. (2)-(4), respectively. This equation consists of linear functions, defined from the consequents of control rules and the numerical values of the Error and Derror input variables.

$$i_{ts} = \frac{i_{tsx} + i_{tsy} + i_{tsz}}{iNB + iNM + iNS + iAZ + iPB + iPM + iPS} \tag{1}$$

$$\begin{aligned} i_{tsx} = {} & iNB(30 \cdot Error - 0.1 \cdot Derror) + \\ & iNM(70 \cdot Error - 0.3 \cdot Derror) + \\ & iNS(90 \cdot Error - 0.5 \cdot Derror) \end{aligned} \tag{2}$$

$$i_{tsy} = iAZ(1.0 \cdot Error - 1.0 \cdot Derror) \tag{3}$$

$$\begin{aligned} i_{tsz} = {} & iPB(30 \cdot Error - 0.1 \cdot Derror) + \\ & iPM(70 \cdot Error - 0.3 \cdot Derror) + \\ & iPS(90 \cdot Error - 0.5 \cdot Derror) \end{aligned} \tag{4}$$

The project of the current controller was developed from the complex model of representation of a three-phase induction machine, using the control quadrature with referential in rotor flux (b).

Through the realization of mathematical simplifications, it was obtained the transfer function used in the project of current controller as in Eq. (5), where I_s^b and $V_s^{b'}$ correspond to the stator current and stator voltage of the three-phase induction motor in the referential of the rotor flux, respectively. Eqs. (6) and (7) are constituted by the parameters of the three-phase induction motor, in which l_s is the cyclic stator inductance, l_r is the cyclic rotor inductance, l_m is the cyclic mutual inductance, R_s is the stator resistance and τ_r is the rotor time constant.

$$I_s^b = \frac{l_r \sigma}{(s + \eta)} V_s^{b'} \tag{5}$$

$$\sigma = \frac{1}{l_s l_r - l_m^2} \tag{6}$$

$$\eta = l_r \sigma R_s + \frac{\sigma l_m^2}{\tau_r} \tag{7}$$

For the development of the current controller, a PI classical controller whose gains k_{p_i} and k_{i_i} were

determined by Eqs. (8) and (9), respectively, was used. In Eq. (8), T_v is the time constant of the source.

$$k_{p_i} = \frac{1}{4T_v l_r \sigma} \tag{8}$$

$$k_{i_i} = \eta \cdot k_{p_i} \tag{9}$$

2.2 Estimation System

From the complex model of representation of three-phase induction machine, it developed the estimation project of the electromagnetic torque of the three-phase induction motor, using control quadrature with fixed reference in the stator (a) and applying a ANN type LMS algorithm.

An equation widely used to estimate the electromagnetic torque is Eq. (10), which is written in terms of the components of the stator flux and stator current. Thus, for the estimation of electromagnetic torque, stator flux of the three-phase induction motor was firstly estimated.

$$ce = P\left(i_{sq}^{a}\lambda_{sd}^{a} - i_{sd}^{a}\lambda_{sq}^{a}\right) \tag{10}$$

In applying the voltage model of the machine and in the direct field orientation with reference by stator flux, the estimate stator flux λ_s^a is obtained by integrating the counter-electromotive force. Eqs. (11) and (12) correspond to the stator flux in the *d* and *q* components, respectively. The stator voltage v_s^a and stator current i_s^a variables were obtained from the motor terminals. The stator resistance R_s is considered constant and equal to 5.1 Ω.

$$\lambda_{sd}^{a} = \int\left(v_{sd}^{a} - R_s i_{\mathrm{sd}}^{a}\right)\mathrm{d}t \tag{11}$$

$$\lambda_{sq}^{a} = \int\left(v_{sq}^{a} - R_s i_{\mathrm{sq}}^{a}\right)\mathrm{d}t \tag{12}$$

The integration procedure of counter-electromotive force originates levels of continuous current called offset in the estimation of the stator flux, implying, therefore, on an estimation of electromagnetic torque with not tolerable errors.

For eliminating the offset on the flux signal, a neural adaptive filter was developed by the LMS algorithm technique. A neural structure was implemented for each flux component, *d* and *q*, similarly.

In Fig. 6, this structure is presented for the *d* component, consisting of only one neuron and a bias, as synaptic weight, with constant input equal to 1. The neural structure has, as input, the signal from the estimated stator flux λ_{sd}^a and the filtrated estimated stator flux λ_{sdf}^a is obtained in the output. The filtering process is performed by subtracting "*y*" of the input signal λ_{sd}^a.

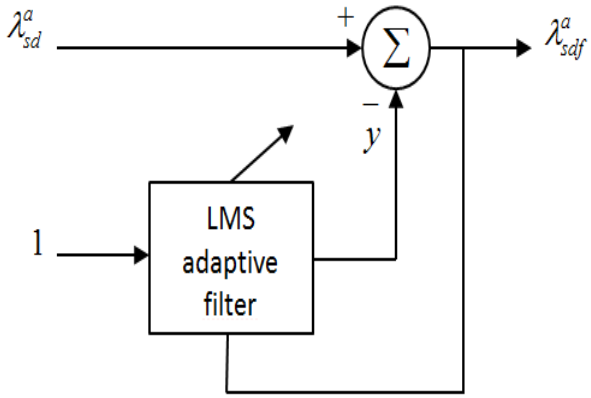

Fig. 6 Neural structure with LMS adaptive filter.

The algorithm developed for representation of the neural structure is described in Eqs. (13) and (14), where $y(n)$ is the filter output at the current instant and $y(n + 1)$ is the filter output at the next instant. Through this algorithm, an adaptive iteration was effected to each acquisition of the input data.

$$\lambda_{sdf}^{a} = \lambda_{sd}^{a} - y(n) \tag{13}$$

$$y(n+1) = y(n) + 2\mu\lambda_{sdf}^{a} \tag{14}$$

The learning rate μ used in Eq. (14) was calculated by Eq. (15), so that μ is obtained in function of speed ω_r because specific learning rates, due to variation of speed ω_r, were required.

$$\mu = -3.5625 \cdot 10^{-7} \cdot \omega_{\mathrm{r}} + 2.4884375 \cdot 10^{-4} \tag{15}$$

After the estimation of the stator flux and the elimination of the offset in the flux signal, the electromagnetic torque of the motor was estimated using Eq. (16). In Eq. (16), the estimated

electromagnetic torque ce_{est} is determined using the filtered estimated stator flux, λ^a_{sdf} and λ^a_{sqf}, the stator current, i^a_{sd} and i^a_{sq}, and the constant of the number of pairs of poles P of the three-phase induction motor, which is equal to two.

$$ce_{est} = P\left(i^a_{sq}\lambda^a_{sdf} - i^a_{sd}\lambda^a_{sqf}\right) \quad (16)$$

3. Simulation Results

In milling system, the objective is to drive the X base of the table for machining pieces constituted by different materials. To perform this study in the simulation of the operation of the three-phase induction motor, the application of various loads to the motor was simulated and information of the torque signal ce_{est} was used in the specification of the speed reference of rotation of the rotor ω^*_r for the motor drive.

The milling machine table performs a displacement of 4 mm for every ten revolutions of the motor shaft. Therefore, it was determined a numerical factor of the relationship between the magnitudes of linear displacement and linear speed of the table and the magnitudes of angular displacement and angular speed of the three-phase induction motor, that is 0.064 mm/rad.

In Table 2, the values, in module, are shown: the electromagnetic torques ce and their speed references ω^*_r, and, through the ratio factor, the equivalent speed references of the X base v*.

For analysis of the response curves, the induction motor is driven by references the type of step position, with amplitudes of 1,562.5 rad and -1,562.5 rad, resulting in rotation of the motor shaft in clockwise and anticlockwise directions. The aim is to analyze the displacement of the X base in right and left directions, along its 200 mm course.

The simulated three-phase induction motor has the following parameters: R_s = 5.1 Ω, R_r = 4.4578 Ω, $l_s = l_r$ = 0.334 H, l_m = 0.3185 H, F = 0.0041 Nms and J = 0.041 kgm^2. The simulation was performed in C language using the C++Builder® XE computer program and response curves were plotted using the Matlab™ program.

Table 2 Electromagnetic torques and reference speeds (values in module).

ce (Nm)	ω^*_r (rad/s)	v* (mm/s)
1.0	31.0	1.984
2.0	27.0	1.728
3.0	23.0	1.472
4.0	19.0	1.216
5.0	15.0	0.960

3.1 First Simulation

Initially, in Fig. 7, the response and reference curves of the variable angular position of the rotor are presented. In this first simulation, the induction motor was driven with a step type reference signal with amplitude of 1,562.5 rad, applying a load of 1 Nm from starting of the machine and, after 30 s of operation, a load of 3 Nm was applied. Due to load applications, electromagnetic torques were imposed to the three-phase induction motor.

In Fig. 8, the response and reference curves of the variable position of the X base are shown, in which the step reference signal with amplitude of 100 mm is equivalent to a step of 1,562.5 rad. This amplitude of linear magnitude corresponds to a displacement of the X base of the table to position 100 mm. Through the graphics of Figs. 7 and 8, it was possible to verify a settling time of 57.72 s, a steady state error of 0.13% and non-occurrence of overshoot.

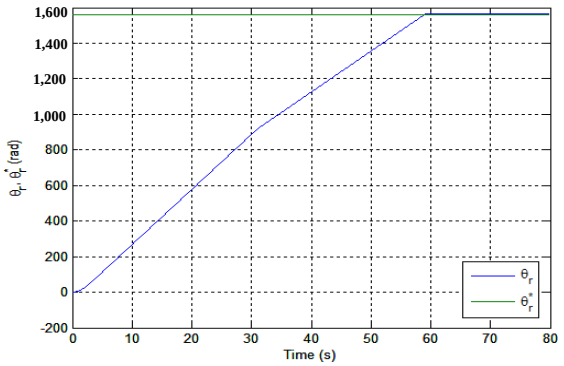

Fig. 7 Response and reference curves of the angular position of the rotor.

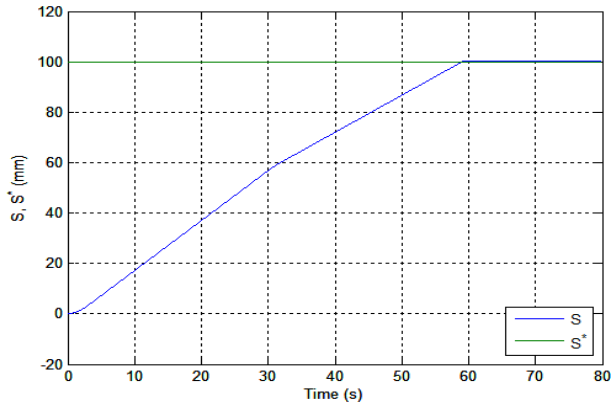

Fig. 8 Response and reference curves of the position of the *X* base.

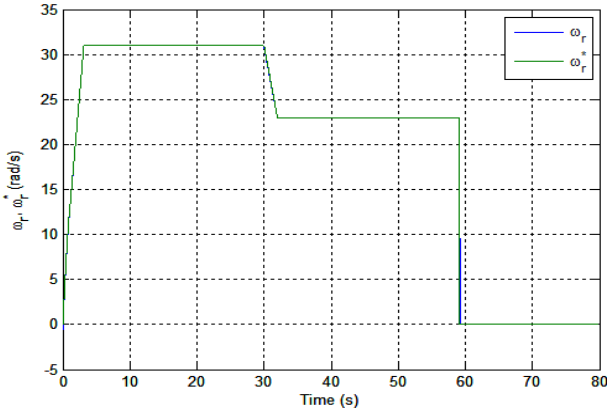

Fig. 9 Response and reference curves of rotational speed of the rotor.

Then, in Fig. 9, the reference curve of rotational speed of the rotor and the response curve obtained are presented. In this curve, it can be observed the three-phase induction motor drive by a ramp signal speed with amplitude of 31 rad/s, in the upward direction, keeping constant speed until the instant of 30 s. This constant speed of 31 rad/s corresponds to the ω_r^* excitation due to an estimation of electromagnetic torque of 1 Nm, according to Table 2. At the instant 30 s, due to the estimation of electromagnetic torque of 3 Nm, a speed ramp with an amplitude of 23 rad/s was observed in the downward direction, remaining constant up to a drive ω_r^* at null value, thus, resulting in the braking of the three-phase induction motor.

In Fig. 10, the response and reference curves of the *X* base speed are shown, in which the amplitude of 1.984 mm/s of the ramp reference was equivalent to the 31 rad/s amplitude, and amplitude of 1.472 mm/s was equivalent to the amplitude of 23 rad/s. By analyzing the graphics of Figs. 9 and 10, null steady state errors were observed in the time interval in which speed references were constant.

Following, the response and reference curves of the stator current in the *d* and *q* components were analyzed, as shown in Figs. 11 and 12, respectively. In these graphics, the control of both components of the stator current was verified. In Fig. 12, it was possible to observe the behavior of the i_{sq}^{b*} control variable curve, generated by the fuzzy controller of speed, verifying

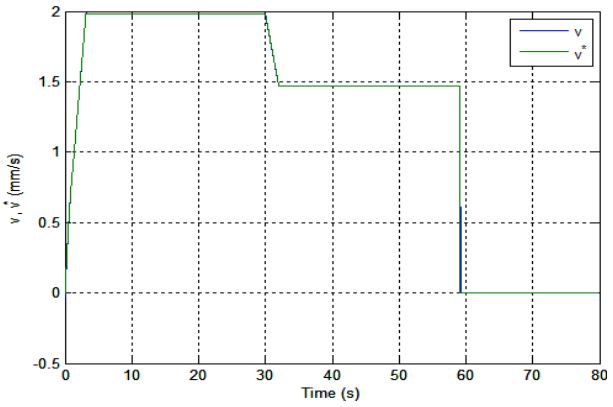

Fig. 10 Response and reference curves of *X* base speed.

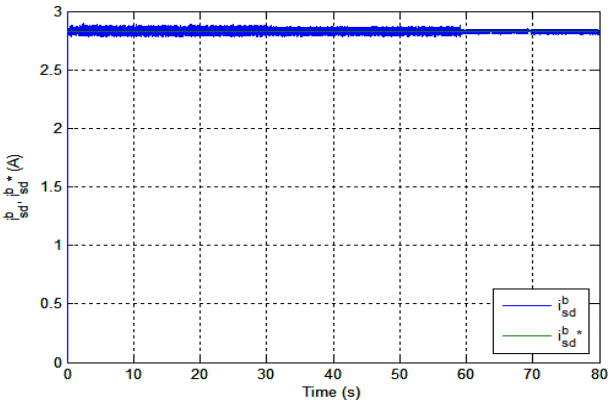

Fig. 11 Response and reference curves of the stator current in the *d* component.

the current increase from 30 s, moment from which the electromagnetic torque imposed on the three-phase induction motor was increased from 1 Nm to 3 Nm.

For the analysis of neural estimation of the electromagnetic torque in Fig. 13, the *ce* electromagnetic torque curve obtained by modeling of

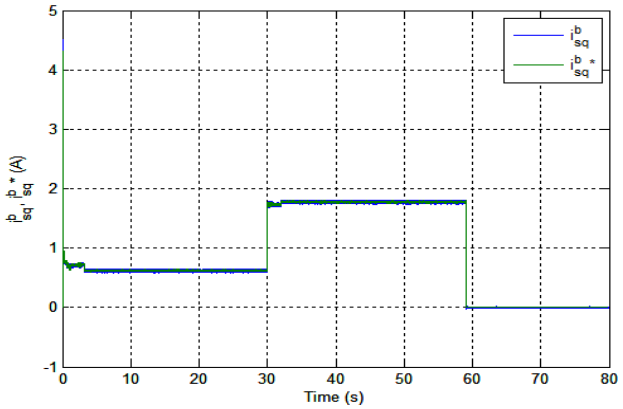

Fig. 12 Response and reference curves of the stator current in the *q* component.

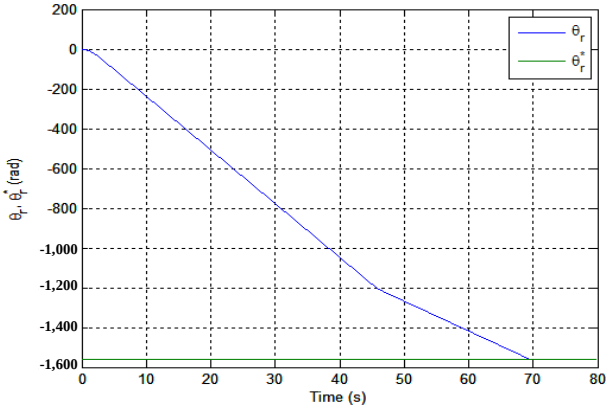

Fig. 14 Response and reference curves of the angular position of the rotor.

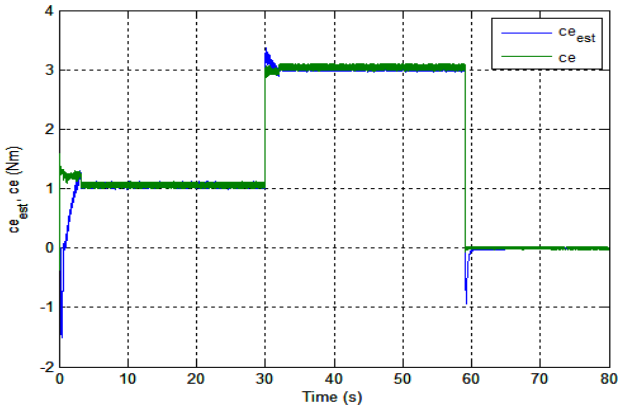

Fig. 13 Curves of the electromagnetic torque and of the estimated electromagnetic torque.

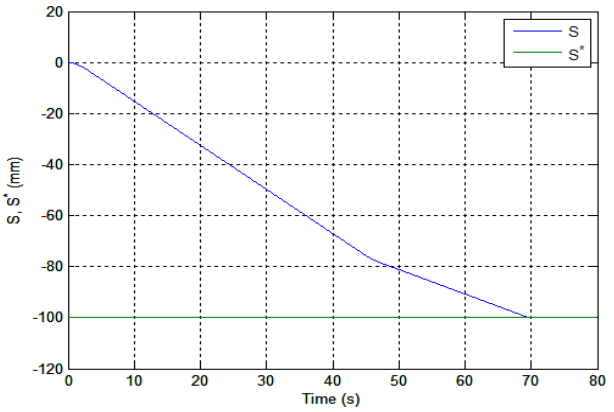

Fig. 15 Response and reference curves of the position of the *X* base.

the motor using Eq. (10), and the ce_{est} estimated electromagnetic torque curve obtained by Eq. (16) were observed. In this graphic, the behavior of ce_{est} torque in the load transitory and in the steady state of estimation was verified. For applications of the first load 1 Nm and the second load 3 Nm, distinctions between *ce* and ce_{est} curves were rarely observed in the steady state.

3.2 Second Simulation

In this simulation, firstly, a load of -2 Nm was applied, and after 45 s of operation, a -5 Nm load was applied.

In Fig. 14, the response and reference curves of angular position of the rotor are shown for a motor drive by step reference signal with amplitude of -1,562.5 rad. In Fig. 15, the response curve and the step reference of the position of the *X* base with amplitude of -100 mm are presented. This amplitude in millimeters is equivalent to a step of -1,562.5 rad, corresponding to a position of -100 mm in the *X* base. Through the graphics of Figs. 14 and 15, it was possible to verify a settling time of 67.65 s, a steady state error of 0.03% and non-occurrence of overshoot.

Then, in Fig. 16, the reference curve of the rotation speed of the rotor and the response curve obtained are shown. In this graphic, the excitation of the machine for speed ramp with amplitude of -27 rad/s was in the downward direction, keeping constant speed until the instant of 45 s. This constant speed of -27 rad/s corresponded to the ω_r^* reference due to an estimation of electromagnetic torque of -2 Nm. At the instant of 45 s, due to torque estimation of -5 Nm, a speed ramp with amplitude of -15 rad/s was used, in the upward direction, remaining constant up to a drive ω_r^* at null value.

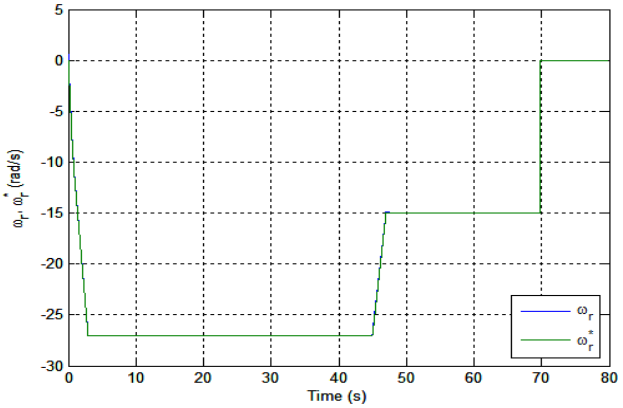

Fig. 16 Response and reference curves of rotational speed of the rotor.

In Fig. 17, the response and reference curves of the *X* base speed are presented, in which the amplitude of -1.728 mm/s of the reference ramp is equivalent to the amplitude of -27 rad/s, and the amplitude of -0.96 mm/s is equivalent to the amplitude of -15 rad/s. Through the graphics of Figs. 16 and 17, null steady state errors were observed in the time interval in which speed references were constant.

In Figs. 18 and 19, the components of the stator current *d* and *q* are presented, respectively. In these graphics, it was verified that the components of the stator current were controlled. In Fig. 19, from 45 s, the increase of the module of the currents i_{sq}^{b*} and i_{sq}^{b} was verified, because, from that instant, the module of the electromagnetic torque imposed on the motor was increased from -2 Nm to -5 Nm.

In Fig. 20, the curves of the *ce* electromagnetic torque and of the ce_{est} estimated electromagnetic torque

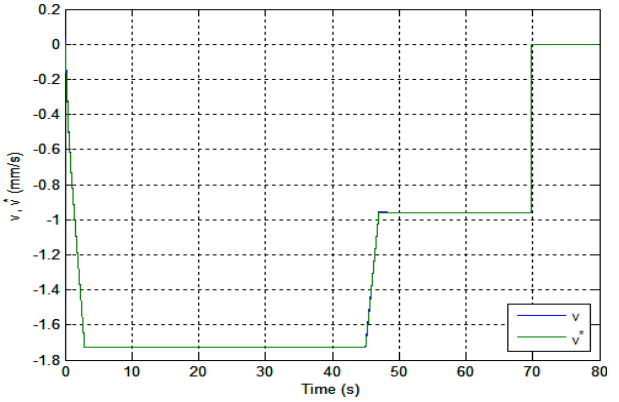

Fig. 17 Response and reference curves of the *X* base speed.

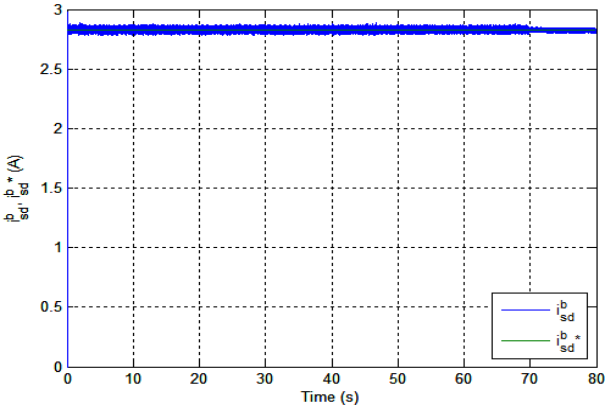

Fig. 18 Response and reference curves of the stator current in the *d* component.

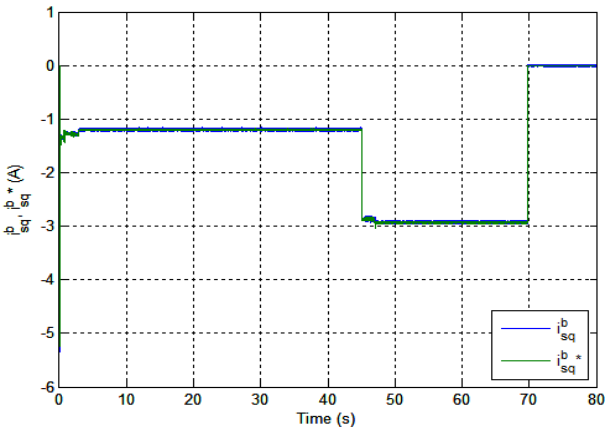

Fig. 19 Response and reference curves of the stator current in the *q* component.

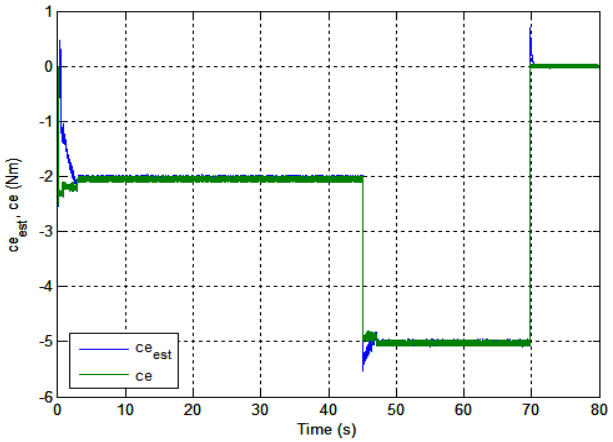

Fig. 20 Curves of the electromagnetic torque and of the estimated electromagnetic torque.

are shown. In this graphic, it was possible to verify the behavior of the ce_{est} torque in the load transitory and in the steady state of estimation. In the steady state, distinctions between *ce* and ce_{est} curves were rarely observed.

4. Conclusions

In this work, the simulation of a control system for application in a milling system was presented. A three-phase induction motor was used and controlled by intelligent control techniques to drive the milling machine table.

The performance of the control system was verified for the two directions of displacement of *X* base of the table with changes in the electromagnetic torque imposed on the motor.

In analyzing the results, a criterion of 2% of the amplitudes of the references was used. Through the response curves of the two simulations, a maximum steady state error of 0.13% was verified for the variable position, not existing overshoot in any of the tests. For the speed, the fuzzy controller made possible the obtaining of null steady state errors in both simulations, at intervals drive with constant speeds. Regarding the electromagnetic torque, the convergence of the two signals of torque estimation was observed, obtaining small errors in comparing the curves of *ce* and of ce_{est} in the steady state.

The fuzzy controller of speed, using the TS method, and the neural estimator of the electromagnetic torque, using the LMS algorithm technique, made possible the obtaining of satisfactory performance of the dynamic functioning of the motor.

An important contribution of this work is the specification of the rotational speed of the rotor of a three-phase induction motor from the information of the signal of the estimated electromagnetic torque, using intelligent control techniques.

As perspective of future work, it is planned to carry out experimental tests in a milling machine, with the feedrate specified in real time from the machining of each material.

References

[1] C.A.F.C. Alves, Study of plasma nitriding applied to milling tools, M.Sc. Dissertation, Federal University of Rio Grande do Sul, 2002.

[2] L.M. Yue, F.H. Ya, L. Yuan, H.Z. Yu, An intelligent controller based on constant cutting force for 5-axis milling, in: International Conference on Information Technology and Computer Science, Ukraine, 2009, pp. 237-241.

[3] J.A.T. Altuna, Implementation of the direct method of vector control of an induction motor with stator flux orientation using DSP, M.Sc. Dissertation, State University of Campinas, 1997.

[4] L.A. Mozelli, Fuzzy control for takagi-sugeno systems: Improved conditions and applications, M.Sc. Dissertation, Federal University of Minas Gerais, 2008.

[5] T. Takagi, M. Sugeno, Fuzzy identification of systems and its application to modelling and control, IEEE Transactions on Systems, Man and Cybernetics 1 (1985) 116-132.

[6] I.S. Shaw, M.G. Simões, Fuzzy Control and Modeling, Edgard Blucher Ltda Publisher, São Paulo, SP, Brazil, 2004.

[7] A. Nigrini, Neural Networks for Pattern Recognition, The MIT Press, San Diego, 1993.

[8] D.E. Rumelhart, J.L. Mcclelland, Parallel Distributed Processing: Explorations in the Microstructure of Cognition, The MIT Press, San Diego, 1986.

[9] L.C. Leite, Identification of the conjugate of a sectorial induction machine by artificial neural networks, Ph.D. Thesis, State University of Campinas, 2003.

[10] X. Lin, A. Li, W. Zhang, Learning fuzzy logic based intelligent determination of feedrate for end milling operation, in: 6th International Conference on Intelligent Systems Design and Applications, China, 2006.

[11] P.B. Severino, A study of estimation of flux and conjugate in three-phase induction motors-implementation using DSP, M.Sc. Dissertation, Federal University of Uberlândia, 2005.

[12] C.E. Milhor, Proposal of a Takagi-Sugeno fuzzy controller with H_∞ performance for regulation of idling in otto cycle engines, Ph.D. Thesis, University of São Paulo, 2008.

Journal of Mechanics Engineering and Automation 4 (2014) 521-527

Dynamic Control of a Flexible Shaft Mounted in Adaptive or Active Bearing

Olivier Bonneau, Mihai Arghir and Pascal Jolly

Institut Pprime UPR 3346 CNRS, Université de Poitiers, BP 30179, France

Received: March 18, 2014 / Accepted: April 04, 2014 / Published: June 25, 2014.

Abstract: The dynamic behavior of rotors is highly influenced by bearing characteristics. In previous works, the authors have shown that it may be beneficial to adapt the bearing behavior to the shaft behavior. Several adaptive and active components will be developed in this paper in order to control the shaft dynamical amplitude. Different models of hydrodynamic bearings behavior are described. The Reynolds equation resolution may be done by numerical or analytical solutions. A physical analysis of the equation of thin films will identify the most sensitive parameters. The shaft flexibility is taking into account by a modal approach. The fluid-structure coupling process is a simulation, step by step, of the rotor behavior. At each step, the nonlinear fluid force is numerically calculated to obtain the unbalanced shaft response. The results, presented in this paper, concern the dynamic response of unbalanced shaft mounted in adaptive or active bearings: bearings with variable clearance, variable viscosity or variable housing speed. It is shown that the fluid bearing parameters must be adapted to the rotor speed (in particular near or far a critical speed). Then, the paper presents a new kind of active bearing. It works with a mechanical control of the housing position. Several parameters are tested and compared. The robustness of the dynamic control parameters is presented. In conclusion, the bearing adaptation could be very useful to control the shaft dynamic. This limits the effect of the critical speed, in particular by diminishing the shaft amplitude and the dynamic forces transmitted to the housing.

Key words: Lubrication, rotor dynamics, adaptive and active journal bearings.

1. Introduction

The dynamic behavior of high-speed rotors can be very complex to study, in particular when the speeds are close to the critical frequencies. The dynamical behavior of the fluid bearings has, in that case, an important effect. The design of bearings (i.e., the geometrical and functional parameters) must be chosen carefully. However, the ideal values of these parameters are often a function of the shaft speed. For a speed close to a rotor critical speed, the ideal bearing is not the same as that obtained for a speed far to a critical frequency.

The idea is then to adapt the bearing to the speed.

Some studies present two kinds of adaptive bearings: with a variable clearance [1, 2] or with a variable viscosity [3-6]. The next level of analysis is the design of a real active bearing. Some authors have studied bearings mounted in a piezoelectric active housing [7, 8]. This solution is elegant but expensive.

We want to develop here an original solution based on a mechanical control of two eccentrics. Two brushless motors are used to control the eccentricity and the phase shift of the bearing position. It is more a pedagogical device than an industrial product.

The paper is organized as follows: Section 2 describes the bearing models (Reynolds equation); Section 3 presents the rotor finite element and the modal approach; Section 4 presents the fluid-structure coupling. It is a step by step resolution of Reynolds equation and shaft equations; Section 5 exposes and discusses results obtained with an adaptive bearing; Section 6 exposes a new active bearing model; and

Corresponding author: Olivier Bonneau, professor, research fields: tribology, lubrication, rotor dynamic behavior and mechanical design. E-mail: Olivier.bonneau@univ-poitiers.fr.

finally Section 7 discusses the results obtained with this active bearing (interest of this kind of design, influence of the amplitude and of the phase of the signal control).

2. Bearing Model

In this study, two kinds of bearings will be used: Active ball bearing and hydrodynamic fluid bearing. The ball bearing behavior is considered as linear and it will be modeled with stiffness.

The hydrodynamic bearing behavior is nonlinear and it is modeled by the Reynolds equation [9] write in the cylindrical reference (R, θ, z):

$$\frac{1}{R^2}\frac{\partial}{\partial\theta}\left[\frac{h^3}{\mu k_x}\frac{\partial P}{\partial\theta}\right]+\frac{1}{\partial z}\left[\frac{h^3}{\mu k_z}\frac{\partial P}{\partial z}\ 0\right]=$$

$$\frac{(\omega_{\text{housing}}+\omega_{\text{shaft}})}{2}\frac{\mathrm{d}h}{\mathrm{d}\theta}+\dot{x}\cos\theta\ +\ \dot{y}sin\theta \qquad (1)$$

where,

R: the radius

h: local thickness

μ: fluid viscosity

k_x and k_z coefficients depending of the Reynolds number (to take into account turbulent effects), $\omega_{housing}$ and ω_{shaft} rotation speeds. Fig. 1 describes the x and y cartesian positions of the rotor in the housing.

This equation can be solved (to obtain the pressure field and then the fluid film forces) using finite differences or by an analytic method (for example, the short bearing theory) [10].

3. Shaft Model

The rotor is modeled with typical beam finite elements including the gyroscopic effects.

Each element in Fig. 2 has four degrees of freedom: two translations in the radial directions x and y, and two axes of rotations (x and y).

According to the fundamental principle of mechanic [10, 11], the differential system (with $\{\delta\}$ the node displacement vector) is the following :

$$[M]\left\{\ddot{\delta}\right\}+[C]\left\{\dot{\delta}\right\}+[K]\{\delta\}=\{F_{unb}\}+\{F_{nl}\}+\{F_{gr}\} \qquad (2)$$

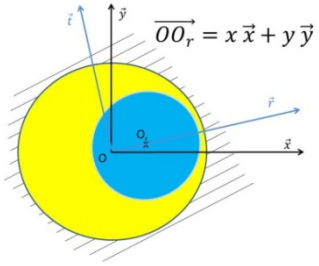

Fig. 1 Fluid film.

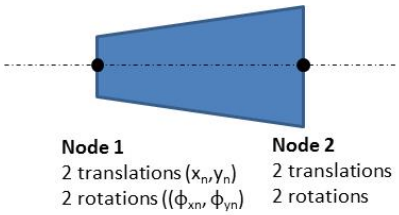

Fig. 2 Rotor element.

where,

[M]: mass matrix

[C]: damping and gyroscopic matrix

[K]: stiffness matrix

$\{F_{unb}\}$: unbalance forces

$\{\mathrm{F_{nl}}\}$: non linear bearing forces

$\{F_{gr}\}$: gravity forces.

This system has $4n$ degrees of freedom (n is the number of nodes). To reduce the degrees of freedom, a modal approach is used [9, 12, 13] with a change of variable: $\{\delta\} \geq \{q\} \geq \{\delta\} = [\psi]\{q\}$ with $[\psi]$ the matrix obtained with the eight first modal vectors. $\{\psi_i\}$ and $\{\mathrm{q}\}$: the modal vector of displacement.

Then, the differential equation is transformed:

$$[m]\{\ddot{q}\}+[c]\{\dot{q}\}+[k]\{q\}=\{f_{ext}\} \qquad (3)$$

with $\{q\}$ modal vector, [m], [c] and [k] modal matrices of mass, damping and stiffness. Now, the degrees of freedom were reduced to eight. For the rotor treated here, eight modes are enough to obtain an acceptable precision (the eighth frequency is 40,440 rpm for a maximum rotor speed of 6,000 rpm).

4. Dynamic Model

A nonlinear analysis of an unbalanced shaft mounted at one end in a ball bearing and at the other

end on an adaptive bearing is conducted in Fig. 3. It is a step by step resolution [10] of the coupled equations in modal basis: dynamic equation of the shaft Eq. (3) and fluid film bearing equation Eq. (1). The flow chart is as follows:

(a) beginning with initial values of modal positions and velocities;

(b) calculus of external modal forces (unbalance, weight. etc.);

(c) calculus of real displacements and velocities in bearings (by modal basis change);

(d) non linear bearings forces calculus (in the real basis);

(e) computation of all forces in the modal basis (by modal basis change);

(f) modal accelerations computation;

(g) time integration (by variable step Euler method);

(h) shaft speed is incremented;

(i) the process begins in b.

The general idea is to control the bearing behavior, because it can have a strong influence on the dynamic behavior of the rotor: The fluid forces in Eq. (3) are function of:

- geometrical parameters: length (l), bearing radius (R), radial clearance (C), fluid film thickness ($h(\theta, z)$).
- kinematic parameters: shaft speed (ω_{shaft}), housing speed ($\omega_{housing}$) which is very often nil.
- fluid parameters: viscosity (μ), pressure feed (P_{feed}).

5. Results

The shaft of the Bently rotor kit [14] will be used in this study. The length is 0.46 m, the rotor diameter is 10 mm, with one disc (0.9 kg) in the middle. It is guided by a bearing at one end and by a bearing adaptive to the other end.

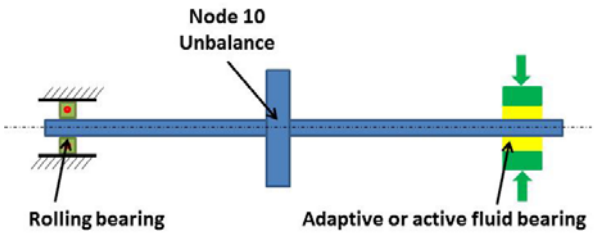

Fig. 3 Unbalanced flexible shaft.

The modes and frequencies are presented in Fig. 4.

We present three studies which show the influence on the rotor behavior of variable radial clearance, of the viscosity and of the housing speed. The dynamic force is an unbalanced force located on the middle of the rotor (Node 10). All the amplitudes are undimensioned by 0.2 mm which corresponds to the radial clearance.

5.1 Influence of Radial Clearance

Murthy [1] and then Mu et al. [2] have studied a squeeze film damper with variable clearance. In general, a conical design is proposed. Fig. 5 presents a scheme of this kind of fluid bearing.

The clearance is adapted to the shaft speed by an axial position.

Fig. 6 shows the response at the Node 10 (unbalanced position) during an increase of the shaft speed and for two values of the bearing clearance 0.2 mm and 0.4 mm).

Shaft amplitude is undimensioned by the value of 0.2 mm (the smallest bearing clearance). The shaft has a resonance frequency (first mode) near 2,220 rpm.

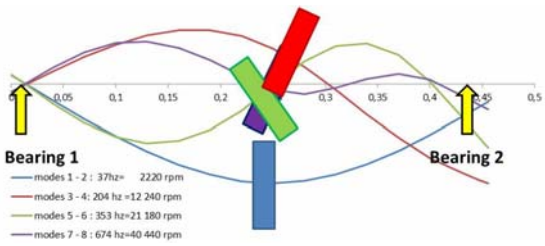

Fig. 4 Rotor modes.

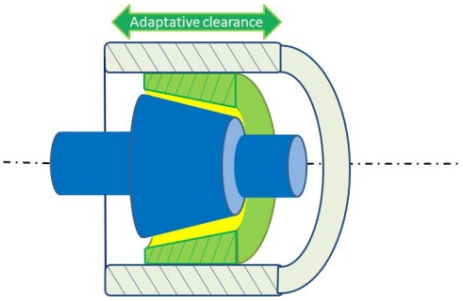

Fig. 5 Adaptive radial clearance.

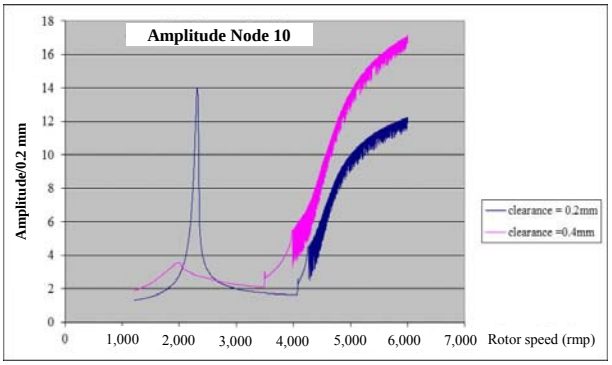

Fig. 6 Dimensionless amplitude versus rotational speed.

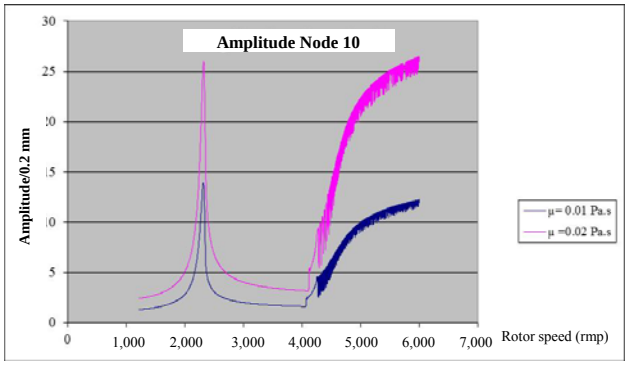

Fig. 7 Dimensionless amplitude versus rotational speed.

Then, near 4,000 rpm, the instability of the bearing creates very important amplitude. It is imperative to avoid in this area. This classical bearing instability (whirl) appears when the shaft speed is close to twice the critical speed: the bearing generates a half frequency whirl which excites the critical frequency of the rotor.

It appears that the clearance of the fluid bearing has a very important effect on the amplitude of the shaft. Fig. 6 shows that when the speed is very different to the critical speed, it is better to have a small clearance (to limit bearing amplitude) and it is better to have a large clearance near the critical speed. It is then possible to adapt the clearance at the rotor speed (large clearance near the first critical speed and small clearance when the speed is far from it). We have shown [9] the same kind of results obtained with a squeeze film damper.

5.2 Influence of the Viscosity

It is possible, in the same way, of showing the influence of the viscosity [9]. Fig. 7 presents the amplitude of the Node 10 during an increase in the rotor speed.

Two viscosities have been used.

Some technological solutions for bearings with varying viscosity have been designed [3-6]. The dynamical results are close to results obtained with variable clearance; these simulations show that it could be possible to monitor the damping of the fluid bearing.

5.3 Influence of the Housing Speed

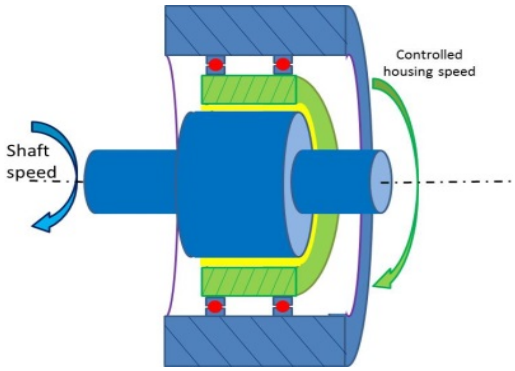

Fig. 8 Controlled housing speed.

The influence of the housing speed could be analyzed.

It is possible to avoid, by this speed control Fig. 8 the whirl effect. If the housing rotates with a speed opposite to that of the shaft, the behavior of the bearing is close to that of a SFD (squeeze film damper): $(\omega_{housing} + \omega_{shaft}) = 0$. This solution allows starting up a machine: the housing speed creates the hydrodynamic effect. But this bearing design is complex and expensive.

6. Active Bearing

All the previous controlled designs have been developed with an adaptive bearing: adapt a bearing parameter to optimize the behavior for each speed of rotation. This has some limits and we present now the use of an active bearing.

The idea is to control, by a mobile bearing, the amplitude of the unbalanced rotor. Some studies [13, 14] show results obtained with bearing mounted in piezoelectric actuators. The new design presented

here is very simple. The bearing is supported by a dynamic housing controlled by two brushless motors.

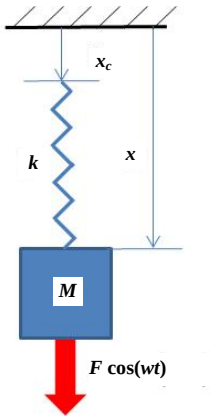

Fig. 9 One degree of freedom model.

Fig. 9 presents, in one dimension, the general idea. On this simple model, a mass is suspended from a spring. The spring (stiffness k) is mounted in a controlled support (x_c is the controlled parameter). Equation obtained with the fundamental principle of mechanic applied to the mass is:

$$m\ddot{x} + k(x - x_c) = F\cos(\omega t)$$

Then if x_c is controlled with an amplitude equal to $x_c = -\frac{F\cos(\omega t)}{k}$, the dynamic perturbation is annulled $\geq m\ddot{x} + kx = k\,x_c + F\cos(\omega t) = 0$.

We have designed the "active bearing" on this principle. Two degrees of freedom are controlled, with the objective to decrease the dynamic amplitudes.

Fig. 10 presents this new design; the rotor is mounted in one end on a ball bearing and on the other end: either in an "active ball bearing", either in an active fluid bearing. This "active bearing" is guided in two eccentrics 2 and 3. The speed of the shaft 10 is controlled by the motor M_1.

The bearing supporting the shaft is turning with a variable eccentricity e_v (Fig. 11) controlled by the angle difference θ_v between 3 and 2 (angular position of the motor three relative to the motor 2). Then the speed of rotation of 3 (ω_{30}) and 2 (ω_{20}) must be the same and equal to (ω_{10}).

Variable eccentricity and the frequency (and phase) are function of the shaft speed (ω_{10}):

- during an increase of the shaft speed e_v is adapted for each speed value;

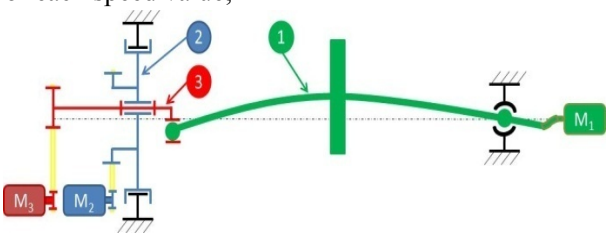

Fig. 10 Active bearing design.

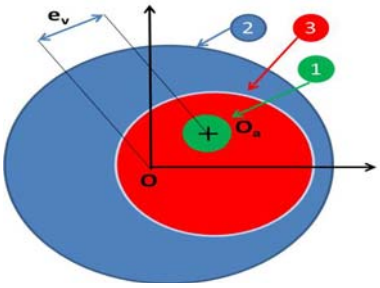

Fig. 11 Controlled amplitude design.

$\omega_{20} = \omega_{30}$ are equal to ω_{10} (in case of an unbalanced force).

7. Results

These numerical results are obtained for the flexible shaft described in Fig. 4.

Several configurations will be tested. In particular, the "robustness" of the process will be studied: i.e., the influence of the regulation parameters (e_v, θ_v) on the dynamic response.

All results are obtained with an increase in speed from 1,000 rpm to 4,000 rpm to 240 s. The unbalance is 0.1 10-3 m·kg.

7.1 Fluid Bearing Versus Ball Bearing without Control

We first compare the response of the system with a fluid bearing and with a ball bearing. The ball bearing is modeled by a constant stiffness.

Fig. 12 (amplitude function of the rotation speed) compares the amplitude (Node 10 = middle of the shaft) between the two design. At the critical frequency the damping provided by the fluid bearing reduces the

non-dimensional amplitudes from 25 to 14.

7.2 Optimal Control

In order to demonstrate the interest of the active support: it provides "dynamic damping", we have chosen to design the bearing without natural damping: now, all the results are obtained with a controlled ball bearing.

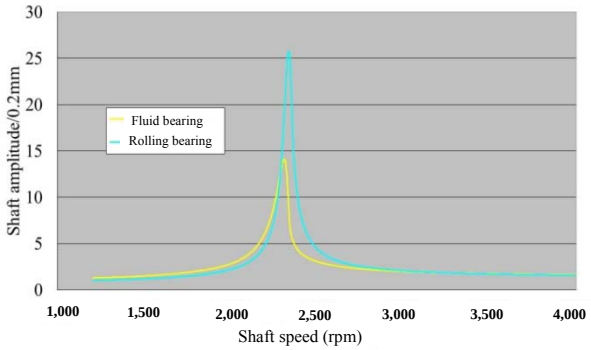

Fig. 12 Shaft amplitude for fluid and ball bearing.

The control parameters (e_v, θ_v) are calculated in advance to find the optimal values. In a real case, they will be determined by a real control: a PID regulate the process with a measure of the dynamical amplitude of the shaft.

Fig. 13 presents the amplitude of the unbalanced shaft for uncontrolled and for controlled rotor (with 3 e_v values). It is clear that the process is very useful. The optimal e_v is 0.15 mm and optimal phase very close to 0º. The amplitude of the unbalanced force at the first critical speed (2,200 rpm) is about 5 N.

7.3 Influence of e_v

Fig. 13 exposes the influence of the variable eccentricity. The optimal value is 0.15 mm. If the e_v value is more important (0.2 mm) or less (0.1 mm), the control is less efficient.

Fig. 14 exposes four trajectories of the unbalance shaft (Node 10). These trajectories are obtained for 2,280 rpm (close to the critical speed). The benefit of the control is clear. The active bearing movement compensates unbalanced forces.

7.4 Influence of the Phase θ_v

The choose of the optimal phase, between the angular position of the shaft (i.e., unbalanced position) and the controlled bearing, is very important. In this application, the optimal phase is close to 0º, this is due to the absence of damping. We present in Fig. 15 four trajectories obtained:

- without control;
- with optimal control values;
- with two bad phases (45º and 90º).

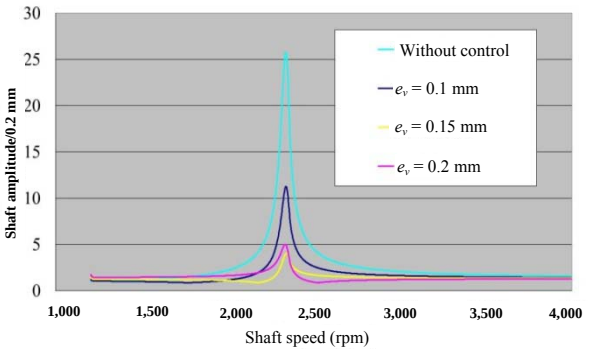

Fig. 13 Shaft amplitude with control.

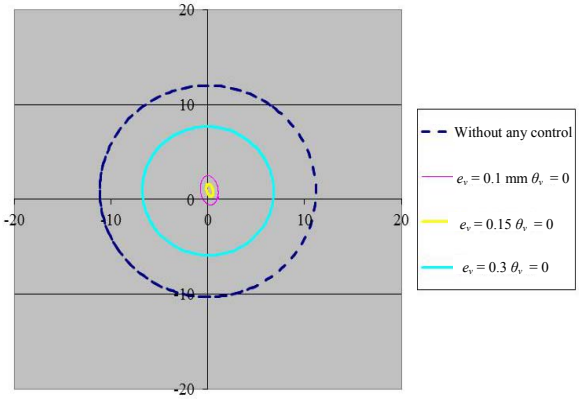

Fig. 14 Trajectories of the shaft (Node 10).

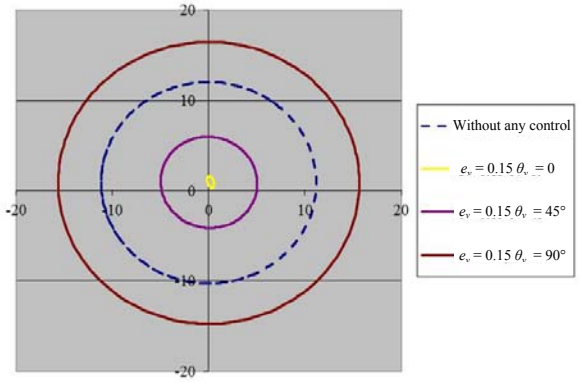

Fig. 15 Trajectories for 2,280 rpm.

It may be noted that even with a significant error

(45°) the reduction of the amplitude is always sensitive.

The results presented in Fig. 16 are clearer. The amplitude of the rotor at a speed of 2,280 rev/min depends on the phase. The decreasing amplitude is relatively constant around the optimum position.

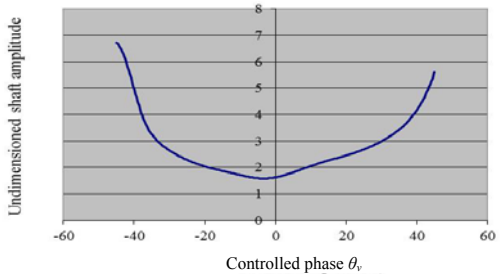

Fig. 16 Shaft amplitude (2,280 rpm) versus controlled shaft (e_v = 0.15).

8. Conclusions

The numerical study presented in this paper highlights the significant gain obtained by an active control of a bearing.

The general idea is to develop a simple mechanism which is more educational than industrial.

The dynamic control of the position of the bearing can greatly reduce the amplitudes due to an unbalance of the shaft. The influence of the main parameters could be quantified. An experimental device must now be developed.

Reference

[1] T.S.R. Murthy, Analysis of multi-scallop self-adjusting conical hydrodynamic bearings for high precision spindles, Tribol. Int. 14 (3) (1981) 147-150.

[2] C. Mu, J. Darling, C.R. Burrows, An appraisal of a proposed active squeeze film damper, J. Tribol. 113 (4) (1991) 750-754.

[3] A. Bouzidane, M. Thomas, An electrorheological hydrostatic journal bearing for controlling rotor vibration, Comput. Struct. 86 (3-5) (2008) 463-472.

[4] D.A. Bompos, P.G. Nikolakopoulos, CFD simulation of magnetorheological fluid journal bearings, Simul. Model. Pr. Theory 19 (4) (2011) 1035-1060.

[5] B. Pecheux, O. Bonneau, J. Frêne, Investigation about electrorheological squeeze film damper applied to active control of rotor dynamic, Int. J. Rotating Mach. 3 (1) (1997) 53-60.

[6] P.G. Nikolakopoulos, C.A. Papadopoulos, Controllable high speed journal bearings, lubricated with electro-rheological fluids: An analytical and experimental approach, Tribol. Int. 31 (5) (1998) 225-234.

[7] J. Tůma, J. Šimek, J. Škuta, J. Los, Active vibrations control of journal bearings with the use of piezoactuators, Mech. Syst. Signal Process. 36 (2) (2013) 618-629.

[8] Z. Abduljabbar, M.M. ElMadany, A.A. AlAbdulwahab, Active vibration control of a flexible rotor, Comput. Struct. 58 (3) (1996) 499-511.

[9] O. Bonneau, J. Frêne, Non-linear behavior of a flexible shaft partly supported by a squeeze film damper, Wear 206 (1-2) (1997) 244-250.

[10] O. Bonneau, Static and dynamic behavior of rotor supported by fluid bearings: Influence of the bearings, Ph.D. Thesis, University of Poitiers, 1989.

[11] M. Lalanne, Rotordynamics Prediction in Engineering, 2nd ed., Chichester; John Wiley & Sons, Inc., New York, 1998.

[12] J. Frene, O. Bonneau, Dynamic behaviour of elastic shaft supported by hydrodynamic bearings, Tribology Series 39 (2001) 3-13.

[13] O. Bonneau, S. Berger, J. Frêne, Dynamic behavior of bearings and thrust bearing with geometrical defects, Mech. Ind. 5 (01) (2004) 41-47.

[14] A. Muszyńska, Rotordynamics, Taylor & Francis, Boca Raton, 2005.

Journal of Mechanics Engineering and Automation 4 (2014) 528-532

Influence of Testing Temperature on the Corrosion Behavior of API 5L X70 Pipeline Steel

Carlos Antonio Vieira de Almeida Machado[1], Renato Altobelli Antunes[1], Elisabete Jorge Pessine[2] and Olandir Vercino Correa[2]

1. Centro de Engenharia, Modelagem e Ciências Sociais Aplicadas (CECS),Universidade Federal do ABC, Santo André 09210-580, Brazil

2. Centro de Ciência e Tecnologia de Materiais (CCTM), Instituto de Pesquisas Energéticas e Nucleares(IPEN/CNEN-SP), Cidade Universitária, São Paulo 05508-000, Brazil

Received: March 11, 2014 / Accepted: April 01, 2014 / Published: June 25, 2014.

Abstract: It is known that localized corrosion attack takes a preponderant role in the onset of stress corrosion cracking of pipeline steels in high pH conditions. Carbonate/bicarbonate solutions can be employed to study the localized corrosion behavior of these materials. In addition to the presence of chloride ions in the electrolyte, the solution temperature is also of prime importance to the onset of pitting corrosion. The aim of this work is to evaluate the influence of the testing temperature on the corrosion behavior of the API 5L X70 pipeline steel which is a standard material for gas pipelines in Brazil. Samples were exposed to a solution consisting of Na_2CO_3, $NaHCO_3$ and NaCl at three different temperatures: RT (room temperature), 40 ºC and 60 ºC. The corrosion morphology was observed using SEM (scanning electron microscopy). The results showed that pitting corrosion became facilitated when the steel was immersed at higher temperatures.

Key words: API 50 X70, pipeline steel, corrosion, temperature.

1. Introduction

API 5L X70 is a pipeline steel currently used in Brazil to transportation of natural gas and oil. This type of structure is designed to ensure that failures resulting from high pressure, thermal effects and environmental degradation are prevented [1]. Most parts of oil and gas sources in the world are located in remote areas and demand transportation by pipelines in order to reach their major markets [2]. The environments where these pipelines are installed are considered aggressive to the API steels due to the presence of species such as Cl^-, NCO_3^-, CO_2 and H_2S [3]. SCC (stress corrosion cracking) is a serious threat to the safe operation of pipeline steels [4]. Several authors studied the SCC mechanisms of pipeline steels in different environments [5, 6]. Most failures due to SCC of API steels are reported to occur under a high pH (approximately 9.5) condition which is associated with a concentrated solution consisting of carbonate/bicarbonate [7, 8]. A passive oxide layer can develop when the steel is exposed to this condition [9]. Chloride ions are reported to lead to the breakdown of the passive layer, forming corrosion pits. Pitting corrosion is considered as the first step of the SCC mechanism of pipeline steels [10]. In this context, it is imperative to investigate the pitting corrosion behavior of pipeline steels in order to guarantee a safer operation. Few works have been devoted to study the effect of temperature on the pitting corrosion resistance of pipeline steels. Nazari et al. [11] showed that the nature of the oxide layer formed on the surface of the X70 pipeline steel was strongly affected by the testing temperature. The aim of this work is to investigate the effect of the test temperature on the corrosion behavior

Corresponding author: Renato Altobelli Antunes, materials engineer, Ph.D., research fields: corrosion science and protective coatings. E-mail: renato.antunes@ufabc.edu.br.

of the API 5L X70 steel immersed in carbonate/bicarbonate solutions with addition of NaCl. The electrochemical evaluation was performed based on electrochemical impedance spectroscopy measurements and potentiodynamic polarization curves. The onset of pitting corrosion at different testing temperatures was assessed. This paper is organized as follows: Section 2 describes the experimental procedure; Section 3 presents results and discussion; and Section 4 gives conclusions.

2. Experimental Details

2.1. Material

The material used in this work was a hot rolled API 5L X70 steel plate kindly provided by USIMINAS whose chemical composition is shown in Table 1.

2.2 Electrochemical Tests

The electrochemical tests were performed in an electrolyte which was comprised of 0.05 M Na_2CO_3, 0.1 M $NaHCO_3$ and 0.1 M NaCl at three different temperatures: 40 ºC and 60 ºC. The specimens were cut in rectangular dimensions, leaving an approximate area of 1 cm^2 to be exposed to the electrolyte. All the electrochemical measurements were carried out using a potentiostat/galvanostat Autolab PGSTAT 100 equipped with a FRA module. A three-electrode cell arrangement was used, containing a Pt wire as the auxiliary electrode and a SCE (saturated calomel electrode) as reference; all potentials quoted in this paper are referred to this reference electrode. The specimen acting as working electrode was mounted in epoxy resin. The working electrode was ground with successive grade silicon carbide sandpaper up to 1,000 grit, polished with alumina paste (1 μm), degreased with ethanol, rinsed with distilled water and dried in air.

EIS (electrochemical impedance spectroscopy) measurements were used to monitor the electrochemical behavior of the specimens during seven days of immersion. The data were collected under the OCP (open circuit potential) over a frequency range from 100 kHz to 10 mHz with an acquisition of 10 points/decade. The amplitude of the perturbation signal was ±10 mV. Potentiodynamic polarization curves were obtained after seven days of immersion using a scan rate of 1 $mV \cdot s^{-1}$ in the potential range from -300 mV vs. the OCP up to 1 V.

Table 1 Results from traditional acquisition.

Element	Mass (%)
C	0.12
Mn	1.490
S	0.006
P	0.018
V	0.020
Nb	0.017
Al	0.014
Fe	Bal.

2.3 Corrosion Morphology

The corrosion morphology of the tested specimens, emphasizing the presence of pits, was assessed using SEM (scanning electron microscopy) (Hitachi TM3000 tabletop).

3. Results and Discussion

3.1 EIS Measurements

EIS results are represented as Nyquist plots as shown in Fig. 1. The plots are referred to seven days of immersion in the electrolyte at different testing temperatures. Electrochemical AC techniques such as EIS have a low amplitude perturbation signal, making it attractive to study the corrosion processes of electrical conductors in aqueous electrolytes [12]. EIS is a powerful tool for investigating the mechanisms of electrochemical reactions. The Nyquist plots are characterized by a depressed semicircle spanning throughout the whole frequency range independently of the testing temperature. The highest frequencies are on the left whereas the lowest frequencies are on the right of the plots shown in Fig. 1. At a first glance, this indicates that the corrosion mechanism should be the same for the three different temperature conditions. In

fact, Zhang et al. [13] stated that the capacitive semicircle which characterizes the Nyquist plots shown in Fig. 1 is typical of activation-controlled interfacial reactions.

In this regard, diffusion-controlled processes throughout the oxide layer formed on the surface of the specimen during immersion can be neglected. In spite of the similarity akin to the corrosion mechanisms suggested by the Nyquist plots, it is important to observe the relative impedance values obtained at each condition and, most importantly, the radius of the capacitive loops. It is well-known from the literature, that this radius is closely related to the corrosion resistance of the electrode surface [14]. Thus, the results suggest that the corrosion resistance was little affected when the testing temperature was raised from the RT to 40 ºC. However, by further increasing the temperature to 60 ºC the radius of the semicircle was greatly depressed, indicating a significant loss of corrosion resistance. Recent studies by Tang et al. [15] and Xiang et al. [16] confirm that temperature seriously affects the corrosion rate of pipeline steels. The electrochemical reactions leading to reaction are favored at temperatures up to 70 ºC or 90 ºC, accelerating corrosion. For higher temperatures, the corrosion rate can be depressed due to the formation of more protective oxide films. The results shown in Fig. 1 confirm the trend of increased corrosion kinetics for the temperatures evaluated in this work.

3.2 Potentiodynamic Polarization Curves

Potentiodynamic polarization curves of the API 5L X70 steel immersed for seven days at different temperatures in the electrolyte solution described in Section 2.2 are shown in Fig. 2. The electrochemical parameters determined from these curves are presented in Table 2. Corrosion potential (E_{corr}), corrosion current density (I_{corr}) and breakdown potential (E_b) are reported.

The curves shown in Fig. 2 present a well-defined passive region independently of the testing temperature.

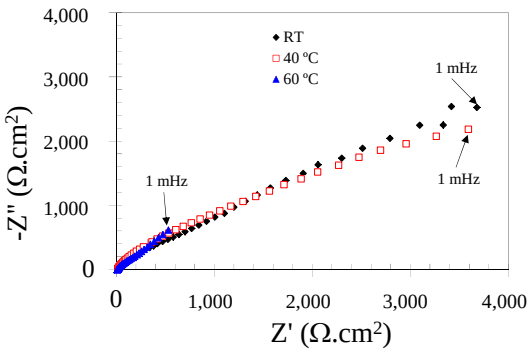

Fig. 1 Nyquist plots of the API 5l X70 steel immersion for 7 days at different testing temperatures.

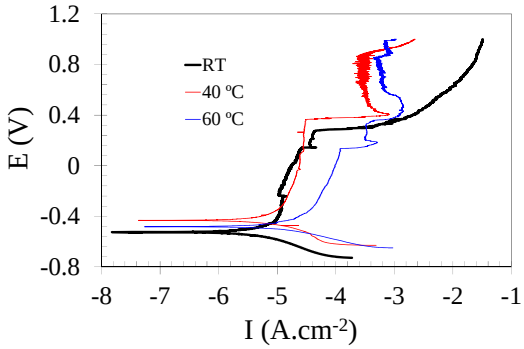

Fig. 2 Potentiodynamic polarization curves of the API 5L X70 steel immersed for seven days at different temperatures in the electrolyte solution described in Section 2.2.

Table 2 Electrochemical parameters determined from the potentiodynamic polarization curves shown in Fig. 2.

Temperature	E_{corr} (mV)	I_{corr} (μA·cm^{-2})	E_b (mV)	Passive range (mV)
RT	-0.53	2.18	0.27	0.80
40 ºC	-0.43	4.17	0.38	0.81
60 ºC	-0.51	11.7	0.11	0.62

The onset of pitting corrosion is evident from the sharp increase of the current density at the breakdown potentials (E_b). In spite of the similarities between the curves especially in respect to the presence of a passive region, remarkable differences can be observed depending on the testing temperature. The passive currents for the room temperature condition are slightly lower than at 40 ºC up to the breakdown potential as well as the value of I_{corr}, suggesting that the corrosion resistance of the API steel is higher at the lowest testing temperature. Nevertheless, the passive range is very similar for these conditions and the current densities

associated with the specimens tested at 40 ºC are also small, indicating that the corrosion properties of the API 5L X70 steel was little affected when the temperature was raised up to this level. This is in agreement with the EIS measurements as inferred from the Nyquist plots shown in Fig. 1.

For the tests performed at 60 ºC, though, there was an evident reduction of the corrosion resistance. The onset of pitting corrosion occurred at a breakdown potential of only 0.11 V and the passive range was shortened to 0.62 V. Thus, it is possible to affirm that the API 5L X70 steel became more prone to localized corrosion attack when the temperature reached 60 ºC. Furthermore, the corrosion current density was almost three times higher at 60 ºC when compared to that determined at 40 ºC and more than five times higher than that obtained at the room temperature. This result points to an overall higher corrosion rate of the specimens tested at 60 ºC.

3.3 Corrosion Morphology

According to Ref. [10], SCC of pipeline steels can be initiated in the bottom of a pit. The initial pitting mechanism is related to corrosion at metallurgical heterogeneities such as grain boundaries, non-metallic inclusions and interfaces between different phases. As observed in the potentiodynamic polarization curves shown in Fig. 2, the onset of pitting corrosion has been observed for the API 5L X70 steel independently of the testing temperature. Moreover, the resistance to pitting corrosion was found to decrease at 60 ºC. Hence, the propensity to SCC should accompany this temperature dependence. In order to share more light on this subject, the corrosion morphology of the steels was evaluated using SEM (Fig. 3).

The micrograph shown in Fig. 3a corresponds to the surface of a specimen tested at room temperature after potentiodynamic polarization. Fig. 3b shows the same region at a higher magnification. The specimens tested at higher temperatures presented similar corrosion morphology but with increasing number of pits,

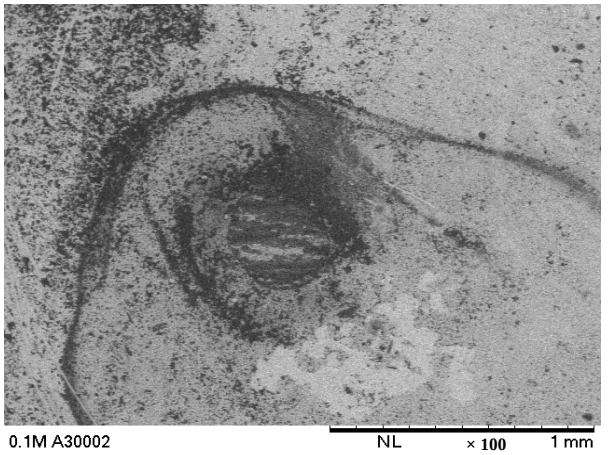

(a)

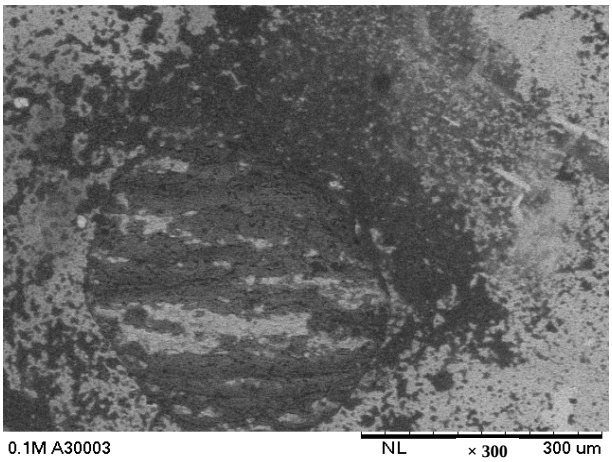

(b)

Fig. 3 SEM micrograph showing the presence of one shallow pit after potentiodynamic polarization of the API 5L X70 steel at room temperature. The micrograph on the right is referred to the same region on the left at a higher magnification.

especially those tested at 60 ºC. Shallow pits were observed. Van Boven et al. [10] showed that cracks originate from shallow pits during SCC of the X65 pipeline steel in simulated soil solution. In this regard, the results obtained in the present work point toward a dangerous corrosion activity of the X70 pipeline steel at 60 ºC. Even at RT, the presence of shallow pits is also observed.

4. Conclusions

The influence of the testing temperature on the corrosion behavior of the API 5L X70 pipeline steel in 0.05 M Na_2CO_3, 0.1 M $NaHCO_3$ and 0.1 M NaCl

solution has been evaluated. The results showed that the steel was prone to pitting corrosion even at room temperature. When the temperature was raised to 40 ºC the corrosion properties were little affected. Nevertheless, for the tests performed at 60 ºC, there was a marked decrease of the corrosion resistance, in respect to either the overall corrosion rate expressed as the corrosion current density or the pitting corrosion resistance. In this context, based on the well-established relationship between the formation of pits and SCC of pipeline steels, the results reveal a more dangerous situation for the initiation of SCC at 60 ºC. Notwithstanding, pits have also been observed at lower temperatures.

Acknowledgments

Usiminas is acknowledged for kindly providing the API 5L X70 steel plate used in this work.

References

[1] F.J. Sánchez, B. Mishra, D.L. Olson, Magnetization effect on hydrogen absorption in high strength steels and its implications, Scripta Materialia 53 (2005) 1443-1448.

[2] S.H. Hashemi, Correction factors for safe performance of API X65 pipeline steel, International Journal of Pressure Vessels and Piping 86 (2009) 533-540.

[3] Z.Y. Liu, X.G. Li, C.W. Du, G.L. Zhai, Y.F. Cheng, Stress corrosion cracking behavior of X70 pile steel in an acidic soil environment, Corrosion Science 50 (2008) 2251-2257.

[4] Z. Liu, X. Li, Y. Zhang, C. Du, G. Zhai, Relationship between electrochemical characteristics and SCC of X70 pipeline steel in na acidic soil simulated solution, Acta Metallurgica Sinica 22 (2009) 58-64.

[5] A. Eslami, B Fang, R. Kania, B. Worthingham, J. Been, R. Eadie, et al., Stress corrosion cracking initiation under the disbanded coating of pipeline steel in near-neutral pH environment, Corrosion Science 52 (2010) 3750-3756.

[6] F.M. Song, Predicting the mechanisms and crack growth rates of pipelines undergoing stress corrosion cracking at high pH, Corrosion Science 51 (2009) 2657-2674.

[7] M.C. Li, Y.F. Cheng, Corrosion of the stressed pipe steel in carbonate-bicarbonate solution studied by scanning localized electrochemical impedance spectroscopy, Electrochimica Acta 53 (2008) 2831-2836.

[8] S. Tang, Y.F. Cheng, Localized dissolution electrochemistry at surface irregularities of pipeline steel, Applied Surface Science 254 (2008) 5199-5205.

[9] R.N. Parkins, S. Zhou, The stress corrosion cracking of C-Mn steel in CO_2-HCO_3-CO_3^{2-} solutions: I: Stress corrosion data, Corrosion Science 39 (1997) 159-173.

[10] G. van Boven, W. Chen, R. Rogge, The role of residual stress in neutral pH stress corrosion cracking of pipeline steels. Part I: pitting and cracking occurrence, Acta Materialia 55 (2007) 29-42.

[11] M.H. Nazari, S.R. Allahkaram, M.B. Kermani, The effects of temperature and pH on the characteristics of corrosion product in CO_2 corrosion of grade X70 steel, Materials and Design 31 (2010) 3559-3563.

[12] K. Jüttner, EIS (electrochemical impedance spectroscopy) of corrosion processes on inhomogeneous surfaces, Electrochimica Acta 35 (1990) 1501-1508.

[13] G.A. Zhang, Y.F. Cheng, Electrochemical corrosion of X65 pipe steel in oil/water emulsion, Corrosion Science 51 (2009) 901-907.

[14] R.A. Antunes, A.C.D. Rodas, N.B. Lima, O.Z. Higa, I. Costa, Study of the corrosion resistance and in vitro biocompatibility of PVD TiCN-coated AISI 316L stainless steel for orthopedic applications, Surface and Coatings Technology 205 (2010) 2074-2081.

[15] X. Tang, Y. Wu, Y. Yao, Z. Zhang, Effect of temperature and H2S concentration on corrosion of X52 pipeline steel in acidic solutions, Materials Science Forum 743-744 (2013) 589-596.

[16] Y. Xiang, Z. Wang, Z. Li, W.D. Ni, Effect of temperature on corrosion behavior of X70 steel in high pressure CO_2/SO_2/O_2/H_2O environments, Corrosion Engineering, Science and Technology 48 (2013) 121-129.

Journal of Mechanics Engineering and Automation 4 (2014) 533-541

A Study on the Levitation Control of the Multi-degrees-of-Freedom Rotational Machine Supported by Magnetic Bearings Using Flux Feedback

Jun-Ho Lee

Advanced Traction and Noncontact Feeding System Research Team, Korea Railroad Research Institute, Uiwang-City, Gyeonggi-do 437-757, Korea

Received: April 01, 2014 / Accepted: April 18, 2014 / Published: June 25, 2014.

Abstract: This paper deals with an open-loop characteristic of a magnetically levitated system including flux feedback. In order to design a controller to obtain a good disturbance rejection and to be insensitive to parameter variations, it might be useful to employ a flux feedback loop. The air gap flux which can be sensed by a proper sensor has linear relationship with respect to the change of the current and the air gap. This linear property decreases the inherent nonlinearity of the magnetic suspension system that is caused by the coupling between the electrical actuator and the mechanical plant. Simulation results achieved from a multi-degree-of-freedom numerical model show that the flux feedback loop makes an improvement of the performance of the magnetic suspension system against the load variations.

Key words: Flux feedback, magnetic bearings, levitation, rotational machine, multi-degrees-of-freedom.

1. Introduction

In recent trends to develop various technologies, the word “contactless” has been begun to receive notable attentions because of its effectiveness and maintenance free properties that are impossible to achieve in the conventional “contact” system. The typical representative contactless system is a magnetic suspension system which is commonly known as maglev (magnetically levitated) system. The first trial for the maglev has been performed at the University of Virginia in 1937 which has been intended to test magnetic bearing systems.

Recently, there are various applications employing the magnetic levitation configuration as a core technology, such as the magnetically levitated train system, the high speed turbo compressors, the flywheel energy storage system and the artificial heart pump.

Corresponding author: Jun-Ho Lee, Ph.D., research fields: design and control of flywheel energy storage system, design of wireless power transfer system. E-mail: jhlee77@krri.re.kr.

The magnetically levitated system can be divided into two parts based on the levitation method: one is a repulsive type using super conductors. One of disadvantages of this type of suspension system is that it needs to operate below the critical speed when the suspended object is stationary because an active suspension actuator and a controller are not included which make it possible to pass through the critical speeds; the other type is EMS (electromagnetic suspension system) using ferromagnetic or permanent magnet. The EMS type has one significant advantage in that it provides attraction force at zero speed, but such system is inherently unstable. In order to overcome the inherent instability, an active controller plays a very important role in the electromagnet type suspension system to make the stable suspension and maintain the suspended object within the nominal air gap.

Especially, when external disturbance or parameter variations affect on the active controller of the Maglev,

the system may cause a malfunction of the suspension system. In such case, a controller that has a robustness property should be introduced, or a system model should be considered to avoid the effects of the external disturbance or parameter variations [1-4].

In many papers and literatures, the design methodologies of the active magnetic suspension controllers have already been presented. Some advances in improving AMB (active magnetic bearing) feedback control using a nonlinear gap model instead of a linear gap model were proven in a SISO (single-output) balance beam test rig [5]. Hu et al. [6] developed a reduced power loss AMB in a balance beam by considering the constraint of voltage saturation as obtained for the class of sinusoidal force signals. Lindlau et al. [7] considered a feedback linearization voltage mode controller in an AMB balance beam using mu synthesis. Lin et al. [8] developed a model which treated coil resistance changes with structured uncertainty as well as considering actuator flux leakage. Nonlinear output regulation for a balance beam was carried out in a similar balance beam. Issues with a high speed energy storage flywheel AMB concerning modeling uncertainty and treatment using mu synthesis control were reported in Ref. [9].

However, the papers for the analysis of the open-loop characteristics of the magnetic suspension system have rarely presented. A significant paper on flux feedback control of AMBs used current control with both displacement and the deviation flux expressed as a linear combination of the total force in the AMB [10, 11]. At the equilibrium point, the total force in the AMB should be equal to the sum of the state feedback control effort and the estimated disturbance force. A linear flux observer was developed to reject a static and periodic disturbance force [10].

Sometimes, it is very valuable to make focus on the inherent properties of the magnetic suspension system to achieve a design of the improved active controller against the system parameter variations. The purpose of this paper is to show the effectiveness of the flux feedback loop of the air gap in the open loop characteristic of the magnetic suspension system when a constant voltage is applied to the electromagnet coils.

The paper is organized as follows: Section 2 summarizes the fundamental mathematical model (one-degree-of-freedom and four-degrees-of-freedom) of the EMS system, which does not include the flux feedback loop; Section 3 shows a modified mathematical model including the flux feedback loop. In the flux feedback loop, the estimated flux is linearly proportional to the magnetic excitation current and inversely proportional to the air gap; Section 4 presents that the magnetic suspension system including flux a loop has robustness against the parameter variations based on the simulation results; and Section 5 gives conclusions.

2. Fundamental Mathematical Model

2.1 One-Degree-of-Freedom

Fig. 1 shows a simple schematic diagram for EMS system which has the electromagnets as the suspension actuators.

The mathematical model of this system is divided into two parts: one is the plant (mechanical) dynamics and the other is the actuator dynamics. The plant

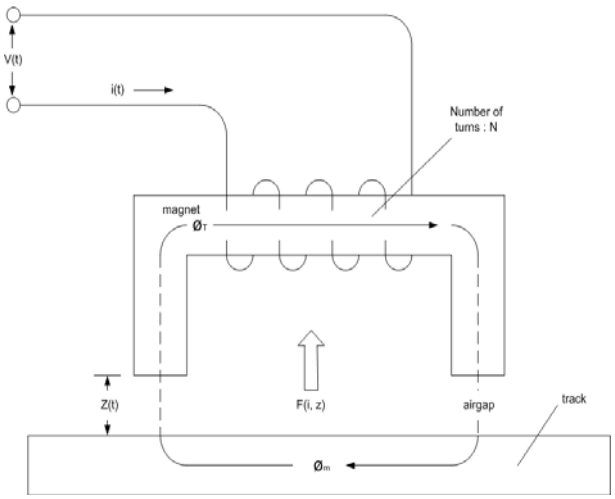

Fig. 1 Schematic diagram for EMS system.

(mechanical) dynamics is

$$m\ddot{z} = F(i,z) - mg - f_d \tag{1}$$

where, m is the total mass of the controlled object, g is the gravitational acceleration and f_d is the external disturbance force acting on the controlled object. In Eq. (1), $F(i, z)$ is the electromagnets attraction force which is proportional to the current deviation and inversely proportional to the air gap deviation, expressed such as:

$$F(i,z) = \frac{B^2 A}{\mu_0} = \frac{\mu_0 N^2 A}{4}\left(\frac{i(t)}{z(t)}\right)^2 \tag{2}$$

where, B is the flux density of the magnetic core material, A is the cross sectional area of the pole face of the electromagnet, μ_0 is the permeability in the air space and N is the number of turns. In order to drive Eq. (2), it is necessary to check the relation between the inductance and the magnetic flux density.

$$L(i,z) = \frac{N}{i}\varnothing_m = \frac{N}{i(t)}\frac{Ni(t)}{R_T} \tag{3}$$

where, $R_t = \frac{2z(t)}{\mu_0 A} = \frac{V_T}{\emptyset_m}$ is the reluctance of the magnetic circuit and V_T is the electromotive force. Normally the reluctance in the magnetic core is assumed to be negligible compared with the air gap, thus the coil inductance becomes

$$L(i,z) = \frac{\mu_0 N^2 A}{2z(t)} \tag{4}$$

$Li(t) = \text{NBA}$ and Eq. (4) yield the magnetic flux density such as:

$$B = \frac{Li(t)}{NA} = \frac{N^2 \mu_0 A i(t)}{2z(t) NA} = \frac{\mu_0 N i(t)}{2z(t)} \tag{5}$$

Substituting Eq. (5) into $F(i,z) = \frac{B^2 A}{\mu_0}$ yields Eq. (2). Eq. (2) has high nonlinearity and it is not easy to use Eq. (2) without doing the linear approximation with respect to the nominal point (i_0, z_0). For the linear approximation, the Taylor series expansion is usually employed. From the Taylor series expansion, Eq. (2) becomes

$$F(i,z) = k_i i(t) - k_z z(t) \tag{6}$$

where, $k_z = \frac{\mu_0 N^2 A i_0^2}{2z_0^3}$ and $k_i = \frac{\mu_0 N^2 A i_0}{2z_0^2}$ are the coefficients for the linear approximation of Eq. (2). k_z and k_i represent the displacement stiffness and the current stiffness, respectively.

In Eq. (6), the stiffness k_z has negative sign which means that once the attractive force of the electromagnets is activated, the controlled object is attracted until the electromagnets stop attracting the controlled object. This is one of the reasons why the electromagnet suspension system should have the active controller to control the air gap deviation.

The actuator dynamics is

$$\begin{aligned} v(t) &= Ri(t) + \frac{d}{dt}\left[L(i,z) i(t)\right] \\ &= Ri(t) + \frac{\mu_0 N^2 A}{2z(t)}\frac{d}{dt} i(t) - \frac{\mu_0 N^2 A i_0}{2z(t)^2}\frac{d}{dt} z(t) \end{aligned} \tag{7}$$

where, v is the coil voltage, R is the coil resistance, and $L(i, z)$ is the coil inductance which is the function of the air gap displacement. It should be noted that there is a variation of the inductance with respect to the air gap displacement in the second term, and that the third term denotes a voltage which varies with changes in the air gap $z(t)$ and its rate of change similar to back EMF voltage. By using Eqs. (1), (6) and (7), we can drive a state space equation such as:

$$\begin{bmatrix} \dot{z} \\ \ddot{z} \\ \dot{i} \end{bmatrix} = \begin{bmatrix} 0 & 1 & 0 \\ \frac{-k_z}{m} & 0 & \frac{k_i}{m} \\ 0 & \frac{k_z}{k_i} & \frac{-R}{L} \end{bmatrix} \begin{bmatrix} z \\ \dot{z} \\ i \end{bmatrix} + \begin{bmatrix} 0 \\ 0 \\ \frac{1}{L} \end{bmatrix} v + \begin{bmatrix} 0 \\ \frac{1}{m} \\ 0 \end{bmatrix} f_d \tag{8}$$

Fig. 2 shows the simple block diagram for the open-loop EMS system which does not include the flux feedback signal. The transfer function of the open loop system is induced by the Laplace transform of Eq. (8) for each state variables, which is

$$z(s) = \left[\frac{\frac{k_i}{mR}}{\left(1+\frac{L}{R}s\right)\left(s^2 + \frac{k_i}{mR\left(1+\frac{L}{R}s\right)}s - \frac{k_z}{m}\right)}\right] v(s) \tag{9}$$

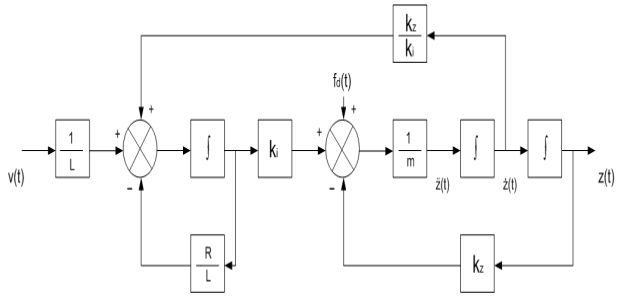

Fig. 2 Open-loop diagram without flux.

2.2 Four-Degrees-of-Freedom

Fig. 3 presents a rotational machine supported by the magnetic bearings which has four-degrees-of-freedom. For the rotational rotor, left and right electromagnetic bearings support the rotor to make levitation so that the rotor can rotate without any contact with the stator. Displacement sensors are very close attached to the electromagnetic bearings to make feedback of the displacement deviation which make it possible for the rotor to be controller actively. Equation of motion of the rotor shown in Fig. 3 is such as:

$$\begin{aligned} M\ddot{q} + G\dot{q} &= {}_{M}T_{B}u_{AMB} \\ y &= {}_{S}T_{M}q \end{aligned} \tag{10}$$

$$M=\begin{bmatrix} I_y & 0 & 0 & 0 \\ 0 & m & 0 & 0 \\ 0 & 0 & I_x & 0 \\ 0 & 0 & 0 & m \end{bmatrix} G=\begin{bmatrix} 0 & 0 & I_z\Omega & 0 \\ 0 & 0 & 0 & 0 \\ -I_z\Omega & 0 & 0 & 0 \\ 0 & 0 & 0 & 0 \end{bmatrix} \tag{11}$$

$${}_{M}T_{B}=\begin{bmatrix} a & b & 0 & 0 \\ 1 & 1 & 0 & 0 \\ 0 & 0 & a & b \\ 0 & 0 & 1 & 1 \end{bmatrix} {}_{S}T_{M}=\begin{bmatrix} c & 1 & 0 & 0 \\ d & 1 & 0 & 0 \\ 0 & 0 & c & 1 \\ 0 & 0 & d & 1 \end{bmatrix}$$

$$\begin{aligned} q &= (\beta, x, -\alpha, y)^T \\ u_{AMB} &= (f_{xA}, f_{xB}, f_{yA}, f_{yB})^T \\ y &= (x_{sA}, x_{sB}, y_{sA}, y_{sB})^T \end{aligned} \tag{12}$$

where, M is the mass matrix that is composed of mass and moment of inertia, G is the gyroscope matrix that is 0 when the rotor stops, however the amplitude gradually becomes greater as the rotational speed goes up. ${}_{M}T_{B}$ is the transformation matrix to transform the bearing coordinates to mass center coordinates, and

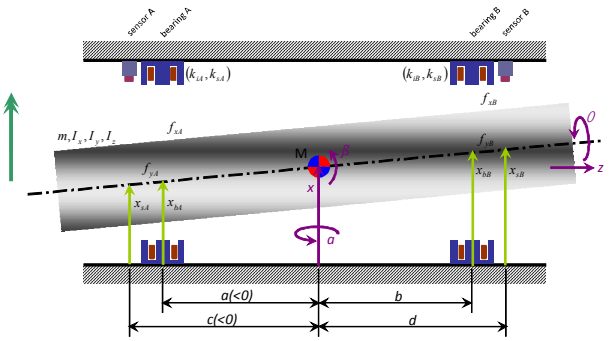

Fig. 3 Conceptual diagram of the rotational machine which has four-degree-of-freedom.

${}_{S}T_{M}$ is the transformation matrix to transform mass center coordinates to displacement sensor coordinates. q is the vector that expresses the position of the radial directions and the rotational angles in the mass center coordinates. u_{AMB} is the force that is generated from the magnetic bearings, and y is the distance that is measured from the displacement sensor to the rotor.

u_{AMB} should be linearized as shown in the fundamental formulas of the one-degree-of-freedom model. Eq. (13) represents the linearized model of the four-degrees-of-freedom model. In Eq. (13), K_s is the displacement stiffness that makes the system unstable as presented in Eq. (6), K_i is the current stiffness, q_B is the vector that indicates the distance from the bearing location to the rotor, and i is the current vector for the bearings.

$$\begin{aligned} u_{AMB} &= \begin{bmatrix} f_{xA} \\ f_{xB} \\ f_{yA} \\ f_{yB} \end{bmatrix} = -\begin{bmatrix} k_{sA} & 0 & 0 & 0 \\ 0 & k_{sB} & 0 & 0 \\ 0 & 0 & k_{sA} & 0 \\ 0 & 0 & 0 & k_{sB} \end{bmatrix} \begin{bmatrix} x_{bA} \\ x_{bB} \\ y_{bA} \\ y_{bB} \end{bmatrix} \\ &+ \begin{bmatrix} k_{iA} & 0 & 0 & 0 \\ 0 & k_{iB} & 0 & 0 \\ 0 & 0 & k_{iA} & 0 \\ 0 & 0 & 0 & k_{iB} \end{bmatrix} \begin{bmatrix} i_{xA} \\ i_{xB} \\ i_{yA} \\ i_{yB} \end{bmatrix} \\ &= -K_s q_B + K_i i \end{aligned} \tag{13}$$

From Eqs. (10) and (13), the linearized equation of motion is such as:

$$M\ddot{q} + G\dot{q} = {}_{M}T_{B}(-K_s q_B + K_i i) \tag{14}$$

The vector q_B is transformed to mass center coordinates by using the transformation matrix ${}_{M}T_{B}$

which is expressed as:

$$q_B = \begin{bmatrix} x_{bA} \\ x_{bB} \\ y_{bA} \\ y_{bB} \end{bmatrix} = \begin{bmatrix} a & 1 & 0 & 0 \\ b & 1 & 0 & 0 \\ 0 & 0 & a & 1 \\ 0 & 0 & b & 1 \end{bmatrix} \begin{bmatrix} \beta \\ x \\ -\alpha \\ y \end{bmatrix} \quad (15)$$

$$= {}_BT_M q = \left({}_MT_B \right)^T q$$

Substituting Eq. (15) for Eq. (14) yields:

$$M\ddot{q} + G\dot{q} = -{}_MT_B K_s {}_MT_B^T q + {}_MT_B K_i i = -K_{sM} q + {}_MT_B K_i i \quad (16)$$

$$M\ddot{q} + G\dot{q} + K_{sM} q = {}_MT_B K_i i$$

where,

$$K_{sM} = {}_MT_B K_s {}_MT_B^T$$

$$= \begin{bmatrix} k_{sA}a^2 + k_{sB}b^2 & k_{sA}a + k_{sB}b & 0 & 0 \\ k_{sA}a + k_{sB}b & k_{sA} + k_{sB} & 0 & 0 \\ 0 & 0 & k_{sA}a^2 + k_{sB}b^2 & k_{sA}a + k_{sB}b \\ 0 & 0 & k_{sA}a + k_{sB}b & k_{sA} + k_{sB} \end{bmatrix}$$

As seen in Eq. (16), the mathematical model of the four-degrees-of-freedom rotational machine supported by magnetic bearings is very similar to the 2nd order mechanical system. However, the rotor shaft is coupled due to the gyroscopic effect and the non-colocation problem between the displacement sensors and the magnetic bearing actuators as shown in Eq. (16).

Voltage equations without flux feedback are expressed in Eq. (17).

$$V = Ri + L\frac{di}{dt} - K_i \frac{dq_B}{dt} \quad (17)$$

Eq. (17) can be modified to present matrix pattern as:

$$\begin{bmatrix} v_{xA} \\ v_{xB} \\ v_{yA} \\ v_{yB} \end{bmatrix} = \begin{bmatrix} R_A & 0 & 0 & 0 \\ 0 & R_B & 0 & 0 \\ 0 & 0 & R_A & 0 \\ 0 & 0 & 0 & R_B \end{bmatrix} \begin{bmatrix} i_{xA} \\ i_{xB} \\ i_{yA} \\ i_{yB} \end{bmatrix} + \begin{bmatrix} L_A & 0 & 0 & 0 \\ 0 & L_B & 0 & 0 \\ 0 & 0 & L_A & 0 \\ 0 & 0 & 0 & L_B \end{bmatrix} \begin{bmatrix} \dot{i}_{xA} \\ i_{xB} \\ i_{yA} \\ i_{yB} \end{bmatrix} - \begin{bmatrix} k_{iA} & 0 & 0 & 0 \\ 0 & k_{iB} & 0 & 0 \\ 0 & 0 & k_{iA} & 0 \\ 0 & 0 & 0 & k_{iB} \end{bmatrix} \begin{bmatrix} \dot{x}_{bA} \\ x_{bB} \\ y_{bA} \\ y_{bB} \end{bmatrix} \quad (18)$$

From Eq. (17) and by using transformation matrix ${}_MT_B$, current slew rate is derived.

$$\frac{di}{dt} = L^{-1}V - L^{-1}Ri + K_i^{-1}K_s \frac{dq_B}{dt} = L^{-1}V - L^{-1}Ri + K_i^{-1}K_s {}_MT_B^T \frac{dq}{dt} \quad (19)$$

The state space model for the four-degrees-of-freedom rotational machine can be presented by using Eqs. (17)-(19).

$$\begin{bmatrix} \dot{q} \\ \dot{q} \\ \dot{i} \end{bmatrix} = \begin{bmatrix} 0 & I & 0 \\ -M^{-1}K_{sM} & -M^{-1}G & -M^{-1}{}_MT_B K_i \\ 0 & K_i^{-1}K_s {}_MT_B^T & -L^{-1}R \end{bmatrix} \begin{bmatrix} q \\ \dot{q} \\ i \end{bmatrix} + \begin{bmatrix} 0 \\ 0 \\ L^{-1}V \end{bmatrix} \quad (20)$$

3. Flux Feedback Loop

3.1 One-Degree-of-Freedom

In this section, estimation of the open loop characteristics using flux feedback is presented. The air gap flux which is produced by the core magnet is proportional to the pole face area as:

$$\Phi = BA = \frac{\mu_0 NAi}{2z} \quad (21)$$

The time derivative of Φ yields

$$\frac{d}{dt}\Phi = \frac{\mu_0 AN}{2z}\frac{di}{dt} + \frac{\mu_0 ANi_0}{2z^2}\frac{dz}{dt} \quad (22)$$

If the magnetic flux Φ is fed back to the amplifier that activates the electromagnets the terms for the dynamics of the electromagnet actuators should be modified so that the force component which is included in the magnetic flux Φ should be included in the actuator dynamic equation. This yields Eq. (23).

$$\begin{aligned} v(t) &= Ri(t) + \frac{d}{dt}\left[L(i,z)i(t)\right] + k_{\Phi\Phi}N\Delta\Phi_a \\ &= Ri(t) + \frac{\mu_0 N^2 A}{2z(t)}\frac{d}{dt}i(t) - \frac{\mu_0 N^2 Ai_0}{2z(t)^2}\frac{d}{dt}z(t) \\ &\quad + k_{\Phi\Phi}(k_{fi}i(t) - k_{fz}z(t)) \\ &= Ri(t) + L\dot{i}(t) - k_i\dot{z}(t) + k_{\Phi\Phi}(k_{fi}i(t) - k_{fz}z(t)) \end{aligned} \quad (23)$$

where, $k_{fi} = \dfrac{\mu_0 A N^2}{2 z_0}$, $k_{fz} = \dfrac{\mu_0 A N^2 i_0}{2 z_0^2}$ and $k_{\Phi\Phi}$ is flux feedback gain.

Compare to Eq. (7), the flux feedback term is included in Eq. (23) which is expressed as linear combination of the coil current and air gap deviation. A combination of Eqs. (1), (6) and (12) induces the state space model including the flux feedback such as:

$$\begin{bmatrix} \dot{z} \\ \ddot{z} \\ \dot{i} \end{bmatrix} = \begin{bmatrix} 0 & 1 & 0 \\ \dfrac{-k_z}{m} & 0 & \dfrac{k_i}{m} \\ \dfrac{k_{\Phi\Phi} k_{fz}}{L} & \dfrac{k_z}{k_i} & \dfrac{(-R - k_{\Phi\Phi} k_{fi})}{L} \end{bmatrix} \begin{bmatrix} z \\ \dot{z} \\ i \end{bmatrix} + \begin{bmatrix} 0 \\ 0 \\ \dfrac{1}{L} \end{bmatrix} v + \begin{bmatrix} 0 \\ \dfrac{1}{m} \\ 0 \end{bmatrix} f_d \tag{24}$$

Fig. 4 presents the open-loop diagram with flux feedback loop. In Fig.4, $k_{\Phi\Phi}$ represents the flux feedback gain.

From the characteristic equation of Eq. (24), the gain of the flux feedback loop $k_{\Phi\Phi}$ can be adjusted such that

$$k_{\Phi\Phi} = -\frac{k_z R}{k_i k_{zi} - k_z k_{iz}} \tag{25}$$

The input-output transfer function is reduced to

$$z(s) = \left[\frac{\dfrac{k_i}{m} L}{s^2 \left\{ s + \dfrac{R}{L} + \dfrac{k_{\Phi\Phi} k_{fi}}{L} \right\}} \right] v(s) \tag{26}$$

which indicates that flux feedback makes the system conditionally stable due to free from the k_z parameter variation.

3.2 Four-Degrees-of-Freedom

Voltage equations with flux feedback are expressed in Eq. (27) which is the same as Eq. (23) except for the number of degrees of freedom.

$$V = Ri + L\frac{di}{dt} - K_i \frac{dq_B}{dt} + K_{\varphi\varphi} K_{fi} i - K_{\varphi\varphi} K_{fz} q_B \tag{27}$$

Matrix pattern of Eq. (27) and current slew rate are expressed in Eqs. (28) and (29), respectively.

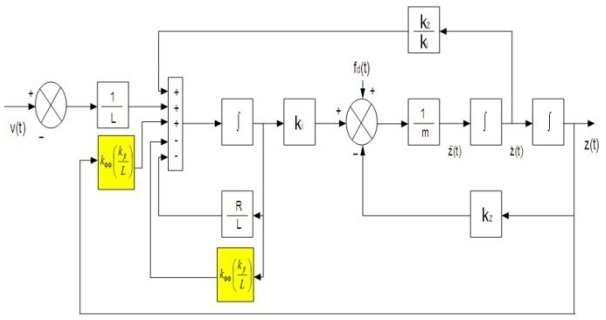

Fig. 4 Open-loop diagram with flux feedback.

$$\begin{bmatrix} V_{xA} \\ V_{xB} \\ V_{yA} \\ V_{yB} \end{bmatrix} = \begin{bmatrix} R_A & 0 & 0 & 0 \\ 0 & R_B & 0 & 0 \\ 0 & 0 & R_A & 0 \\ 0 & 0 & 0 & R_B \end{bmatrix} \begin{bmatrix} i_{xA} \\ i_{xB} \\ i_{yA} \\ i_{yB} \end{bmatrix} + \begin{bmatrix} L_A & 0 & 0 & 0 \\ 0 & L_B & 0 & 0 \\ 0 & 0 & L_A & 0 \\ 0 & 0 & 0 & L_B \end{bmatrix} \begin{bmatrix} \dot{i}_{xA} \\ i_{xB} \\ i_{yA} \\ i_{yB} \end{bmatrix}$$
$$- \begin{bmatrix} k_{iA} & 0 & 0 & 0 \\ 0 & k_{iB} & 0 & 0 \\ 0 & 0 & k_{iA} & 0 \\ 0 & 0 & 0 & k_{iB} \end{bmatrix} \begin{bmatrix} \dot{x}_{bA} \\ x_{bB} \\ y_{bA} \\ y_{bB} \end{bmatrix} + \begin{bmatrix} k_{\varphi\varphi} k_{fiA} & 0 & 0 & 0 \\ 0 & k_{\varphi\varphi} k_{fiB} & 0 & 0 \\ 0 & 0 & k_{\varphi\varphi} k_{fiA} & 0 \\ 0 & 0 & 0 & k_{\varphi\varphi} k_{fiB} \end{bmatrix} \begin{bmatrix} i_{xA} \\ i_{xB} \\ i_{yA} \\ i_{yB} \end{bmatrix}$$
$$- \begin{bmatrix} k_{\varphi\varphi} k_{fzA} & 0 & 0 & 0 \\ 0 & k_{\varphi\varphi} k_{fzB} & 0 & 0 \\ 0 & 0 & k_{\varphi\varphi} k_{fzA} & 0 \\ 0 & 0 & 0 & k_{\varphi\varphi} k_{fzB} \end{bmatrix} \begin{bmatrix} x_{bA} \\ x_{bB} \\ y_{bA} \\ y_{bB} \end{bmatrix} \tag{28}$$

$$\frac{\mathrm{d}i}{\mathrm{d}t} = L^{-1}V - L^{-1}Ri - K_i^{-1}K_s \frac{\mathrm{d}q_B}{\mathrm{d}t} - L^{-1}K_{\varphi\varphi}K_{fi}i + L^{-1}K_{\varphi\varphi}K_{fz}q_B$$
$$= L^{-1}V - L^{-1}Ri - K_i^{-1}K_{s\_M}T_B^T \frac{\mathrm{d}q}{\mathrm{d}t} - L^{-1}K_{\varphi\varphi}K_{fi}i + L^{-1}K_{\varphi\varphi}K_{fz\_M}T_B^T q \tag{29}$$

where,

$$K_{\varphi\varphi} = \begin{bmatrix} k_{\varphi\varphi} & 0 & 0 & 0 \\ 0 & k_{\varphi\varphi} & 0 & 0 \\ 0 & 0 & k_{\varphi\varphi} & 0 \\ 0 & 0 & 0 & k_{\varphi\varphi} \end{bmatrix}, K_{fi} = \begin{bmatrix} k_{fiA} & 0 & 0 & 0 \\ 0 & k_{fiB} & 0 & 0 \\ 0 & 0 & k_{fiA} & 0 \\ 0 & 0 & 0 & k_{fiB} \end{bmatrix}, K_{fz} = \begin{bmatrix} k_{fzA} & 0 & 0 & 0 \\ 0 & k_{fzB} & 0 & 0 \\ 0 & 0 & k_{fzA} & 0 \\ 0 & 0 & 0 & k_{fzB} \end{bmatrix}$$

From Eqs. (28) and (29), the state space equations are

$$\begin{bmatrix} \dot{q} \\ \ddot{q} \\ \dot{i} \end{bmatrix} = \begin{bmatrix} 0 & I & 0 \\ -M^{-1}K_{sM} & -M^{-1}G & -M^{-1}{}_M T_B K_i \\ L^{-1}K_{\varphi\varphi}K_{fz\_M}T_B^T & -K_i^{-1}K_{s\_M}T_B^T & -L^{-1}R - L^{-1}K_{\varphi\varphi}K_{fi} \end{bmatrix} \begin{bmatrix} q \\ \dot{q} \\ i \end{bmatrix} + \begin{bmatrix} 0 \\ 0 \\ L^{-1}V \end{bmatrix} \tag{30}$$

In comparison with Eqs. (20) and (30), Eq. (30) has $k_{\Phi\Phi}$, k_{fz}, k_{fi} in displacement and current terms which make the system stable, that is similar to Eq. (24).

4. Simulations

For the simulations to estimate the flux feedback properties of the electromagnet suspension system, the following parameters are set as in Tables 1 and 2 that

indicate one-degree-of-freedom system and four-degrees-of-freedom system, respectively. In the simulations to assess the effectiveness of the flux feedback loop, load variations in mass are considered.

Figs. 5 and 6 show the air gap deviation of the one-degree-of-freedom system for the case of when the load acting on the controlled object is changed. When the load is 100 kg (Fig. 5) without the flux feedback loop, the controlled object contacts (dashed line) the electromagnets at time 50 s. In case of 500 kg (Fig. 6), it takes more time to contact the electromagnets than that of Fig. 5 due to the heavier load, however, the vibration amplitude becomes bigger and bigger with time. This is because of the inherent unstable characteristics of the magnetic suspension system.

On the contrary, the simulation results with flux feedback loop shown in Figs. 7 and 8 present very good bounded characteristics against the load variation. Fig. 7 is for the case when the load is 100 kg. In Fig. 7, very good robustness property is shown when there is a parameter variation of the EMS system. The small vibration in Fig. 7 is because there is no feedback active controller. Thus, any kind of feedback controller can eliminate this vibration. In Fig. 8, we can see slower vibration and bigger amplitude

Table 1 Parameters for the one-degree-of-freedom system.

Variables	Value	Unit
Mass: m	100, 500	(Kg)
Coil inductance: L	72	(mH)
Coil resistance: R	0.7	(Ω)
Steady current: i_0	1	(A)
Cross sectional area: A	2.2×10^{-6}	(m^2)
Number of turns: N	140	(turns)
Permeability: μ_0	$4\pi \times 10^{-7}$	(H/m)

Table 2 Parameters for the four-degrees-of-freedom system.

Variables	Value	Unit
Mass: m	100, 500	(Kg)
Coil inductance: L	50	(mH)
Coil resistance: R	1	(Ω)
Steady current: i_0	1	(A)
Cross sectional area: A	1.666×10^{-4}	(m^2)
Number of turns: N	152	(turns)
Permeability: μ_0	$4\pi \times 10^{-7}$	(H/m)

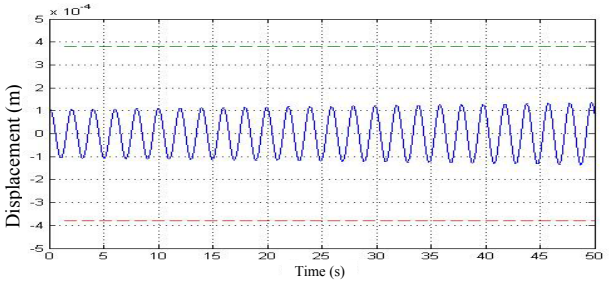

Fig. 5 Gap deviation without flux feedback for one-degree-of-freedom (m = 100 kg).

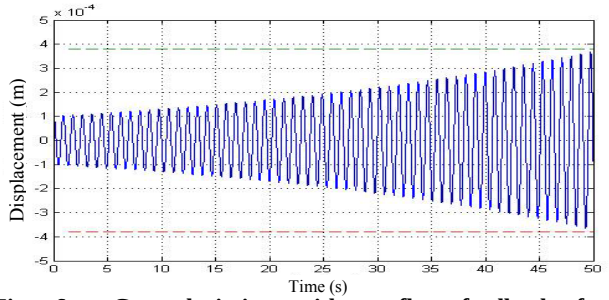

Fig. 6 Gap deviation without flux feedback for one-degree-of-freedom (m = 500 kg).

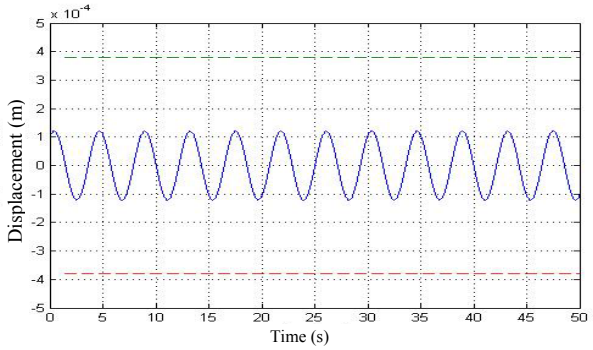

Fig. 7 Gap deviation with flux feedback for one-degree-of-freedom (m = 100 kg).

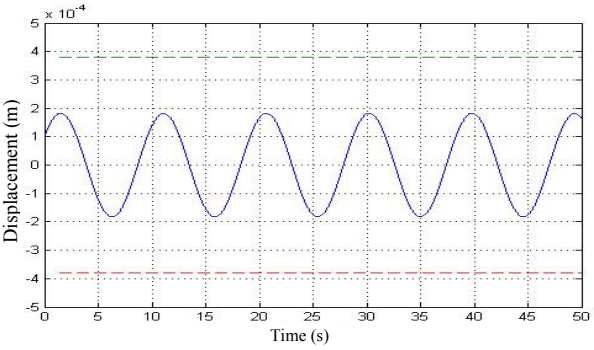

Fig. 8 Gap deviation with flux feedback for one-degree-of-freedom (m = 500 kg).

than that of Fig. 7. This is because of the much heavier load (500 kg).

Figs. 9-16 are the simulation results for the four-degrees-of-freedom system that includes load variations in mass (100 kg, 500 kg). The gap deviations in the x and y directions that the flux feedback loop is not applied are shown in Figs. 9-12. As seen in Figs. 9-12, due the no flux feedback loop, the system is not bounded, however as shown in Figs.

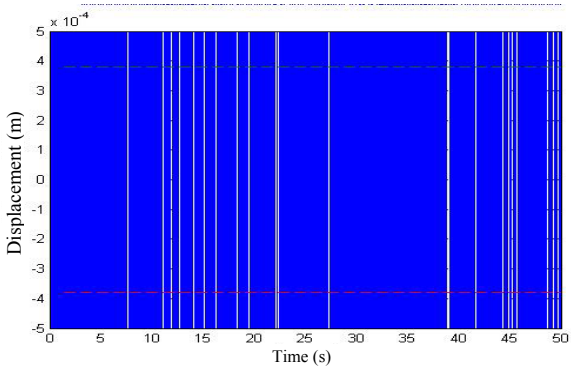

Fig. 9 Gap deviation without flux feedback for four-degrees-of-freedom (m = 100 kg, x direction).

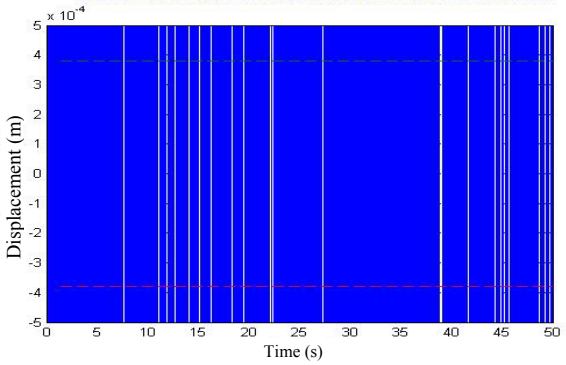

Fig. 10 Gap deviation without flux feedback for four-degrees-of-freedom (m = 100 kg, y direction).

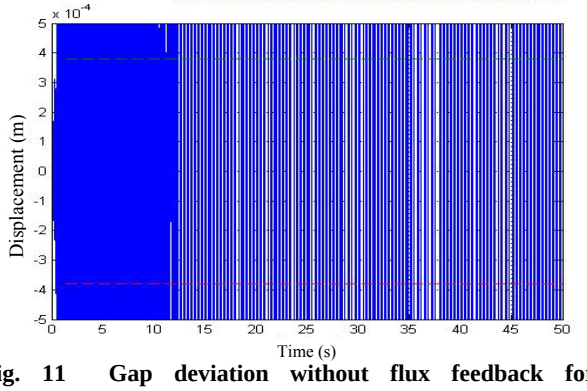

Fig. 11 Gap deviation without flux feedback for four-degrees-of-freedom (m = 500 kg, x direction).

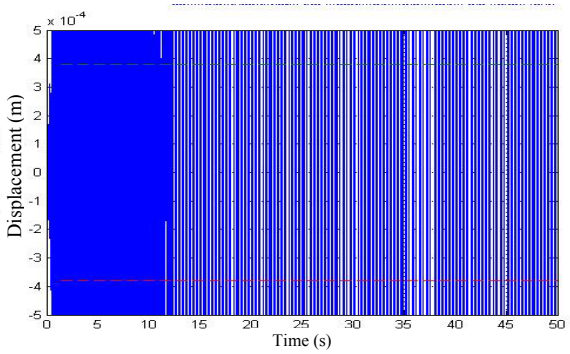

Fig. 12 Gap deviation without flux feedback for four-degrees-of-freedom (m = 500 kg, y direction).

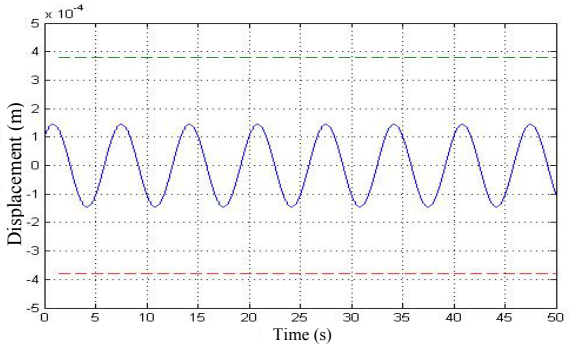

Fig. 13 Gap deviation with flux feedback for four-degrees-of-freedom (m = 100 kg, x direction).

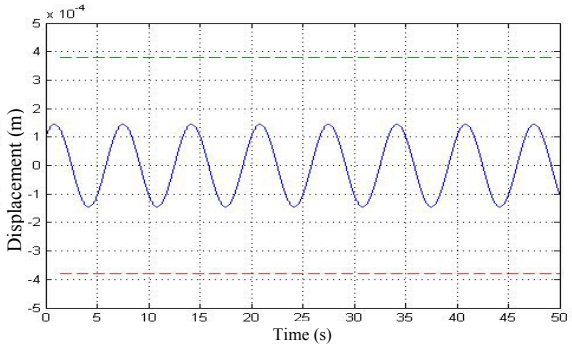

Fig. 14 Gap deviation with flux feedback for four-degrees-of-freedom (m = 100 kg, y direction).

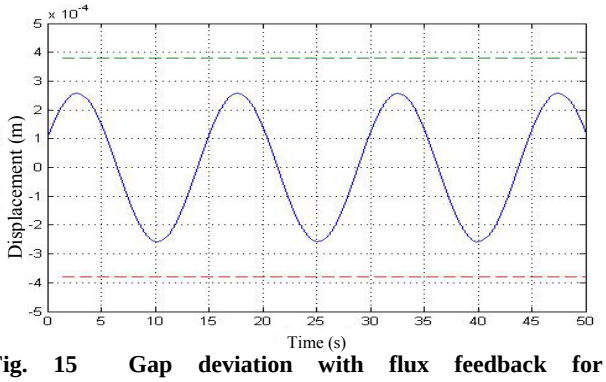

Fig. 15 Gap deviation with flux feedback for four-degrees-of-freedom (m = 500 kg, x direction).

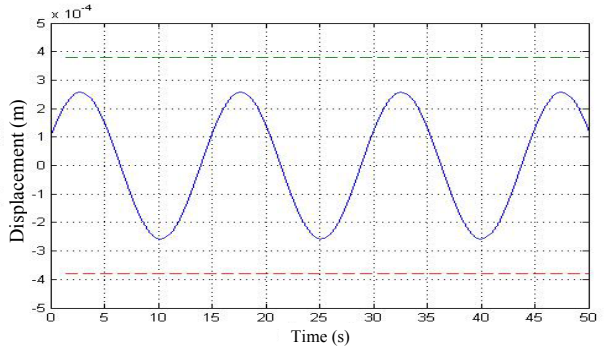

Fig. 16 Gap deviation with flux feedback for four-degrees-of-freedom (*m* = 500 kg, *y* direction).

12-16, the system is well bounded under the effect of the flux feedback loop even if the degree-of-freedom of the system is increased and also the load level is changed (100 kg, 500 kg). This is because of the flux dieback loop that represents linear relationship with respect to the change of the coil current and the air gap displacement which make it possible to decrease in the parameter uncertainties of the k_z, k_i for the one-degree-of-system and the k_s, k_i for the four-degrees-of-system.

7. Conclusions

In this paper, the open loop characteristics of the electromagnets suspension system which has the flux feedback loop to be applied to the multi-degrees-of-freedom rotational machinery have been dealt with. The flux feedback loop increases the system robustness against the parameter variations even if no active controller is employed. This property comes from the flux feedback loop that is presented in linear combination of the air gap displacement and the coil current which is different from the conventional open loop structure. First, we showed the fundamental mathematical model which has no flux feedback loop, and then introduced the modified mathematical model including the flux feedback loop. Finally, the robustness against the parameter variations for the modified open loop scheme has been achieved by the simulations, even if the load acting on the system has been changed. This modified open loop scheme can be applied to a system which has multi-degrees-of-freedom and frequent load variations such as magnetically levitated systems.

References

[1] T. Jin, Y. Liu, A novel GNSS weak signal acquisition using wavelet denoising method, in: Proceedings of the 2008 National Technical Meeting of the Institute of Navigation, San Diego, CA, Jan. 28-30, 2008, pp. 28-30.

[2] J.H. Lee, P.E. Allaire, G. Tao, X. Zhang, Integral sliding mode control of a magnetically suspended balance beam: Analysis, simulation and experimentation, IEEE Trans. On Mechatronics 6 (3) (2001) 338-346.

[3] P.K. Sinha, Electromagnetic Suspension: Dynamics and Control, Peter Peregrinus Limited, UK, 1987.

[4] G. Schweitzer, E.H. Eric, Magnetic Bearings: Theory, Design, and Application to Rotating Machinery, Springer, New York, 2009.

[5] T. Hu, Z. Lin, B. Huang, W. Jiang, P. Allaire, Control of balance beam: A linear design approach, in: 8th International Symposium on Magnetic Bearings, Mito, Japan, 2002.

[6] T. Hu, Z. Lin, P. Allaire, Power loss reduction by optimizing current allocation in magnetic bearings, in: 8th International Symposium on Magnetic Bearings, Mito, Japan, 2002.

[7] J. Lindlau, C.R. Knospe, Feedback linearization of an active magnetic bearing with voltage control, IEEE Transactions on Control Systems Technology 10 (1) (2002) 21-31.

[8] Z. Lin, M. Glauser, T. Hu, P.E. Allaire, Magnetically suspended balance beam with disturbances: A test rig for nonlinear output regulation, International Journal of Advanced Mechatronic Systems 1 (1) (2008) 2-9.

[9] G. Li, Z. Lin, P. Allaire, J. Luo, Modeling of a high speed flywheel control test rig with active magnetic bearings, ASME Journal of Vibration and Acoustics 128 (3) (2006) 269-281.

[10] J.H. Lee, P.E. Allaire, W. Jiang, T. Hu, Z. Lin, Cancellation of static and sinusoidal disturbance forces in a magnetic suspension system using exerted force and flux feedback, in: Eighth International Symposium on Magnetic Bearings, Japan, Aug. 26-28, 2002.

[11] J.H. Lee, A study on an effect of the flux feedback on an open-loop characteristic of the magnetic levitation system, in: 13th International Symposium on Magnetic Bearings, Washington, Virginia, USA, Aug. 6-8, 2012.

Journal of Mechanics Engineering and Automation 4 (2014) 542-546

Effects of Sedentarism and Treadmill Training in Mechanical Properties of Muscles of Ovariectomized Rats with High-Fat Diet

Ana Paula Macedo[1], Débora Taffarel Ferrari[1], Roberta C Shimano[1], João Paulo Mardegan Issa[1, 2], Alceu Afonso Jordão[3] and Antônio Carlos Shimano[1]

1. Department of Biomechanics, Medicine and Rehabilitation of the Locomotor System, Ribeirão Preto Medical School, University of São Paulo, Ribeirão Preto 14049-900, Brazil

2. Departament of Morphology, Physiology and Basic Pathology, School of Dentistry of Ribeirão Preto, University of São Paulo, Ribeirão Preto 14040-904, Brazil

3. Department of Internal Medicine, Ribeirão Preto Medical School, University of São Paulo, Ribeirão Preto 14049-900, Brazil

Received: March 01, 2014 / Accepted: March 21, 2014 / Published: June 25, 2014.

Abstract: The aim of this study is to evaluate the ability of physical training in the maintenance of muscle strength in rats with HFD (high-fat diet) after OVX (ovariectomy). Eighty Wistar rats are at eight weeks of age and weight 200 g which divided into 8 groups (n = 10) and treated for 12 weeks: GA: OVX + ND (normal diet), GB: OVX + ND + training, GC: sham + ND, GD: sham + ND + training, GE: OVX + HFD, GF: OVX + HFD + training, GG: sham + HFD and GH: sham + HFD + training. HFD consists of standard ration for rats with addition of 30% lipids. In training groups, physical training five training/week was conducted on a treadmill with adaptation period of three weeks up to 18 m/s for one hour, training were performed for 12 weeks. The sedentary animals remained in individual box. To analyze the effects of training and diet, tensile strength tests of the gastrocnemius muscles were conducted: the speed of 0.1 mm/min. Analysis of variance was performed to compare groups. The mean (SD) obtained for the maximum load (N) were: GA 57.77 (6.89), GB 62.74 (5.07), GC 49.45 (6.06), GD 59.42 (5.26) and GE 55.58 (4.72), GF 62.50 (4.56), GG 58.35 (4.54) and GH 56.67 (5.87), respectively. There were no differences for maximum load between surgeries (p = 0.004) and between treatments (p = 0.000). Differences were found also for the relationship surgery diet treatment (p = 0.007). For the variable stiffness (N/mm), there were not statistically significant differences: GA 5.03 (0.72), GB 5.08 (1.09), GC 5.17 (0.53), GD 5.35 (0.80), GE 5.52 (1.20), GF 5.36 (1.07), GG 4.83 (1.03) and GH 5.40 (0.73). For the toughness (N/mm), there were differences between treatments (p = 0.010) and the ratio diet treatment (p = 0.024): GA 455.00 (107.21), GB 541.96 (126.80), GC 394.97 (84.67), GD 566.90 (157.07); GE 424.63 (113.03), GF 478.07 (106.03); GG 517.44 (98.65) and GH 481.26 (129.45). OVX causes decrease in muscle maximum load; exercise treadmill provides increased muscular endurance, regardless of the diet and the OVX in groups, the increased resistance observed in the groups submitted to HFD can result in weight gain associated with the presence estrogen.

Key words: Physical training, ovariectomy, mechanical property, gastrocnemius muscles, high-fat diet.

1. Introduction

The intake of micronutrients (vitamins and minerals) and macronutrients (carbohydrate, lipid and protein) are directly related to growth, physical development, cognitive and motor of the individual. A deficiency or excess of these nutrients in childhood can cause serious diseases in adulthood [1]. Nutrition is based on quantitative and qualitative balance necessary for healthy function of the organism. Another problem faced by the public health is overweight due to wrong diets. Surveys conducted in rats showed that low levels of vitamin D and calcium are associated with a

Corresponding author: Ana Paula Macedo, Ph.D., research fields: bioengineering. E-mail: anapaula@forp.usp.br.

HFD (high-fat diet) affect bone development [2, 3]. However, we found no reports in the literature describing the influence of a HFD in muscle strength.

One of the major problems reported postmenopausal is the loss of muscle mass. Probably a more important than human estrogen health issue is related to potential differences in susceptibility to exercise-induced muscle damage in women of premenopausal and postmenopausal. Studies by Amelink et al. [4] showed a primary effect of estrogen may be to protect muscle membranes from muscle damage induced by exercise. The reduction of muscle membrane disruption may also be important in the inflammatory and muscle repair [5]. It has been reported that the loss of estrogen after menopause may result in more power loss associated with aging and a reduced rate of gain of strength in older women. Thus, although some information is available, definitive studies on the influence of estrogen on skeletal muscle damage are deficient and additional research is needed [6].

Several studies have shown that exercise provides a better quality of life and benefiting various aspects of the organism. In this aspect, musculoskeletal promotes muscle strengthening and greater strength and stability of the bones and joints, also favoring one physical wellbeing, mental and social. Already, a sedentary lifestyle is a risk factor for several diseases [7, 8]. Known for their beneficial effects, physical activity has been used in recent years as a method of prevention and analysis of muscle atrophy [9-11]. In addition, training controls the effects of ovariectomy on fat accumulation, lipid profile and lipid content of the tissue [12, 13].

The mechanical test is a standardized technique as used in the evaluation of mechanical properties of materials in different applications, using specimens or experimental models. The tests allow knowing the response of the material by applying different loads. Among the destructive testing has the tensile test, bending, torsion, impact, and fatigue among other nondestructive testing, has ultrasound, x-ray [14].

The aim of this study is to evaluate the ability of physical training in the maintenance of muscle strength in rats with HFD after OVX (ovariectomy).

2. Material and Methods

Eighty Wistar rats, eight weeks of age and weight (200 ± 5) g were ovariectomized and divided into eight groups (n = 10) and treated for 12 weeks: GA: OVX + ND (normal diet), GB: OVX + ND + training, GC: sham + ND, GD: sham + ND + training, GE: OVX + HFD, GF: OVX + HFD + training, GG: sham + HFD and GH: sham + HFD + training.

The diet consists of standard ration diet to rats with addition of 30% lipids [15].

In the trained groups, physical training was performed on a treadmill with adaptation period of three weeks until reaching a speed of 18 m/s during one hour. Five training sessions were conducted per week for 12 weeks, totaling 60 sessions of training.

The sedentary animals remained in “reduced” cages, individually for a period of 12 weeks, according to the guide for Care and Use Laboratory Animals [16].

To analyze the effects of diets and treatments offered, tensile test of the gastrocnemius muscles were performed. The speed was 10 mm/min with preload of 5 N for 60 s in a universal testing machine (EMIC-DL® 10,000). We obtained the maximum load (N)-F_{max}, stiffness (N/mm) and tenacity (N.mm).

To evaluate the effect of training and diet at mechanical proprieties, the statistical analysis was performed using a mixed linear model, which is a generalization of the standard linear model (ANOVA) with Bonferroni’s complementary test using the statistical software SPSS 17.0 for Windows (SPSS Inc., Chicago, IL, USA). Differences were considered significant when $p < 0.05$.

3. Results

Table 1 shows the results of the Shapiro-Wilk test for the evaluation of the normality of the variables.

The results obtained after analysis are shown in Table 2.

When evaluating the influence of the type of surgery in maximum load (N) observed statistical differences between the OVX and SHAM groups (p = 0.004). No statistical differences were found in maximum load for the different diets (p = 0.413), but differences were found for the different treatments (p = 0.000). By comparing the effect of the interaction of the variables, differences for the relationship surgery diet treatment (p = 0.007) was observed, but not to surgery diet (p = 0.072), surgery treatment (p = 0.428) and diet treatment (p = 0.054).

Table 1 Normality test.

	Shapiro-Wilk		
	Statistic	df	Sig.
F_{max}	0.981	80	0.286
Stiffness	0.982	80	0.329
Tenacity	0.978	80	0.183

After identifying differences in the interaction surgery, diet treatment was performed multiple comparisons in which it was observed that animals with HFD, treadmill-trained and under different surgery (GD and GH) showed statistical differences in relation to the maximum load (p = 0.018). Animals with standard diet, sedentary and subjected to different surgery (GA and GE) showed statistical differences with respect to maximum load (p = 0.001). SHAM animals, sedentary with different diets (GE and GF) showed statistical differences (p = 0.000). It was also observed that OVX animals, that receiving HFD and different treatments (GB and GD) showed statistical differences (p = 0.005) and SHAM animals with standard diet and different treatments (GE and GG) was statistically different (p = 0.000).

No statistical differences were observed in the stiffness (N/mm) for any of the variables nor for the iterations (surgery: p = 0.853, diet: p = 0.657, treatment: p = 0.464, surgery diet: p = 0.240, surgery treatment: p = 0.333, diet treatment: p = 0.905 and surgery diet treatment: p = 0.566).

When evaluating the tenacity (N.mm) their differences statistically significant between treatments (p = 0.010) and the ratio diet treatment (p = 0.024).

When evaluating the effect of treatments on tenacity (N.mm), statistical differences were observed. between groups (p = 0.010). There were no statistical differences in tenacity for different surgeries (p = 0.582) and diet (p = 0.605). By comparing the effect of the interactions between variables was possible to observe differences in diet treatment (p = 0.025), but not to surgery diet (p = 0.197), surgical treatment (p = .936) and treatment diet surgery (p = 0.103).

Table 2 Mean (standard deviation) of maximum load (F_{max}), stiffness and tenacity.

Groups	F_{max} (N)*	Stiffness (N/mm)*	Tenacity (N.mm)*
GA	57.77 (6.89)	5.03 (0.72)	455.00 (107.21)
GB	62.74 (5.07)	5.08 (1.09)	541.96 (126.80)
GC	49.45 (6.06)	5.17 (0.53)	394.97 (84.67)
GD	59.42 (5.26)	5.35 (0.80)	566.90 (157.07)
GE	55.58 (4.72)	5.52 (1.20)	424.63 (113.03)
GF	62.50 (4.56)	5.36 (1.07)	478.07 (106.03)
GG	58.35 (4.54)	4.83 (1.03)	517.44 (98.65)
GH	56.67 (5.87)	5.40 (0.73)	481.26 (129.45)

*standard deviation.

After identifying differences in diet treatment interaction was performed multiple comparisons in which it was observed that animals with standard diet, subjected to different treatments (GA, GC, GE and GG) showed statistical differences in relation to tenacity (p = 0.001).

4. Discussion

Several studies have evaluated the influence of high-fat diet on bone quality, obesity and body composition [15, 17-19]. However, there are no reports on the influence of diets rich in lipids in muscle strength after OVX. The objective of this study was to evaluate the influence of HFD on muscle strength in ovariectomized rats.

In the present study, less muscular strength was observed for animals submitted to OVX. This is an important result because reduced ovarian levels leads to endocrine and functional disorders, such as loss of

libido, increased risk of osteoporosis and heart disease, abnormal levels of lipoproteins and weight gain [20]. Differences were found between treatments for maximum load and tenacity.

When evaluating the difference between groups observed that animals with standard diet, sedentary and undergo different surgeries (GA and GE) had statistical differences with respect to maximum strength and toughness. Being that OVX had higher values for both variables. SHAM animals underwent surgery, sedentary and with different diets (GE and GF) showed statistical differences for maximum strength. The highest values were assigned to animals receiving fat diet. It was observed that OVX animals undergoing surgery, receiving HFD and different treatments (GB and GD) showed statistical differences in maximum strength, with higher values in the trained animals. SHAM animals underwent surgery, standard diet and different treatments (GE and GF) are statistically different with respect to maximum strength and toughness, with higher values in the trained animals.

As there are no reports in the literature on similar studies, it is believed that these results may be related to greater weight observed in OVX compared to SHAM animals and animals that received HFD compared to those who received standard diet. As for the differences observed between the groups trained or sedentary, we believe that the best results were observed for animals trained to be a result of muscle strengthening arising from treadmill training applied. In Ref. [16], the authors found improvement in mechanical strength in the muscles of trained rats.

Analyzing the results obtained in static tests, we observed differences between the OVX and SHAM groups for maximum strength, but not for stiffness and toughness. However, the different diets resulted in no statistical differences for the variables of the static test. Differences were found between treatments for maximum strength and tenacity.

5. Conclusions

OVX causes decrease in muscle strength; exercise treadmill provides increased muscular endurance, regardless of the diet and the OVX in groups, the increased resistance observed in the groups submitted to HFD can result in weight gain associated with the presence estrogen.

6. Acknowledgment

This study was supported by the National Council of Technological and Scientific Development.

References

[1] G.Q. Morais, M.G.P.A. Burgos, Impact of nutrients in bone health: New trends, Brazilian Journal of Orthopaedics 42 (2007) 189-194.

[2] G. Lac, H. Cavalie, E. Ebal, O. Michaux, Effects of a high fat diet on bone of growing rats. Correlations between visceral fat, adiponectin and bone mass density, Lipids in Health and Disease 7 (16) (2008) 1-4.

[3] J.J. Cao, B.R. Gregoire, H. Gao, High-fat diet decreases cancellous bone mass but has no effect on cortical bone mass in the tibia in mice, Bone 44 (2009) 1097-1104.

[4] G.J. Amelink, P.R. Bär, Exercise-induced muscle protein leakage in the rat: Effects of hormonal manipulation, Journal of the Neurological Sciences 76 (1986) 61-68.

[5] P.M. Tiidus, Influence of estrogen on skeletal muscle damage, inflammation, and repair, Exercise and Sport Sciences Reviews 31 (2003) 40-44.

[6] P.M. Clarkson, M.J. Hubal, Exercise induced muscle damage in humans, American Journal of Physical Medicine and Rehabilitation 81 (2002) S52-S69.

[7] R. Topp, M. Ditmyer, K. King, K. Doherty, J. Hornyak, The effect of bed rest and potential prehabilitation on patients in the intensive care unit, AACN Clinical Issues 13 (2002) 263-276.

[8] H. Mellerowicz, W. Meller, Training: Biological and Medical Basics and Principles of Training, Springer, NY, 1979, pp. 64-70.

[9] J. Tuukkanen, Z. Peng, H.K. Vaananen, Effect of running exercise of bone loss induced by orchidectomy in the rats, Calcified Tissue International 55 (1994) 33-37.

[10] H.E. van der Wiel, P. Lips, W.C. Graafmans, Additional weight-bearing during exercise is more important than duration of exercise for anabolic stimulus of bone: A study of running exercise in female rats, Bone 16 (1995) 73-80.

[11] J. Mathey, M.N.H. Molteni, B. Chanteranne, Bone mass

in obese diabetic Zucker rats: Influence of treadmill running, Calcified Tissue International 70 (2002) 305-311.

[12] L. Hao, Y. Wang, Y. Duan, S. Bu, Effects of treadmill exercise training on liver fat accumulation and estrogen receptor alpha expression in intact and ovariectomized rats with or without estrogen replacement treatment, European Journal of Applied Physiology 109 (2010) 879-886.

[13] R.D. Leite, J. Prestes, C.F. Bernardes, G.E. Shiguemoto, G.B. Pereira, J.O. Duarte, et al., Effects of ovariectomy and resistance training on lipid content in skeletal muscle, liver, and heart; fat depots; and lipid profile, Applied physiology, nutrition, and metabolism 34 (2009) 1079-1086.

[14] S.A. Souza, Mechanical Testing of Metallic Materials, Edgard Blucher LTDA, São Paulo, Brazil, 1982.

[15] M.M. Pinheiro, N.J. Schuch, P.S. Genaro, R.M. Ciconelli, M.B. Ferraz, L.A. Martini, Nutrient intakes related to osteoporotic fractures in men and women—The Brazilian Osteoporosis Study (BRAZOS), Nutrition Journal 8 (6) (2009) 1-8.

[16] J.G.P.O. Milani, J.P.C. Matheus, L.B. Gomide, J.B. Volpon, A.C. Shimano, Biomechanical effects of immobilization and rehabilitation on the skeletal muscle of trained and sedentary rats, Annals of Biomedical Engineering 36 (2008) 1641-1648.

[17] K.L.C. Jen, A. Buison, M. Pellizzon, F. Ordiz, L.S. Ana, J. Brown, Differential effects of fatty acids and exercise on body weight regulation and metabolism in female wistar rats, Experimental Biology and Medicine 228 (2003) 843-849.

[18] A.M. Feoli, C. Roehrig, L.N. Rotta, Serum and liver lipids in rats and chicks fed with diets containing different oils, Nutrition 19 (2003) 789-793.

[19] M.H. Gaíva, R.C. Couto, L.M. Oyama, Diets rich in polyunsaturated fatty acids: Effect on hepatic metabolism in rats, Nutrition 19 (2003) 44-49.

[20] L.S. Vasconcellos, J.M. Leite, K.R. Sabino, A. Petroianu, Influence of ovariectomy on weight change in young and adult rats, Brazilian Archives of Endocrinology and Metabolism 48 (2004) 299-304.

Journal of Mechanics Engineering and Automation
Volume 4, Number 6, June 2014
David Publishing Company
240 Nagle Avenue #15C, New York, NY 10034, USA
Tel: 1-323-984-7526, 323-410-1082; Fax: 1-323-984-7374, 323-908-0457
http://www.davidpublishing.com
mechanics@davidpublishing.com